Medium Energy Ion Scattering Studies of Ultrathin Epitaxial Films

by

Amanda Window

0006016

Supervisor: Professor Phil Woodruff

Department of Physics

September 2009

Contents

List of Figures

List of Tables

Acknowledgments

Firstly, I would like to thank my supervisor, Prof. Phil Woodruff FRS. His expert guidance has helped to make this thesis possible.

Further advice and support has come from the Warwick MEIS group. Gareth Parkinson provided me with much assistance in gaining the knowledge I needed to get started on the project. Whilst my current colleagues Dan Sheppard and Agenor Hentz have given me the help that I needed at Daresbury laboratories both in conducting the MEIS experiments and also in helping me to keep my sanity, especially when we managed to enjoy some time away from the tower at the various Daresbury food and drink outlets. Back at Warwick, the other members of the surface science group have often provided welcome distractions from my work, especially Ts'enolo Lerotholi with whom I have played many good games of squash.

My thanks also go to Rob Johnston, the technician at Warwick for his support through preparing and repairing various items of equipment necessary to perform the experiments, often at the last minute after something had blown up.

At Daresbury laboratories there have been a number of dedicated members of staff who have helped to keep the MEIS facility running as smoothly as possible. In the early days, the beam was kept running by Kevin Connell and Mark Pendleton, and in more recent times the unlucky job of battling the Warwick curse and keeping us provided with MEIS beam fell upon Paul Whitfield, I thank him for his perseverance.

The beamline scientists Tim Noakes and Paul Bailey have helped to solve a great number of equipment problems, including many that had "not been seen before", due to the complex nature of the equipment, and required a great deal of thinking to solve.

Throughout my time at Warwick I have been heavily involved in Warwick Student Cinema, where I project many films as a means of escape. Thanks to filmsoc, I have made many good friends who have helped make my time at Warwick so much fun. Particular mention goes to Ben Goddard, Rachel Crofts and Martin Mee with whom I have imbibed a number of excellent ales. Also Greg Franklin who, not content with beer alone, also provided me with several cups of tea and was always happy to supply a good listening ear and proof read my work.

I would also like to thank my Mum and Dad for their constant support throughout my long academic career and for making many sacrifices to give me every opportunity to succeed. My brother, Gary has always been there for me and has been a good role model to look up to.

My final thanks go to my wonderful Matt, without whom I would not have been able to achieve this. His constant belief has helped me through the more difficult times. His love and devotion have been unwavering and I am so grateful to have had him by my side, supporting me throughout.

Declarations

This thesis is submitted to the University of Warwick in partial fulfilment of the requirements for admission to the degree of Doctor of Philosophy. The work presented in this thesis is my own, except where specifically stated otherwise and was performed in the Department of Physics at the University of Warwick under the supervision of Professor D. P. Woodruff FRS during the period of October 2005 to September 2009. No part of this material has been previously submitted to this or any other institution.

The MEIS data reported in Chapters 4, 5 and 6 were obtained by the author with the aid of Dr. G. S. Parkinson, Dr A. Hentz and Mr. D. C. Sheppard. All of the analysis and interpretation pertaining to these data was performed by the author.

Amanda J. Window

September 2009

Abstract

Medium energy ion scattering (MEIS) has been used to investigate ultrathin epitaxial films.

The depth profiles of $V_2O_3(0001)$ films grown on Pd(111) were examined. The results from this demonstrated that on this substrate the films grown are highly non-uniform, with a large distribution of thicknesses observed for each prepared sample. $V_2O_3(0001)$ films grown on Au(111) were found to form films with a much more even range of thicknesses, good enough to yield blocking curves. The experimental blocking curves obtained are not in good agreement with half-metal or vanadyl terminated structures favoured by most previous studies. Assuming that imperfections exist in the grown films produced better fits, however this lost surface sensitivity. The optimal structure found is an oxygen termination, proposed by a previous density functional theory (DFT) study. This structure is also found to be consistent with re-examined photoelectron diffraction (PhD) data.

Ag_2S films grown on Ag(111) were found to suffer severely from beam-induced damage, limiting quantity of obtained data. Unusually, an He^+ beam was found to produce less severe effects than an H^+ beam. Energy cuts were used to confirm, as proposed by an early Auger electron spectroscopy (AES) study, that the silver sulphide thickness continues to increase with increasing sulphur deposition onto Ag(111). The backscattered ion yields of the blocking curves increased with increasing film thickness, and no additional blocking features were present. These curves were found to be consistent with the structural model proposed by a previous normal incidence X-ray standing waves (NIXSW) study.

$p2gg(\mathbf{4} \times \mathbf{2})$Mn/Cu(100) films were found to form with thicknesses far greater than the two layers anticipated by previous studies. The thick disordered layer precluded any structural analysis. The copper and manganese peaks could not be resolved, resulting in the only information obtained being about the thickness of the films.

Abbreviations

AES	Auger Electron Spectroscopy
ARUPS	Angle-Resolved Ultraviolet Photoemission Spectroscopy
DOS	Density of States
DFT	Density Functional Theory
EELS	Electron Energy Loss Spectroscopy
EQT	Electrostatic Quadropole Triplet
EXAFS	Extended X-ray Absorption Fine Structure
FWHM	Full Width Half Maximum
HEIS	High Energy Ion Scattering
HREELS	High Resolution Electron Energy Loss Spectroscopy
HVEE	High Voltage Engineering Europa
IRAS	Infrared Reflection-Absorption Spectroscopy
ISS	Ion Scattering Spectroscopy
KE	Kinetic Energy
LEED	Low Energy Electron Diffraction
LEIS	Low Energy Ion Scattering
MCP	Micro-Channel Plate
MEED	Medium Energy Electron Diffraction
MEIS	Medium Energy Ion Scattering
ML	Monolayer

NIXSW	Normal Incidence X-ray Standing Waves
PhD	Photoelectron Diffraction
RAIRS	Reflection-Absorption Infra-Red Spectroscopy
RBS	Rutherford Backscattering
SAM	Self-Assembled Monolayer
SIMS	Secondary Ion Mass Spectrometry
SRIM	Stopping and Ranges of Ions in Matter
STM	Scanning Tunnelling Microscopy
SXRD	Surface X-Ray Diffraction
TEA	Toroidal Electrostatic Analyser
TMP	Turbo Molecular Pump
TSP	Titanium Sublimation Pump
UHV	Ultra High Vacuum
XPS	X-ray Photoemission Spectroscopy

Chapter 1

Introduction

Surfaces, in effect, are a special kind of defect resulting from the termination in the long range order of a 3-D periodic solid. This defect reduces the periodicity to 2-D and as a result, surfaces have different structures (both atomic and electronic) in comparison to the bulk. Studies of surfaces are motivated by the fact that they provide an interface between the well-ordered crystal and the surrounding atmosphere, and it is on this interface that a wide range of interesting phenomena can occur, including: heterogeneous catalysis, adsorption, oxidation and corrosion. The study of surfaces proves rather more challenging than studying bulk crystals for two main reasons. The first is that standard solid state theory, used to derive analytical models for crystals in the bulk region, cannot be easily used for surfaces due to the breakdown of 3-D periodicity. Secondly, the experimental techniques used for investigating crystal structure lack sensitivity to surface phenomena, so in order to study surfaces it was necessary to develop techniques specifically for this purpose.

Since the mid 1960s, a wide range of computational and experimental techniques have emerged and been enhanced in order to study various properties of surfaces. Compositional information can be derived from such techniques as Auger electron spectroscopy (AES), X-ray photoemission spectroscopy (XPS), secondary ion mass spectrometry (SIMS), ion scattering spectroscopy (ISS); atomic structure information can be derived from techniques such as low energy electron diffraction

(LEED), ISS, photoelectron diffraction (PhD), extended X-ray absorption fine structure (EXAFS) and surface X-ray diffraction (SXRD); electronic structure can be investigated using, for example, angle-resolved ultraviolet photoemission spectroscopy (ARUPS) and scanning tunnelling microscopy (STM); and vibrational properties can be examined using infrared reflection-absorption spectroscopy (IRAS) (also known as reflection-absorption infra-red spectroscopy (RAIRS)) and high resolution electron energy loss spectroscopy (HREELS), further details about these techniques and others can be found in Woodruff and Delchar [2]. Each technique has different strengths and weaknesses, so to fully investigate a surface it is normal to use a combination of techniques, based on different theoretical principles, in order to provide complementary evidence.

Whilst most of the motivation for studying surfaces is based upon their behaviour in 'real world' situations, the majority of surface science experiments are conducted in a situation far removed from this. Surface studies are typically performed on extremely clean surfaces, in ultra-high vacuum (UHV), and often at low temperatures provided by liquid nitrogen or liquid helium cooling. These experiments are necessary in order to provide a basis of understanding on which further investigations may be developed. Now that many of these basic experiments have been performed, more and more studies are moving towards more realistic conditions.

The main technique used in the work reported in this thesis, for the investigation of surfaces, is medium energy ion scattering (MEIS). The majority of MEIS studies are focussed on high resolution depth profiling of materials, particularly examination of high-k dielectrics by the microelectronics industry. However, MEIS can also be used to provide atomic structure information using entirely different physical principles to other common surface structural tools; because of this MEIS provides good complementary evidence for structures proposed using other techniques. As ever more complicated surface structures are investigated, the various different surface

science techniques begin to experience limitations to the information that it is possible to obtain. This is certainly the case for some of the systems studied for the purpose of this thesis where full structural determinations are not possible, however, the data obtained are generally in agreement with models proposed previously using other techniques.

1.1 Organisation of the Thesis

This thesis describes work conducted in the Department of Physics at the University of Warwick analysing experimental data obtained at the UK MEIS facility in Daresbury during the period March 2006 to October 2008. The systems examined all consist of an ultrathin film grown epitaxially onto single crystal metals. In each system, the quality of the films are explored and, where possible, surface structure investigations are undertaken. The thesis is arranged as follows:

Chapter 2 introduces the principles of the main technique, medium energy ion scattering. The chapter describes the theory behind the technique; how this theory is applied to obtain data; how simulations of the MEIS data are obtained; and how surface structure determinations are made by quantitative comparison between simulations and experimental data.

Chapter 3 provides a brief outline of other supporting surface science techniques: Auger electron spectroscopy and low energy electron diffraction, which are both used in order to characterise prepared surfaces. The chapter then goes on to provide details of the ion beamline, data acquisition, UHV chambers and equipment used at the UK MEIS facility.

Chapters 4 and 5 are concerned with results from two different ultrathin epitaxial film systems: vanadium sesquioxide (V_2O_3) grown on two different substrates, Pd(111) and Au(111); and silver sulphide (Ag_2S) grown on Ag(111). The chapters

both follow the same general format: an introduction outlining the interest in the system and previous work performed on the system; an experimental section discussing surface preparation, characterisation, measurements taken and examination of the potential for beam-induced damage; a results and discussion section of the data analysis, beginning with quantitative interface information and leading onto surface structural investigations; and a final conclusion drawing together the results from the chapter.

Chapter 6 is concerned with ultrathin epitaxial films of copper manganese grown on Cu(100). The chapter contains an introduction outlining the interest in the system and previous work performed on the system; an experimental section discussing surface preparation, characterisation and measurements taken; a results and discussion section of the analysis of the data; and a final conclusion.

Chapter 7 provides a closing summary of the work presented in this thesis and suggestions for further possible work.

Chapter 2

Medium Energy Ion Scattering Theory

2.1 Introduction

A number of techniques exist in surface science that make use of the transfer of kinetic energy (KE) between incident ions and atoms in order to obtain information about the composition and structure of the surface atoms. These techniques exist in different energy regimes: low ($\approx 1-5$ keV), medium ($\approx 50-400$ keV) and high ($\approx 1-2$ MeV). Medium and high energy ion scattering techniques are similar in terms of the underlying physics although medium energies have the advantage of having improved energy resolution compared to high energies and they also produce broader shadow cones (see Section 2.2.7) allowing greater surface sensitivity. Ion scattering techniques in the low energy regime must be considered entirely separately due to the effects of neutralisation making significant contributions and the fact that the scattering potential is not well known, unlike for higher energies [3, 4].

The birth of these techniques was in 1959, when S. Rubin [5] first demonstrated that it was possible to determine the composition of a surface as a function of depth by analysing the momentum distribution of protons backscattered from it. The technique of Rutherford backscattering (RBS) evolved from this early work.

In the period directly afterwards, much work was done using lower energy, heavier ions to study surface composition. The interest in this arose due to the high scattering cross-sections for so-called heavy ions (Z>1) at low energies (less than 3 keV) leading to intrinsic surface specificity. Even at these low energies, the collision process could be considered elastic, as shown experimentally by Smith [6], as well as there existing a large enough proportion of backscattered particles which are not neutralised in these collisions to make analysis feasible [7]. These studies developed into the technique generally known as low energy ion scattering (LEIS) and now used for both surface composition and structural analysis.

In the mid 1970s, Turkenburg *et al.* at the FOM-AMOLF Institute in the Netherlands [8, 9] made some refinements to the RBS technique leading to the technique that is known as medium energy ion scattering (MEIS). MEIS builds on the major advantage of RBS, that scattering cross-sections are well known in this energy regime ($50-400$ keV), but makes use of an electrostatic analyser to obtain a higher energy resolution than can be achieved by the silicon surface barrier detectors used in RBS ($\sim$ 120 eV in MEIS as opposed to $\sim 10-20$ keV in RBS), which in turn leads to a higher depth resolution of $3-5$ Å. MEIS also has the advantage over LEIS that neutralisation effects are less evident.

This chapter reviews the physical principles underlying the MEIS technique, which provides the fundamental basis for the work presented in this thesis.

2.2 Technique

2.2.1 Collision Kinematics

The technique of MEIS is reliant on the fact that a collision occurring between an incident ion and an atom can be modelled using classical mechanics to describe a binary collision between the two particles. For this model it is necessary to make the following three assumptions:

1. The kinetic energy transferred to the atom during a collision, (typically ≥ 100 keV for MEIS experiments), is large in comparison to the lattice binding energy of the atom, typically < 10 eV.

2. The time period of each collision is short, $\sim 10^{-15}$ s, in comparison to the period of characteristic lattice vibrations, $\sim 10^{-12} - 10^{-13}$ s, so that the target atom can be regarded to be stationary as the ion collides.

3. The collision is considered to be purely elastic and thus all energy transferred is kinetic.

It has been shown experimentally [6, 7] that these assumptions are applicable to ions with an energy as low as 0.5 keV, so clearly for the much higher energies used in MEIS experiments the assumptions are valid, and it is indeed reasonable to consider the system as a binary collision model, as represented by Figure 2.1. Using the basic principles of energy and momentum conservation it is possible to solve simultaneous equations to mathematically describe the scattering process.

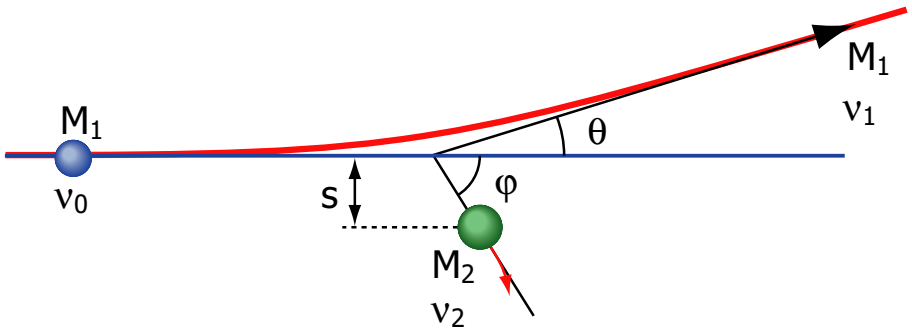

Figure 2.1: Kinematic scattering diagram for an ion interacting with a surface atom. Where M_1 = mass of incident ion; M_2 = mass of target atom; θ = scattering angle with respect to incident trajectory; φ = recoil angle of target atom with respect to trajectory of incident ion; s = impact parameter.

Given an incident ion of mass M_1 with initial velocity v_0, which is scattered at an angle θ with velocity v_1 after a collision with a particle of mass M_2, the ratio of the final energy of the incident ion (E_1) to initial energy (E_0) can be analysed to yield what is known as the kinematic factor equation (Equation 2.1), where A

is the ratio of the masses of the particles, $A = M_2/M_1$, and k is the kinematic factor.

$$\frac{E_1}{E_0} = \left(\frac{\cos\theta \pm \sqrt{A^2 - \sin^2\theta}}{(1+A)} \right)^2 = k \tag{2.1}$$

This equation shows that different elements will scatter a monoenergetic ion beam at different final energies and it is this fact that provides a basis for compositional analysis in MEIS. For any chosen scattering angle with a well-defined ion beam energy, it is possible to calculate the expected energy peak of a backscattered ion for any element.

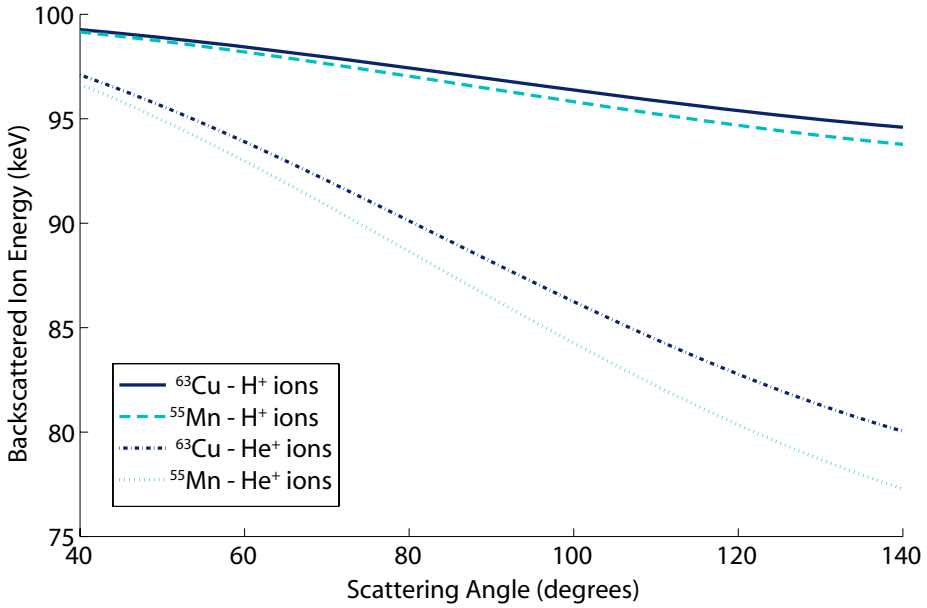

Figure 2.2: Plot of kinematic factor equation for Cu and Mn, each using two different ion beams (H^+ and He^+) with an incidence energy of 100 keV. This graph demonstrates how the energy of a backscattered ion depends on target atom mass, incident ion mass and scattering angle. It is clear that the resolution of Cu and Mn is poor using an H^+ ion beam, especially at low scattering angles.

In order to successfully analyse each elemental energy peak independently, a clear energy separation is necessary. This energy separation improves with increasing energy transfer to the surface atoms. Figure 2.2 shows how the backscattered

ion energy varies with scattering angle for two elements of similar mass for two different masses of incident ion. This plot demonstrates that energy separation can be poor for elements of similar mass with an H^+ beam, but is significantly improved by the use of the heavier He^+ beam. However, the use of heavier ions introduces other problems: the increased energy transfer to the surface provides greater potential for displacing surface atoms resulting in physical damage to the sample, especially for sensitive materials such as those containing light elements; and also ion neutralisation plays a greater role. For elements with a greater difference in mass it is possible to obtain the necessary energy separation to conduct MEIS experiments using an H^+ beam.

2.2.2 Rutherford Cross-Section

In addition to knowing the energy transferred in a collision, as described previously, in order to describe the scattering process it is also necessary to know the probability that an incident ion will be scattered at a particular angle to be able to determine the intensity of scattering at that point. This probability is known as the cross-section and depends strongly on the form of the interatomic potential.

In order to derive the cross-section, it can be assumed that the number of particles scattered into the solid angle $d\theta$ between angles θ and $\theta + d\theta$ is equal to the number of incident ions with corresponding impact parameters between s (defined as shown in Figure 2.1) and $s + ds$. For an intensity of incident particles, I, this gives rise to

$$2\pi I s|\mathrm{d}s| = 2\pi\sigma(\theta) I \sin\theta|\mathrm{d}\theta| \tag{2.2}$$

$\sigma(\theta)$ is known as the differential cross-section and by rearranging equation 2.2 can be written as

$$\sigma(\theta) = \frac{s}{\sin\theta}\left|\frac{\mathrm{d}s}{\mathrm{d}\theta}\right| \tag{2.3}$$

Using conservation of energy and linear momentum, it can be shown (see, for example [10]) that the scattering angle between the line of initial approach and

the final trajectory of the ion can be written as

$$\theta(s) = \pi - 2\int_{r_{min}}^{\infty} \frac{s\mathrm{d}r}{r\sqrt{r^2\left(1 - \frac{V(r)}{E}\right) - s^2}} = \pi - 2\Psi \tag{2.4}$$

where $V(r)$ is the potential of the central force, E is the initial energy of the ion, r_{min} is the distance of closest approach between the ion and the scattering centre and Ψ is the angle between r_{min} and line of initial approach, as shown in Figure 2.3. For

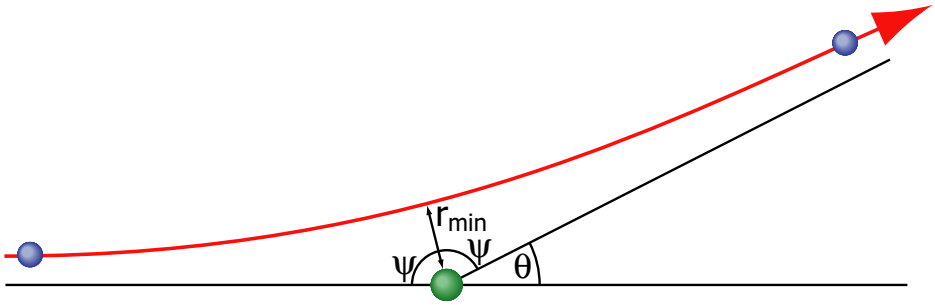

Figure 2.3: Diagram demonstrating the relation of orbit parameters and scattering angle

simple potentials, it is possible to solve this integral. In the case of ion scattering, the interaction is mainly between ion and nucleus and is therefore described by the Coulomb potential

$$V(r) = \frac{Z_1 Z_2 e^2}{r} \tag{2.5}$$

For this potential, the solution of the scattering integral is a hyperbola defined by

$$\frac{1}{r} = \frac{mZ_1Z_2e^2}{l}(\varepsilon\cos\theta - 1) \tag{2.6}$$

with eccentricity

$$\varepsilon = \sqrt{1 + \left(\frac{2Es}{Z_1Z_2e^2}\right)^2} \tag{2.7}$$

By consideration of the orbit geometry, the relationship between scattering angle and impact parameter can be shown to be

$$s = \frac{Z_1Z_2e^2}{2E}\cot\left(\frac{\theta}{2}\right) \tag{2.8}$$

Differentiating equation 2.8 and substituting into equation 2.3 yields the famous Rutherford cross-section, derived first in 1911 for the scattering of α particles from Au nuclei [11]

$$\sigma(\theta) = \frac{\left(\frac{Z_1 Z_2 e^2}{4E}\right)^2}{\sin^4\left(\frac{\theta}{2}\right)} \tag{2.9}$$

This equation led to the current nuclear model for the atom and is fundamental in current ion scattering techniques.

Equation 2.9 assumes a fixed centre of force. If instead, an elastic collision in the centre of mass frame is considered, then an analogous equation can be derived by inclusion of a factor to convert back to the laboratory frame of reference and by replacing the energy and scattering angles by their centre of mass counterparts [12]

$$\sigma(\theta)_{LAB} = \left[\frac{\left(\frac{Z_1 Z_2 e^2}{4E_{CM}}\right)^2}{\sin^4\left(\frac{\theta_{CM}}{2}\right)}\right] \times \left(1 - 2\left(\frac{M_1}{M_2}\right)^2 \sin^4\left(\frac{\theta}{2}\right)\right) \tag{2.10}$$

2.2.3 Scattering Potential

The Coulomb potential is used in the derivation of the Rutherford cross-section as this allows for direct integration of the scattering integral. However, this does not provide a completely accurate description of the scattering process in MEIS since the incident ion does not interact with the full charge of the atomic nucleus as the use of the Coulomb potential would imply. In actual fact, the force experienced by the scattered ion is reduced by electrons screening the ion from some of the nuclear charge, so it becomes necessary to add a screening function to accurately describe scattering behaviour.

For ions in the MEIS regime, this screening factor normally takes the form $\phi(\frac{r}{a})$, where r is the distance between the ion and the nucleus and a is a characteristic length in Gaussian units which defines the range of the screening effect. The

screening factor is multiplied by the original Coulomb potential

$$V(r) = \frac{Z_1 Z_2 e^2}{r}\phi\left(\frac{r}{a}\right) \tag{2.11}$$

Molière [13] has described a form for this screening function, and this is the one most commonly used in MEIS

$$\phi\left(\frac{r}{a_F}\right) = 0.35\exp\left(-\frac{0.3r}{a_F}\right) + 0.55\exp\left(-\frac{1.2r}{a_F}\right) + 0.10\exp\left(-\frac{6.0r}{a_F}\right) \tag{2.12}$$

where the screening length, a_F, is defined by Firsov, for the Bohr radius, a_0, [14]

$$a_F = 0.88534 a_0 \left(Z_1^{\frac{1}{2}} + Z_2^{\frac{1}{2}}\right)^{-\frac{2}{3}} \tag{2.13}$$

The other screening factor often used in ion scattering is the 'Universal Potential' developed by Ziegler *et al.* [15] based on fits to experimental data

$$\begin{aligned}\phi\left(\frac{r}{a_{ZBL}}\right) = {} & 0.1818\exp\left(-\frac{0.32r}{a_{ZBL}}\right) + 0.5099\exp\left(-\frac{0.9423r}{a_{ZBL}}\right) \\ & + 0.2802\exp\left(-\frac{0.4029r}{a_{ZBL}}\right) + 0.02817\exp\left(-\frac{0.2016r}{a_{ZBL}}\right)\end{aligned} \tag{2.14}$$

where the screening length, a_{ZBL}, is defined by

$$a_{ZBL} = 0.88534 a_0 \left(Z_1^{0.23} + Z_2^{0.23}\right)^{-1} \tag{2.15}$$

However, for the energy regime of MEIS experiments, there is minimal difference between the two screening factors, so generally the simpler Molière factor is used.

An alternative, computationally simpler, approach to calculating the cross-section is to multiply the Rutherford cross-section by a correction factor, F. The applicability of this method was demonstrated by L'Ecuyer *et al.* [16] and uses a simplified potential which is set to zero outside of the screening radius and is set to a series expansion of the exponentials of the screening factor, equation 2.12, inside the screening radius. Using these assumptions, the following correction term was obtained

$$F = 1 - \frac{0.042 Z_1 Z_2^{\frac{4}{3}}}{E_{CM}[\mathrm{keV}]} \tag{2.16}$$

Andersen *et al.* [17] suggested a different assumption in which the incident ion does not lose energy in the screened region. Instead, when it does scatter, it has larger energy than in the pure Rutherford scattering case since the effect of the electron cloud is to reduce the repulsive force of the nucleus and therefore the ion experiences less deceleration. This method determines the cross-section for an ion with an effective parameter, giving rise to

$$F_A = \left[1 + \frac{0.042 Z_1 Z_2 \left(Z_1^{\frac{2}{3}} + Z_2^{\frac{2}{3}} \right)^{\frac{1}{2}}}{E_{CM}[keV]} \right]^{-1} \tag{2.17}$$

Lee and Hart [18] conducted a study to investigate which of these correction factors is the most appropriate for ions in the MEIS energy range, by comparing various theoretical cross-sections with experimental values for a range of reduced energies, $\epsilon = \frac{E_{CM}}{V_1}$, $V_1 = 0.042 Z_1 Z_2^{\frac{4}{3}}$. This study demonstrated that the Andersen correction is accurate to within $1 - 2\%$ for $\epsilon > 3$. The correction of L'Ecuyer, equation 2.16, agrees within 2.5% for $\epsilon > 6$. This implies that for the purpose of this thesis, where the lowest reduced energy is 7.0 (obtained from He^+ scattering from Silver), the simpler correction of L'Ecuyer is valid. For systems with He^+ scattering from heavy atoms it may be necessary to use the Andersen correction to ensure a good approximation is made.

In practice, however, in the calculations used in this thesis, the scattering integral (equation 2.4) is solved numerically for a given potential within the simulations of the ion scattering process.

2.2.4 Energy Loss

Whilst the previous sections describe the interactions that occur when an ion scatters from an atomic nucleus, the majority of ions will not undergo such an interaction, due to the small cross-sections involved for a back-scattering event, and instead will experience small deflections and penetrate into deeper layers of the crystal. Each of these deflections, an elastic collision, will result in a loss of energy; the accumulation

of which is known as nuclear stopping. In addition to this, ions will lose energy through interactions with the electron cloud surrounding the target atom; which is known as electronic stopping. The combined effect is known as the 'stopping power' and results in a slow energy loss as an incident ion travels through the target crystal. For the energies involved in MEIS, the effects of nuclear stopping are negligible and the stopping power is dominated by electronic stopping.

The stopping power into and out of the target are almost identical and therefore can be considered equal such that $S_{in} \approx S_{out} \equiv S$. The energy of the ion as it leaves the crystal, E_{out} can then be described using the kinematic factor equation (equation 2.1) and deducting the energy loss, expressed in terms of the path length through the crystal, $l_1 + l_2$, and the stopping power, S,

$$E_{out} = k(E_0 - Sl_1) - Sl_2 \tag{2.18}$$

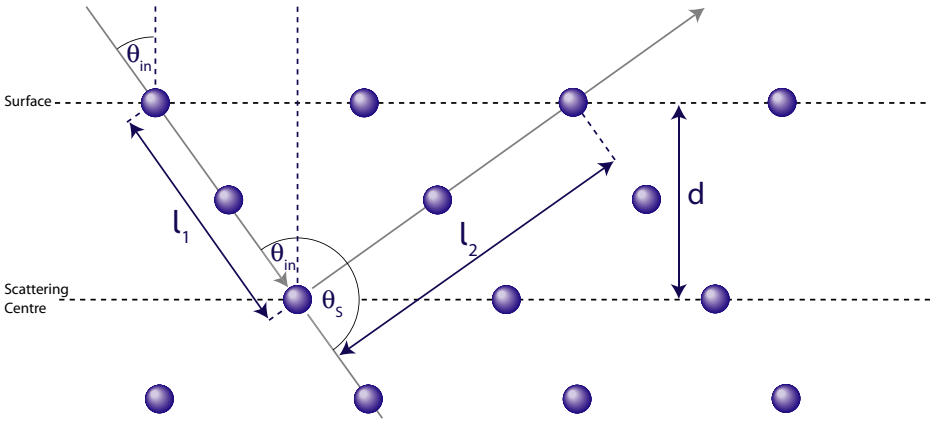

Figure 2.4: Diagram demonstrating how depth of a scattering event can be calculated from energy loss

Given an approximation for the stopping power it is possible, using equation 2.18 and basic trigonometry, to derive an equation which expresses the depth of a scattering event in terms of measurable parameters. It is this equation that makes MEIS a

useful tool in depth profiling

$$d = \left(\frac{kE_0 - E_1}{S}\right)\left[\frac{\cos\theta_{in}\cos(\pi - \theta_{in} - \theta_s)}{\cos\theta_{in} + k\cos(\pi - \theta_{in} - \theta_s)}\right] \tag{2.19}$$

Values for stopping powers can be obtained from the database developed by Ziegler *et al.* [19], Stopping and Ranges of Ions in Matter (SRIM).

2.2.5 Straggling

The SRIM database provides values for the average stopping power per unit distance for any given target material and incident ion energy. However, there is a spread of values in the losses for individual ions. This spread, known as straggling, is a Gaussian distribution of width Ω. From Bohr's theory of inelastic collisions with atomic electrons [20], the following assumptions are made:

1. The velocity of the ion is much greater than that of the orbital electrons in the target atoms.
2. The energy loss is very small in comparison to the total energy of the ion.
3. The target atoms are randomly distributed and no channelling is involved in the penetration process.

An expression for the energy straggling can then be obtained

$$\Omega^2_{Bohr} = 4\pi Z_1^2 Z_2 e^4 N \Delta R \tag{2.20}$$

where N is the number of target atoms per unit volume; e is the electron charge; ΔR is the thickness of the target.

The validity of assumption (2) applies in the majority of cases. Whilst channelling conditions are used for the experiments in this thesis, assumption (3) is considered valid since the channelling only affects the relative amplitude. However, for low and medium energies, assumption (1) is not satisfied. To solve this problem Bohr's theory can be extended by applying a correction factor to equation 2.20. Chu [21] utilised an improved model of electron density to perform a more complete

calculation of the straggling. Yang *et al.* [22] then produced empirical fits to the data of Chu to derive the following empirical function for the straggling effect

$$\Omega^2_{Chu} = \frac{\Omega^2_{Bohr}}{1 + A_1 E^{A_2} + A_3 E^{A_4}} \tag{2.21}$$

Where A_1, A_2, A_3, A_4 are parameters dependent on Z_2, listed in Yang *et al.* [22]; E is the energy of hydrogen ions (MeV/amu)

2.2.6 Neutralisation

The key principle in MEIS is based on being able to measure the absolute yield of backscattered ions. However, as an ion travels through a crystal there is a chance that it may experience a change in its charge. Ions may become neutralised, or ionised further, and neutral particles may become ionised. Since the electrostatic analyser only detects ions it is important to be able to quantify the proportion of incident ions which are measured after backscattering. As a result of this, much work has been done on investigating this problem. Most of this work has been conducted on LEIS where neutralisation is particularly problematic, but in the MEIS regime neutralisation should still be considered and the most notable work in this regime was by Kido *et al.* [23], in which empirical formulae were obtained fitting experimental data obtained by Marion and Young [24]:

$$f_+(E_{out}) = 0.17442(E_{out} - 10.2087)^{\frac{1}{3}} \text{ for } 30 - 150 \text{ keV } H^+ \text{ ions} \tag{2.22}$$

$$f_+(E_{out}) = 0.02045(E_{out} - 12.3388)^{\frac{2}{3}} \text{ for } 30 - 200 \text{ keV } He^+ \text{ ions} \tag{2.23}$$

where f_+ represents the ratio of positively charged ions emerging from the surface to the total of ions and neutrals.

These equations show that generally neutralisation depends only on the exit energy of the projectile from the surface and is independent of the target species. The exit energy is the important parameter because projectiles are neutralised and re-ionised continuously as they travel through the crystal and hence the final charge state of the particle is established in the near surface region where the particle has energy

E_{out}. Figure 2.5 shows that for 100 keV incident H^+ ions, used in the majority of this thesis, the fraction of ions backscattered to the detector is approximately 80%. For He^+ ions of the same energy, the ion fraction backscattered is roughly half of this value, at ∼40%.

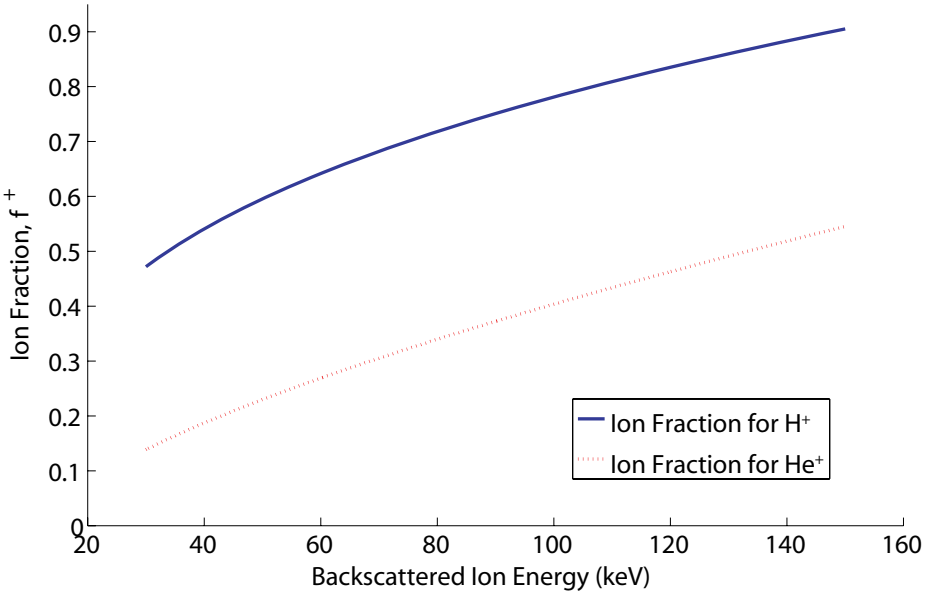

Figure 2.5: Graph showing how the fraction, f^+, of both H^+ and He^+ ions backscattered to the detector varies with the backscattered ion energy, calculated from Equation 2.22 and Equation 2.23

2.2.7 Shadowing/Blocking Leading to Surface Specificity

The previous sections have described how an ion undergoes small deflections as it comes close to an atom, and larger deflections as the impact parameter reduces. The result of this behaviour is that there is a region behind the atom, known as the shadow cone, which is impenetrable by the incident ion, see Figure 2.6. The region around the edge of the shadow cone experiences an enhanced ion yield, known as focussing.

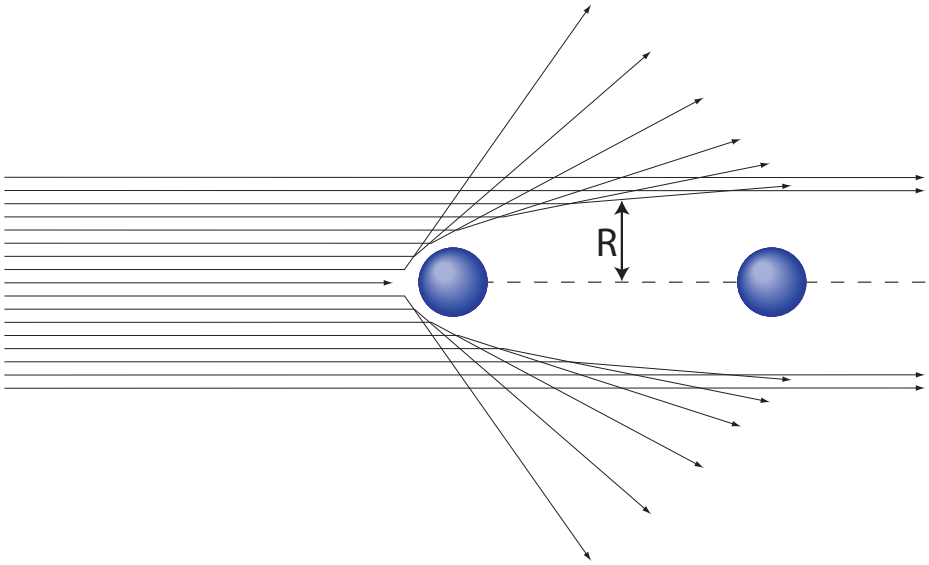

Figure 2.6: Ions are scattered from the first atom in a row creating a region behind the atom, known as the shadow cone, which is impenetrable by the incident ions; the edge of the shadow cone experiences an enhanced ion yield in an effect known as focussing.

The shadow cone radius, R, at a distance, l, behind the atom can be approximated by the radius, R_C, calculated analytically [12] using the unscreened Coulomb potential to give

$$R_C = 2\sqrt{\frac{Z_1 Z_2 e^2 l}{E}} \tag{2.24}$$

No such expression exists for R_M, the shadow cone radius for the Molière potential. Instead, numerical solutions can be found from universal curves which give the ratio $\frac{R_M}{R_C} = \xi$ for different combinations of incident ion and atom [25, 26]. Electronic screening reduces the range of the interaction and hence the true shadow cone radius, $R < R_c$.

Clearly, from equation 2.24, as energy increases the width of the shadow cone decreases; so for the energy range used in MEIS, shadow cones are relatively narrow allowing ions with impact parameters outside of the shadow cone to penetrate deep into the bulk. In MEIS, surface specificity is achieved by aligning the ion beam, and therefore the shadow cones, along major crystallographic directions,

known as channelling directions. Careful choice of the channelling directions allows illumination of different numbers of surface layers which enables layer by layer analysis of the crystal surface. Figure 2.7 demonstrates two channelling directions for an ideal, crystal lattice. However, atoms in a crystal are not ideally static, due to thermal vibrations. Section 2.2.1 demonstrated that an ion will interact with an atom considered to be stationary, therefore the effect of the thermal vibrations is that each ion will experience an interaction with atoms displaced at random from the lattice positions. This causes the shadowing to be imperfect and therefore deeper layers have a finite probability of interacting with the incident ion beam. For a nominal one layer incidence geometry at room temperature, the typical increase in backscattered ion yield is $\frac{1}{3} - \frac{1}{2}$ monolayers (ML).

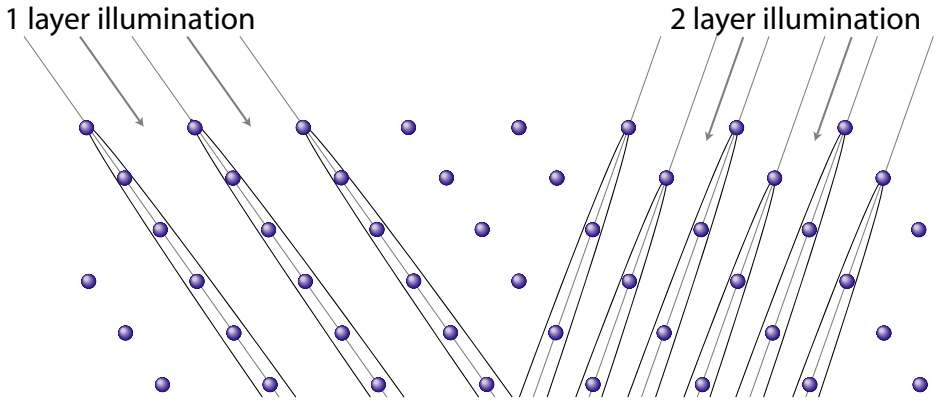

Figure 2.7: Ions aligned along crystallographic directions for one layer and two layer illumination, giving rise to surface specificity

Once ions have been backscattered from subsurface atoms, they can be blocked from reaching the detector by surface atoms, in a similar effect. This results in a decrease in backscattered ion yield measured by the detector along trajectories containing atoms, giving rise to 'blocking minima'. The cumulative effect is a blocking curve as demonstrated in Figure 2.8. The combination of alignment along a channelling direction and detection close to a blocking direction, both major crystallographic directions, is known as 'double-alignment'. Double-alignment maximises surface specificity and reduces background signal from ions backscattered by bulk atoms.

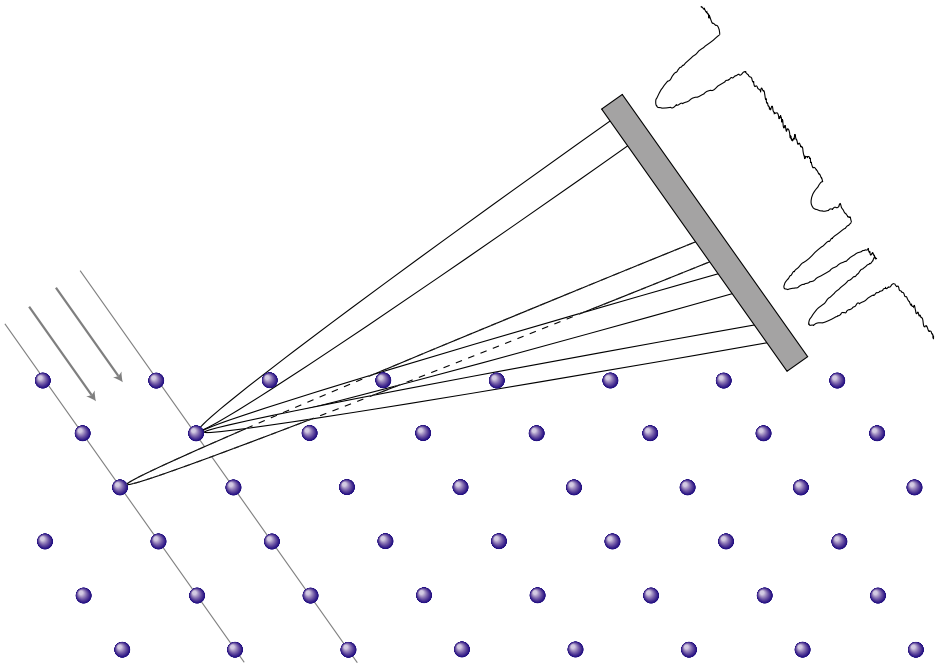

Figure 2.8: Ions enter the crystal lattice along a channelling direction. Once backscattered from subsurface layers, the ions are blocked from reaching the detector by atoms in the surface region. This results in blocking minima in the backscattered ion yield along trajectories containing atoms.

2.2.8 Surface Structure Determination

Given an experimentally obtained blocking curve, the shape and position of surface blocking minima can provide direct information about the relative positions and vibrational amplitudes of surface atoms. For example, surface relaxations will cause a shift in the scattering angle observed for surface blocking dips, in comparison to those expected for bulk like positions, see Figure 2.9. Using simple trigonometry it is then possible, for this simple case, to determine quantitatively a value for the relaxation

$$\frac{\Delta d}{d} = \frac{\tan(\alpha + \Delta\alpha)}{\tan\alpha} - 1 \tag{2.25}$$

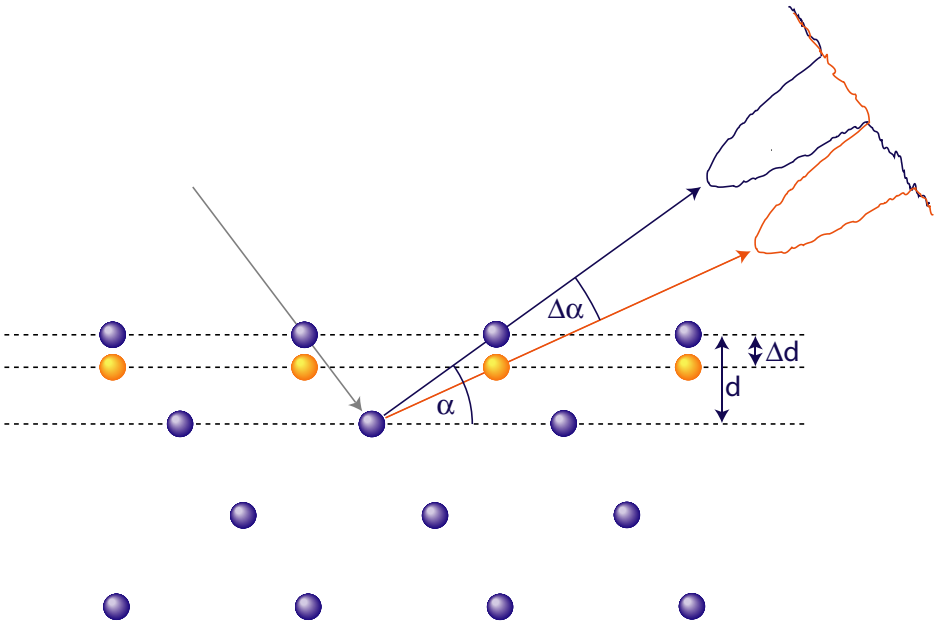

Figure 2.9: Surface relaxation leads to a shift in the angular position of the blocking dip. The dark blue atoms represent a bulk like termination, the pale orange atoms represent a relaxed surface giving rise to the two different blocking angles shown.

However, this simple approach is not feasible for the majority of cases since there are several factors affecting blocking curves, which must all be considered: vibrational amplitudes of surface atoms are usually larger than for bulk atoms; and a reconstructed surface, in which the surface atoms are removed from bulk-like positions, will lead to an enhanced yield in backscattered ions due to the fact that shadowing of the subsurface atoms will become less effective. As a result of this, most surface structures must be solved by producing simulations of the blocking curves, for a predicted surface model, and comparing these to experimentally obtained data.

2.2.9 Simulation

Simulations of MEIS blocking curves are produced for trial models using the 'VEGAS' code [27], which is based on Monte Carlo calculations. The theory behind these simulation codes are described in this section.

One method for producing theoretical curves would be to fully simulate the experiment and follow a large number of ion trajectories through the crystal and record every interaction with an atom. However, due to the very small probability of backscattering occurring, most of the calculated trajectories are of no interest and serve only to increase computation times to the point where the calculations are impractical.

Barrett [28] suggested an alternative method for modelling channelling by determining the probability that a particular atom will be hit by the incident ion beam, and then the probability that an ion scattered from the same atom will reach the detector. This method greatly reduces the required computation time for simulations. Barrett stated a number of assumptions required for the calculations, of which the following are particularly important to consider:

1. The motion of the ions is treated classically. This was shown to be a valid assumption by Lindhard [29].

2. For channelling calculations, in the majority of cases, the starting points for trajectories are selected at random over the surface of the crystal by means of a random number generator. However, for special purposes start points may be selected in other ways.

3. For blocking calculations, trajectories start from the position of a lattice atom, this may be either at rest or at a position determined by thermal vibrations.

4. Thermal vibrations can be simulated by giving each lattice atom a random displacement chosen from Gaussian distributions based on the Debye theory of thermal vibrations.

5. The interaction potential used can be in any desired form, although typically the Molière potential is used.

6. As an ion moves through the lattice, it can be assumed that it has only one important interaction at a time. It is then possible to create a table

of deflection as a function of impact parameter and then look up the value for each interaction. This saves a lot of computational time.

7. Energy losses by ions are neglected in the calculations as these are generally expected to have little effect unless either energy losses are specifically being investigated or a large fraction of energy is lost by the ion during its passage through the crystal. In many calculations, the average ion energy along its path is used rather than its initial energy.

8. The nuclear encounter probability is given by the cross-section for the process multiplied by the integral of the ion flux times the probability of a lattice atom being at the point of passage.

Tromp *et al.* [30] and Frenken *et al.* [31] then applied some new approaches to the work conducted by Barrett [28] in order to further improve computational efficiency of the VEGAS code which is used in MEIS. VEGAS is based on calculating the scattering probability, $Y_i(\boldsymbol{e}_1, \boldsymbol{e}_2)$, defined as the average probability that ions incident along the trajectory $\boldsymbol{e}_1$ will backscatter from atom i and subsequently be detected in the direction of $\boldsymbol{e}_2$, see Figure 2.10, with Y_i normalised to equal unity if shadowing and blocking effects are absent.

Let $G_i(\boldsymbol{x}_i)$ be the probability that atom i is located at position $\boldsymbol{x}_i$; $F^1(\boldsymbol{e}^1, \boldsymbol{x}_i)$ is the probability that incoming ions reach location $\boldsymbol{x}_i$; and $F^2(\boldsymbol{e}^2, \boldsymbol{x}_i)$ the corresponding probability that ions scattered from location $\boldsymbol{x}_i$ reach the detector. Then integrating over all positions of $\boldsymbol{x}_i$ gives

$$Y_i(\boldsymbol{e}^1, \boldsymbol{e}^2) = \int \mathrm{d}^3\boldsymbol{x}_i F^1(\boldsymbol{e}^1, \boldsymbol{x}_i) G_i(\boldsymbol{x}_i) F^2(\boldsymbol{e}^2, \boldsymbol{x}_i) \tag{2.26}$$

This expression can be simplified by using the fact that if $\boldsymbol{e}^2$ is random (i.e no blocking effects), equation 2.26 becomes an expression for the hitting probability, H_i, of atom $\boldsymbol{x}_i$

$$H_i \equiv Y_i = \int \mathrm{d}^3\boldsymbol{x}_i F^1(\boldsymbol{e}^1, \boldsymbol{x}_i) G_i(\boldsymbol{x}_i) \tag{2.27}$$

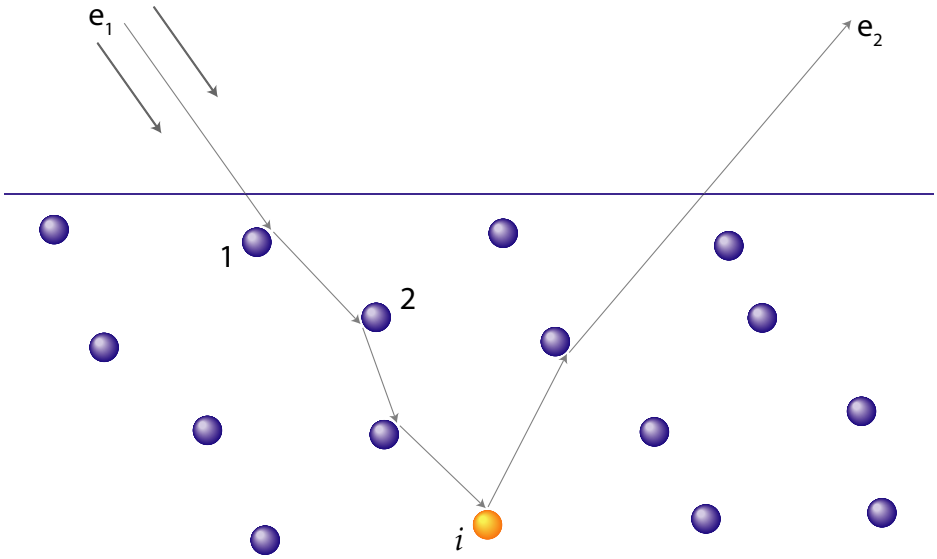

Figure 2.10: An ion trajectory through a crystal lattice. The ion experiences small deflections from atoms, which are displaced by thermal vibrations, before being backscattered by atom i (pale yellow)

and if $\boldsymbol{e}^1$ is random (i.e no shadowing of atom $\boldsymbol{x}_i$), equation 2.26 becomes an expression for the detection probability, D_i, of atom $\boldsymbol{x}_i$

$$D_i \equiv Y_i = \int \mathrm{d}^3\boldsymbol{x}_i F^2(\boldsymbol{e}^2, \boldsymbol{x}_i) G_i(\boldsymbol{x}_i) \tag{2.28}$$

Equation 2.26 is then approximated by

$$Y_i \approx H_i D_i \tag{2.29}$$

Given assumption (7) (that the ion experiences no energy losses as it traverses the crystal) the incident and outgoing parts of the ion trajectory are reversible in time, with H_i and D_i equivalent. Therefore the calculation needs only to consider hitting probabilities.

If an ion enters a solid at position, $\boldsymbol{x}_0$, and experiences small deflections by atoms 1 to $i-1$ before being backscattered by atom i, with the ion track approaching the equilibrium position of atom i, $\boldsymbol{\xi}_i$, then the probability that a trajectory of this type

occurs is

$$G_1(\boldsymbol{x}_1)G_2(\boldsymbol{x}_2)\cdots G_{i-1}(\boldsymbol{x}_{i-1})G_i(\boldsymbol{x}_i) \tag{2.30}$$

and the probability that atom i lies in the path of the ion track is $g_i(\boldsymbol{\xi}_i)$. Then, integrating over all possible ion impingement positions, $\boldsymbol{x}_0$, in the surface plane and over all possible positions for the atoms 1 to $i-1$ the hitting probability of atom i is given by

$$H_i = \int\cdots\int \mathrm{d}^2\boldsymbol{x}_0\left[\prod_{j=1}^{i-1}\mathrm{d}^3\boldsymbol{x}_j G_j(\boldsymbol{x}_j)\right]g_i(\boldsymbol{\xi}_i) \tag{2.31}$$

This integration is only possible for simple cases involving just a few atoms. For the more complicated cases, which are normally required, equation 2.31 is evaluated by summing the integrand over a large number of random samples, with sampling distribution function, $\Gamma_j(\boldsymbol{x}_j)$, to obtain

$$H_i = \frac{1}{\Phi}\sum_{\Gamma}\left[\prod_{j=1}^{i-1}\frac{G_j(\boldsymbol{x}_j)}{\Gamma_j(\boldsymbol{x}_j)}\right]g_i(\boldsymbol{\xi}_i) \tag{2.32}$$

where the density, Φ, of impingement positions $\boldsymbol{x}_0$ in a plane perpendicular to $\boldsymbol{e}_1$ is used to normalise H_i to unity when atom i is not shadowed. Division by $\Gamma_j(\boldsymbol{x}_j)$ ensures the result is independent of the sampling distribution function. In conventional Monte Carlo calculations, $\Gamma_j(\boldsymbol{x}_j)$ is chosen to be equal to the position distribution function, $G_j(\boldsymbol{x}_j)$ in order to enhance efficiency of the simulations by simplifying equation 2.32 to

$$H_i = \frac{1}{\Phi}\sum_{G} g_i(\boldsymbol{\xi}_i) \tag{2.33}$$

The VEGAS simulations use this to calculate ion trajectories for any specified number of ions at a given incidence direction and produce simulated blocking curves.

2.2.10 R-factor Analysis

When comparing simulated blocking curves to experimental data, it is neither sufficient nor practical to judge simply by eye which of the calculated data give the best reproduction of the features of the experiment. Visual inspection can help to ascertain which of the trial structures gives something close to the experimental

data, but to distinguish between more similar simulations it is necessary to employ the use of a reliability factor (R-factor) which provides a statistical comparison between the theoretical and experimental curves.

A number of different R-factors exist, and some work has been done investigating the most appropriate form for MEIS analysis [32, 33]. The general conclusion is that a reduced chi-squared R-factor is the most appropriate to use

$$R_\chi = \left(\frac{1}{N}\right) \sum_i^N \left[\frac{(I_{exp} - \lambda I_{theo})^2}{I_{exp}}\right] \tag{2.34}$$

where I_{exp} is the experimentally obtained backscattered ion yield at a particular scattering angle; I_{theo} is the number of layers visible as calculated by VEGAS, which must be multiplied by a scaling factor, λ, to convert into the corresponding number of counts; N is the number of points in the data. This R-factor compares the actual number of backscattered ions, without angular correction for the cross-section, which results in the data from lower scattering angles having a greater influence on the R-factor than data from high scattering angles.

In most cases, MEIS structural analysis is conducted using a number of different scattering geometries to enable layer by layer analysis. In this case, an overall R-factor, R_T can be found by calculating individual R-factors, R_i, for each dataset, i, using equation 2.34, and applying a weighting to reflect the number of points, N_i, in each of the sets of data [34]

$$R_T = \frac{N_1 R_1 + N_2 R_2 + \cdots + N_n R_n}{N_1 + N_2 + \cdots + N_n} \tag{2.35}$$

Due to the fact that the chi-squared R-factor is calculated using raw counts, the variance of the R-factor associated with a particular structural parameter, Z, can be determined simply using the following [35]

$$\sigma^2 = \frac{2}{\left(\frac{\mathrm{d}^2 R_\chi}{\mathrm{d}Z^2}\right)_{R=R_{min}}} \tag{2.36}$$

This calculated variance can then be used to determine an acceptable range of values for the parameters under investigation.

Chapter 3

Experimental Method

3.1 Supporting Techniques

Whilst the majority of the work in this thesis is conducted using ion scattering techniques, it has been clear for some time that it is rare to be able to deduce all required information on a surface using one technique alone. There are three main areas of interest in a surface: chemical composition; atomic structure and electronic structure. In most cases it is necessary to obtain some minimal information in each of these areas in order to characterise a surface, and therefore it is usual to use a combination of techniques.

The two most commonly used supporting techniques are low energy electron diffraction (LEED), which provides characterisation of the long range order of a surface, and Auger electron spectroscopy (AES), which gives details of chemical composition and is used, in particular, to test the cleanliness of a surface. These two techniques were indeed used in combination with MEIS in order to characterise surfaces for the purpose of this thesis. MEIS relies on fundamentally different physical principles to many other surface science techniques, including LEED and AES so using the three in combination provides strong complementary characterisation.

3.1.1 Auger Electron Spectroscopy

The Auger electron spectroscopy technique for chemical analysis of surfaces is based on the Auger radiationless process. When a core level of a surface atom is ionised by an impinging electron beam, typically in the range $1 - 10$ keV, the atom may decay to a lower energy state through an electronic rearrangement which leaves the atom in a doubly ionised state. The energy difference between these two states is given to the ejected Auger electron, see Figure 3.1, which will have a kinetic energy, KE, characteristic of the parent atom. Where

$$KE = E_A - E_B - E_C \tag{3.1}$$

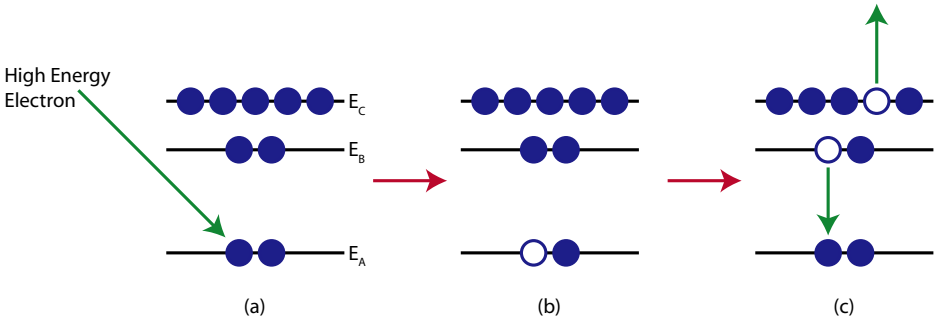

Figure 3.1: Energy level diagram to show the process that produces an Auger electron. A high energy electron ionises a core level of an atom (a), leaving the atom in an excited state (b), the atom decays to a lower energy state via an electron from a higher energy level filling the core level hole. This liberated energy causes the ejection of a third, Auger electron (c).

When the Auger transitions occur within a few angstroms of the surface, the Auger electrons may be ejected from the surface without loss of energy and give rise to peaks in the secondary electron energy distribution function. Equation 3.1 shows that the energy of the emitted electrons are independent of the incident beam energy and therefore the energy (and also shape) of these Auger features can be used to unambiguously identify the composition of the solid surface. For the work conducted in this thesis, AES is used in most part in the preparation of crystals to confirm that there are no contaminants on the surface.

An Auger electron spectroscopy system consists of an ultra-high vacuum system (UHV), an electron gun for specimen excitation, and an energy analyser for detection of Auger electron peaks in the total secondary electron distribution. The use of incident electrons means that Auger peaks are superimposed on a rather large continuous background, but they can be more easily detected by differentiating the energy distribution function N(E), which suppresses the background and allows amplification of the Auger peaks. Thus the conventional Auger spectrum is the function dN(E)/dE , an example spectrum can be seen in Figure 3.2.

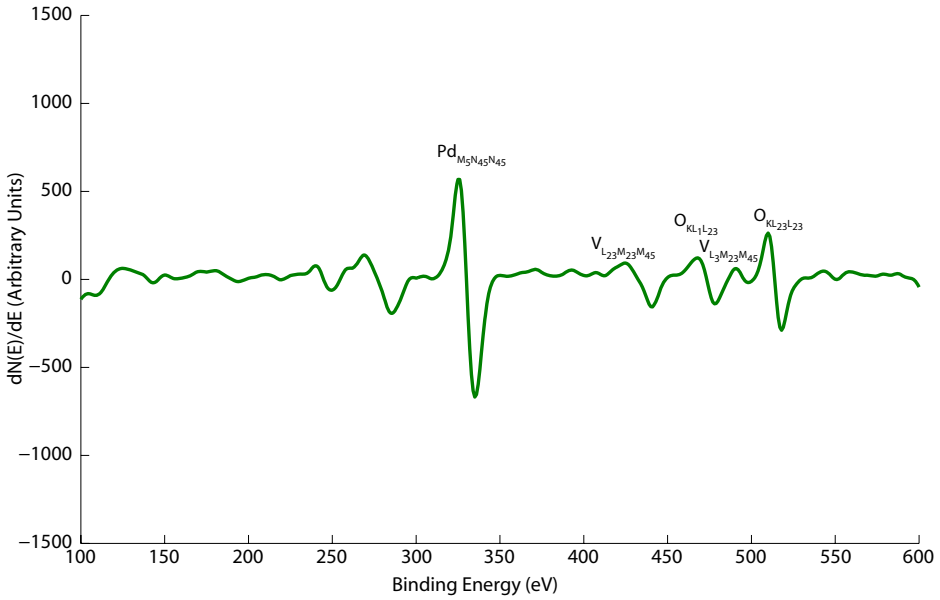

Figure 3.2: An example Auger spectrum, showing the differentiated intensity, dN(E)/dE, of the Auger electron peaks for a sample consisting of a thin V_2O_3 film grown on Pd(111)

AES can also be used as an indication of deposition rate of a source. The peak-to-peak magnitude of an Auger peak in a differentiated spectrum is directly related to the surface concentration of the element which produces the Auger electrons. In a simple case of species A being deposited onto species B at a constant rate, R, and assuming perfect layer by layer growth. Then, whilst the first ML is deposited, the magnitude of the differentiated peak of A will increase linearly. Once the first

layer is complete, the second layer will form, once again with a linear increase in magnitude of peak A, but at a different rate. If $|A|$ and $|B|$ are the peak to peak magnitudes of species A and B respectively, then by plotting the ratio,

$$\frac{|A|}{|A|+|B|} \tag{3.2}$$

against time, a change in gradient can be seen at the completion of each ML which can be used to determine the deposition rate. The mean-free-path of the Auger electrons is only a few angstroms, so after three or four layers of species A have been deposited, the peak observed from species B will disappear and only electrons from species A will be detectable and therefore the gradient of this plot will plateau at this point.

3.1.2 Low Energy Electron Diffraction

The origins of LEED are one of the oldest amongst surface science techniques. The first electron diffraction experiment was performed in 1927 by Davisson and Germer [36], using equipment that was later developed into the modern LEED system. However little interest was given to the use of the low energy electron diffraction experiment at the time due to the small sample penetration achieved by low energy electrons, allowing only the outer layers (contaminated by air) to be investigated. With the advent of UHV technologies and better crystal preparation in the 1960s, the original disadvantage of LEED became its greatest success - the high degree of surface sensitivity make LEED an ideal surface science technique [37, 38].

The range of energy, E, used in LEED ($30 - 300$ eV) gives rise to an electron wavelength, λ, of ~ 1 Å, by use of the de Broglie relationship,

$$\lambda = \sqrt{\frac{150.4}{E(\text{eV})}} \tag{3.3}$$

This wavelength is comparable to the magnitude of interatomic distances in a crystal lattice, hence diffraction of the electrons occurs. The mean-free-path for inelastic scattering in this energy range is very short, typically around 5 Å, hence

the diffraction process involves only the surface. Therefore LEED can describe the diffraction of electrons by making use of the conservation of energy in a 2-D periodic system,

$$|\mathbf{k'}_{\parallel}|^2 + |\mathbf{k'}_{\perp}|^2 = |\mathbf{k}_{\parallel}|^2 + |\mathbf{k}_{\perp}|^2 \tag{3.4}$$

where $\mathbf{k}_{\parallel}$ is the component of the incident wavevector parallel to the sample surface; $\mathbf{k}_{\perp}$ is the component of the incident wavevector perpendicular to the sample surface; $\mathbf{k'}_{\parallel}$ is the component of the reflected wavevector parallel to the sample surface and $\mathbf{k'}_{\perp}$ is the component of the reflected wavevector perpendicular to the sample surface. The conservation of reduced electron wavevector (momentum) in a 2-D periodic system is given by,

$$\mathbf{k'}_{\parallel} = \mathbf{k}_{\parallel} + \mathbf{g}_{hk} \tag{3.5}$$

where the reciprocal net vector

$$\mathbf{g}_{hk} = h\mathbf{a}^* + k\mathbf{b}^* \tag{3.6}$$

where h, k are integers and, for primitive lattice vectors, $\mathbf{a}$ and $\mathbf{b}$, and unit surface normal, $\mathbf{n}$, the primitive translation vectors of the 2-D reciprocal lattice of the surface, $\mathbf{a}^*$ and $\mathbf{b}^*$, are given by:

$$\mathbf{a}^* = 2\pi\left[\frac{\mathbf{b} \wedge \mathbf{n}}{\mathbf{a} \cdot \mathbf{b} \wedge \mathbf{n}}\right] \tag{3.7}$$

$$\mathbf{b}^* = 2\pi\left[\frac{\mathbf{n} \wedge \mathbf{a}}{\mathbf{a} \cdot \mathbf{b} \wedge \mathbf{n}}\right] \tag{3.8}$$

These conservation equations can be conveniently represented using the Ewald Sphere construction [2]. The diffraction pattern observed in LEED is a projection of the reciprocal net of the surface, $\mathbf{g}_{hk}$, scaled according to the incident electron energy.

LEED can be used quantitatively, known as LEED-I(V), to determine surface structures, by measuring the changes in intensity of particular diffraction spots with the change of energy, giving rise to I(V) curves. However, for the purpose of this thesis, LEED is used only qualitatively as an indication of a well-ordered

surface and to aid identification of overlayer structures. A sample that has very good translational symmetry will produce a diffraction pattern with sharp, bright spots and an uncontaminated surface will produce little background, so a crystal can be judged to be well-ordered when both of these criteria are satisfied. An overlayer structure with a larger unit mesh in comparison to the substrate will lead to fractional order spots appearing in the LEED pattern and allows qualitative interpretation of the structures present.

A schematic of a typical LEED optic is shown in Figure 3.3. The electrons are produced by an electron gun, using a high temperature thermionic source, in a well collimated (parallel to within better than 1°), monoenergetic (to within 0.5 eV) beam. The sample is mounted at the centre of a number of hemispherical grids.

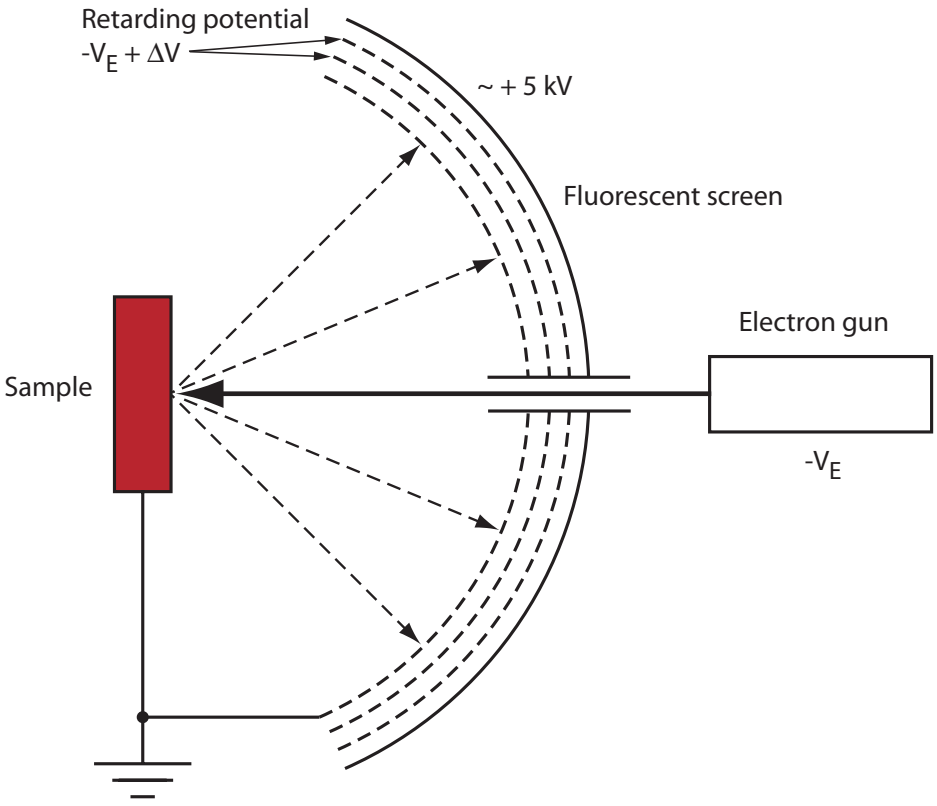

Figure 3.3: Schematic diagram of a typical low energy electron diffraction optic

Once scattered from the surface, the electrons travel directly in the field free region created between the sample and the inner hemispherical grid, G_1, which are both connected to a common ground. The outer grids, G_2 and G_3, are given a potential slightly below the incident beam voltage, which acts to retard electrons which have not been elastically scattered; since it is only these that are coherent and hence form a diffraction pattern. Those electrons which get through the grids (normally those which have lost less than $1 - 2$ eV of their original energy) are accelerated towards the screen, typically biased at ~ 5 kV, to give the electrons enough energy to excite the phosphor and allow the diffraction pattern to be seen. An example LEED pattern can be seen in Figure 3.4

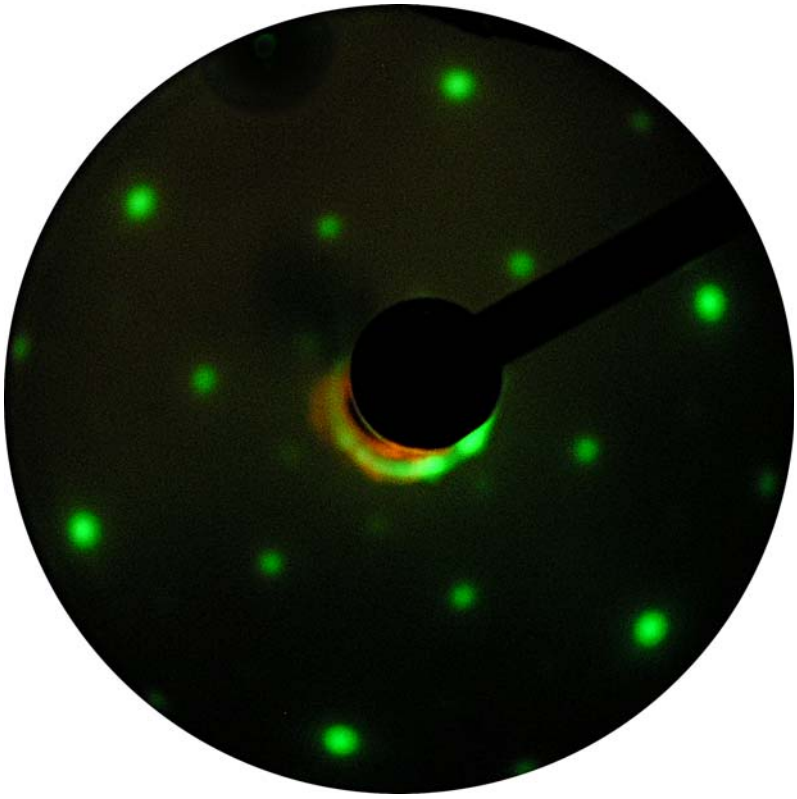

Figure 3.4: Example of an experimentally obtained LEED pattern. This $\sqrt{3} \times \sqrt{3}$ pattern is obtained from a thin V_2O_3 film grown on Pd(111) with an incident beam energy of 56 eV

3.2 Daresbury MEIS Facility

The MEIS experiments were conducted at the UK MEIS facility located at Daresbury Laboratories. This facility, commissioned in 1996, consists of an ion source, producing positively charged ions; a beamline for transporting the ion beam; and a multi-chamber ultra-high vacuum end station. The end station consists of a main chamber where the scattering experiments take place; a storage chamber capable of storing up to six samples under UHV; a preparation chamber with surface characterisation capabilities and able to mount several deposition sources of many different types; a fast entry load-lock chamber; and a sample transfer system allowing samples to be moved freely, under continuous vacuum conditions, between the chambers. A schematic of the facility can be seen in Figure 3.5

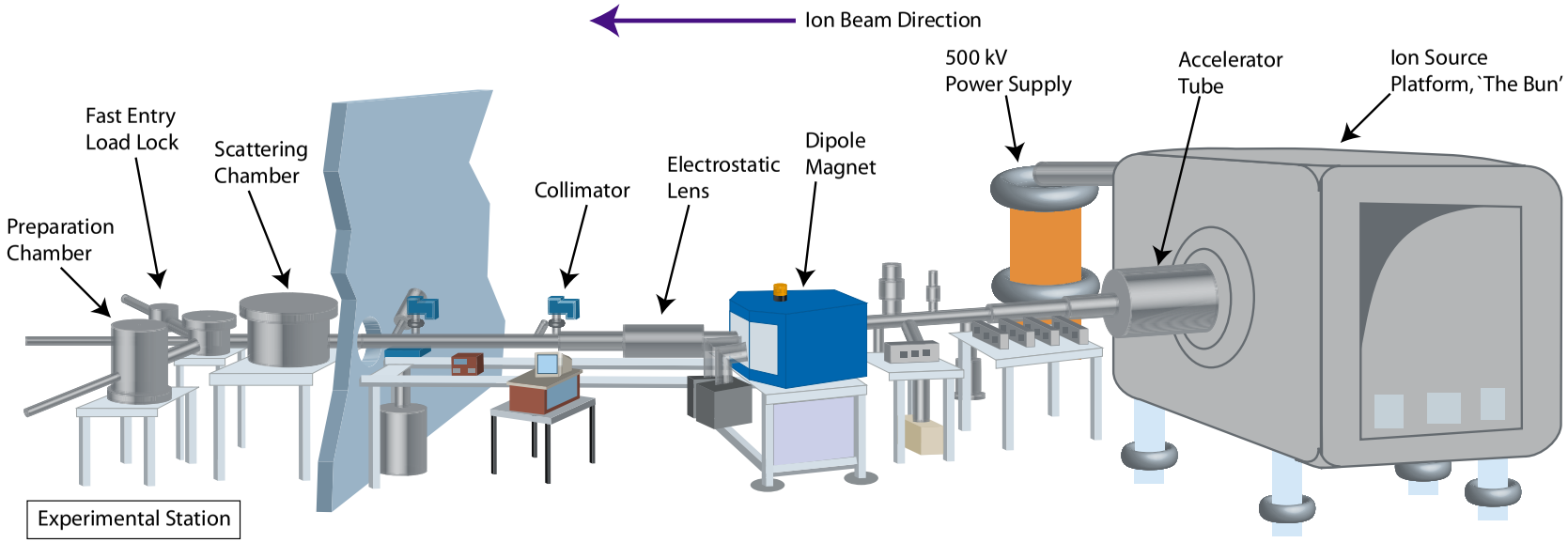

Figure 3.5: Schematic diagram of the UK MEIS facility at Daresbury. Ions are created in 'the bun' and from there travel along the beamline towards the experimental station.

3.2.1 Beam Line / Ion Source

The beam of ionised gas at the UK MEIS facility is generated using a High Voltage Engineering Europa (HVEE) hot cathode duoplasmatron source, which is located in an isolated platform known as 'the bun'. The duoplasmatron source creates a low pressure arc discharge in the gas to be ionised, which is electrostatically constricted by a funnel shaped intermediate electrode placed between an electron emitting hot filament (cathode) and the anode. A strong axial magnetic field between the intermediate electrode and the anode constricts the discharge further, creating a narrow plasma beam in line with the exit aperture (for further details, see [39, 40, 41]). It is theoretically possible to ionise any elemental gas in this way, but typically either hydrogen or helium are used for MEIS experiments, because they are less destructive of the samples.

Once the ionised gas has been created, it is extracted from the source by a 20 kV potential giving rise to a total accelerating voltage of the source HT plus 20 kV. Therefore, for the typical 100 keV ion beam, the voltage in the bun must be 80 kV for singly charged ions. The ions created will emerge from the source with a range of energies depending on the position at which they were produced.

After leaving the bun, the ionised gas enters the beamline via a linear accelerator, which delivers ions to the scattering chamber in the energy range $50 - 400$ keV. The beamline consists of components which focus, steer and define the ion beam. The settings of some components must be regularly optimised in order to maintain a good ion beam. The beam is mainly focussed by two electrostatic quadrupole triplets (EQTs), one of which lies before a bending magnet (designed to allow only singly charged ions through), the other after. Electrostatic steerers are positioned along the beamline in order to align the beam through two sets of defining slits before entering the scattering chamber. The vertical (Y) steerers are often adjusted as this affects the focussing of the EQTs. The defining slits are not normally adjusted but can be changed in order to improve resolution of the ion beam, and hence of the

data acquired.

3.2.2 Experimental Chambers

The end station consists of four interlinking chambers between which samples can be transferred whilst maintaining vacuum. The chambers are separated from each other by manually operated Viton gate valves. The three UHV chambers, namely the preparation chamber; storage chamber and main chamber, are pumped with turbo molecular pumps (TMPs) and titanium sublimation pumps (TSPs) achieving base pressures of $\sim 3{\times}10^{-10}$ mbar for the preparation chamber; and $\sim 1 \times 10^{-10}$ mbar for the storage and main chambers. After venting any of the chambers, UHV pressures are achieved by baking the relevant chamber to 150 °C for an appropriate time, typically: $24 - 36$ hrs for the preparation and storage chambers; and $30 - 48$ hrs for the main chamber. The bake is followed by careful outgassing of all the filaments. A schematic diagram of the arrangement of the chambers is shown in Figure 3.6. Samples enter into the experimental chambers via the fast-entry load lock, and from here can be transferred into the storage chamber in less than 30 min. The load-lock can achieve base pressures of 3×10^{-7} through pumping with a TMP. The load-lock also contains basic heating facilities allowing samples and sample holders to be degassed before entering the UHV system.

The storage chamber contains a carousel capable of holding up to six samples at any one time. One of the sample holder positions contains facilities for e-beam heating and thermocouple temperature measurements.

The preparation (prep) chamber has facilities for ion bombardment sputtering and e-beam heating, which are used for cleaning samples. There are several portholes on the prep chamber to which various deposition sources can be mounted and the chamber houses a rear view LEED and AES in order to characterise the prepared samples. The sample temperature can be measured via a thermocouple or a pyrometer depending on the required application.

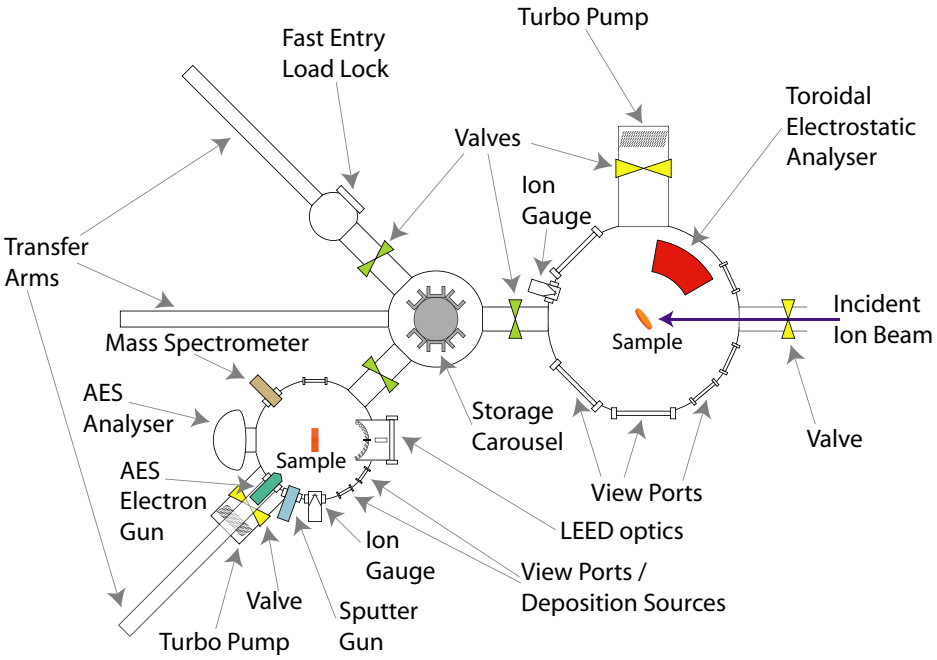

Figure 3.6: Schematic diagram showing the plan view of the arrangement and facilities of the experimental chambers in the end station. Samples enter the UHV system through the fast entry load lock (top left) and from there transferred to the central storage chamber. Samples can then enter either the main experimental chamber (right) for MEIS data acquisition or the preparation chamber (bottom left) for surface preparation and characterisation.

The main chamber, which is separated from the beamline via a pneumatic Viton gate valve, contains a beam defining aperture at the end of the beamline and a beam current monitor, measuring a fixed amount (28.6 %) of the beam and thus readings from the monitor are equal to 0.4 of the current transmitted to the sample. The main chamber houses a high precision goniometer which can manipulate the sample to an accuracy of 0.1° in each of three degrees of rotation (spin, tilt and rotation, as defined in Figure 3.7) as well as translation in $x-$, $y-$ and $z-$ directions. Finally, the main chamber contains the toroidal electrostatic analyser (TEA), which is used to measure the ions after scattering from the sample, more details of this can be found in section 3.2.3

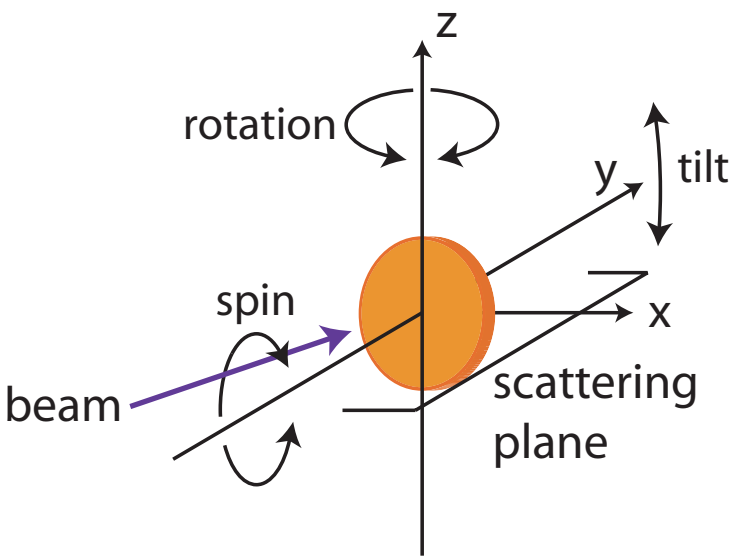

Figure 3.7: Schematic showing the three degrees of rotation and the translation directions of a sample housed in the high precision goniometer. The ion beam and backscattered ions lie within the x-y plane.

3.2.3 Toroidal Electrostatic Analyser

After scattering from the sample surface, ions enter into the toroidal electrostatic analyser [42], manufactured by HVEE, which is broadly similar to hemispherical analysers such as those used for electron detection in photoemission or Auger. The entrance slit of the TEA is a solid angle of $\sim 10^{-3}$ sr, limiting the rate of ions passing into the detector to 10^2 ions/s. The ions are then deflected through 90° by the field created by a pair of toroidal plates, one with negative voltage the other positive, before passing into a position sensitive detector, see Figure 3.8

The pass energy, E_{pass}, for the ions is the central energy which can pass through the TEA, given by $E_{pass} = 0.06 \times V(\text{keV})$, where $\pm V$ are the voltages (kV) applied to the TEA plates. So, for 100 keV ions, a voltage of ±6 kV must be applied to the plates. The detector collects ions in an energy window which is $\sim 2\%$ of the pass energy; for 100 keV ions this gives an energy window of ~ 2 keV.

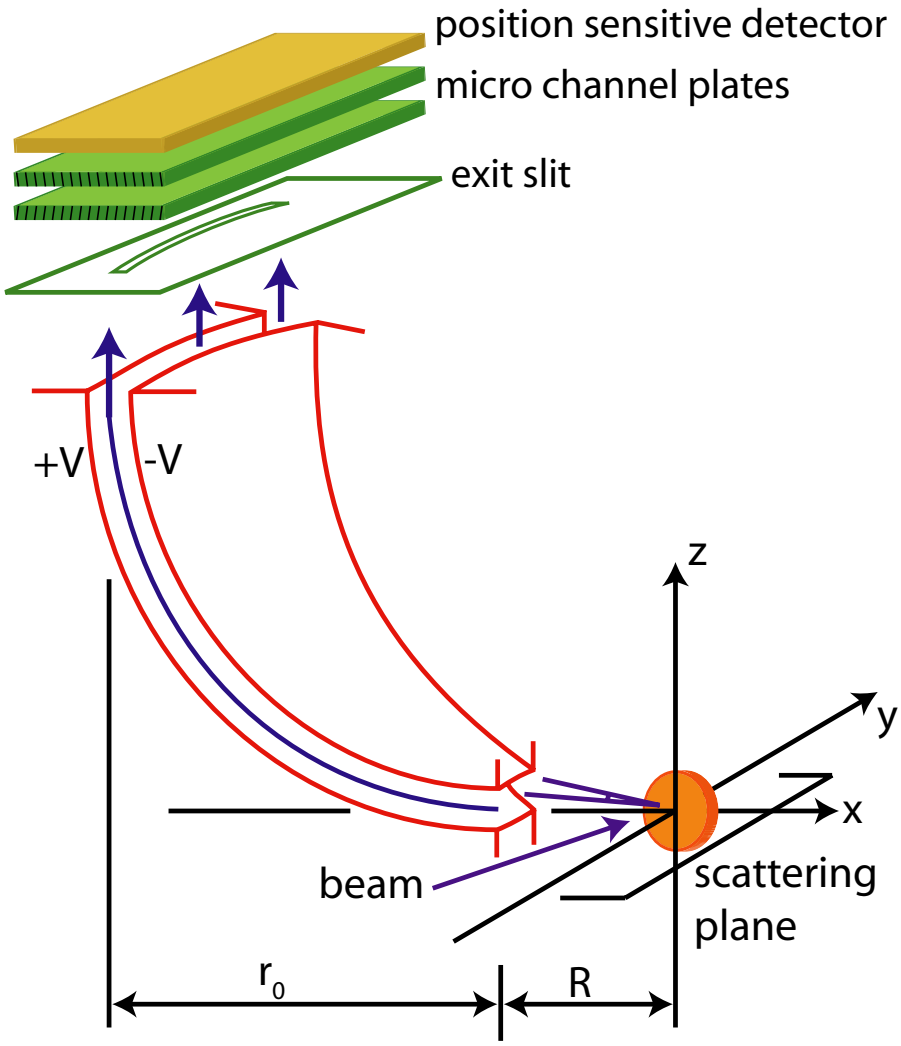

Figure 3.8: Schematic diagram of the toroidal electrostatic analyser. Scattered ions enter the TEA and are deflected through 90° onto a position sensitive detector capable of simultaneously measuring energy and scattering angle of backscattered ions

The design of the TEA means that it is rotationally symmetric about the scattering centre, so that ions scattered from the sample will maintain their scattering angle as they pass through the analyser, which is fundamental to the detection. The analyser is capable of detecting ions in an angular span of 27°, with a resolution of $< 0.01°$. However, due to fringing field effects at the edges of the window of detectable ions, the energy resolution dramatically decreases at the extremes of angle in this window and so a smaller angular span is used in reality.

The design of the analyser is such that certain important attributes are provided:

1. point to point imaging, where ions leaving the same point with the same energy but having different angles in the vertical direction ($z-$axis) are focussed onto the same point of the detector.

2. parallel to point imaging, where ions leaving the surface with the same energy and vertical angle but from different points are focussed onto the same point of the detector.

3. when ions enter the field free region after energy selection, their trajectories are parallel

Given these conditions, it is possible to make use of a position sensitive detector by means of micro channel plates to simultaneously determine the energy and angle of scattered ions. Points (1) and (2) are important for the position sensitive detector, whilst point (3) is necessary for the use of channel plates because they experience a steep decrease in detection efficiency for off-normal incidence.

3.2.4 Position Sensitive Detector

At the exit of the TEA, the ions pass through a fringing field slit, a beam defining slit and two micro-channel plates (MCPs) before entering into the detector itself. The design of the detector is similar to one used previously in angle-resolved electron spectroscopy [43]. The MCPs are mounted in a chevron formation with one angled at $+8°$ off the $z-$axis (which is normal to the detector), and the other angled at

$-8°$ [44][45]. The impinging ions create an electron cascade that is accelerated onto a 2-D position sensitive detector. This 2-D detector is, in fact, a combination of two different types of detector [46]: the first is a 'backgammon detector', which consists of a set of triangular gold electrodes; the second is a 'charge division detector', which divides the incident charge between electrical terminals using capacitor chains. See Figure 3.9.

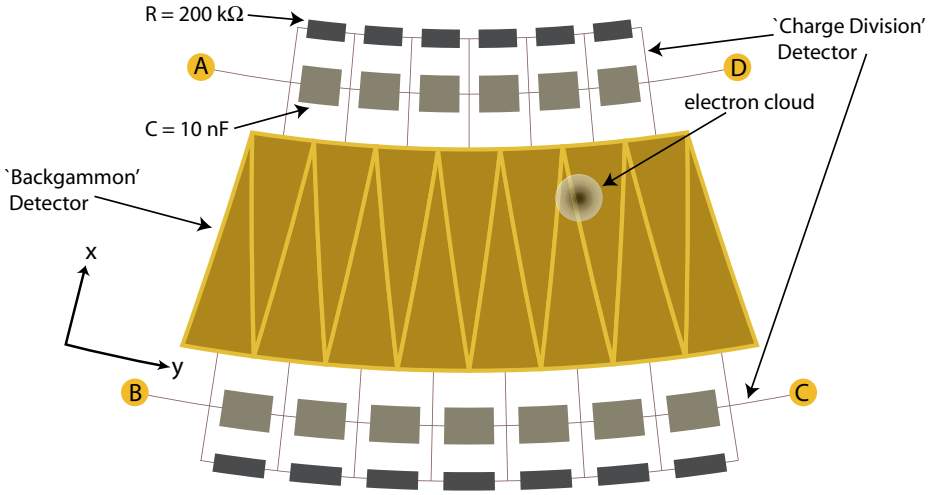

Figure 3.9: Schematic diagram of the position sensitive detector. An electron cloud impinging from the micro-channel plates hits two triangles of the 'backgammon detector' sending electric impulses to the four corners of the 'charge division detector', allowing the scattering angle and backscattered ion energy to be determined

The charge cloud (the diameter of which must be large enough to overlap more than one triangle on the backgammon detector) created by the MCPs hits the backgammon detector and the charge collected by each electrode then spreads along the capacitor chains to charge sensitive pre-amps located at the four corners of the detector. By measuring the electric impulses in the four corners, A−D, the exact $x-$coordinate (scattering angle) and $y-$coordinate (energy of scattered ion) of the centre of the electron cloud can be determined using:

$$\theta = \frac{A+B}{A+B+C+D} \tag{3.9}$$

$$E = \frac{B+C}{A+B+C+D} \tag{3.10}$$

The combined energy resolution of the detector and analyser is ~ 450 eV for a 100 keV H^+ beam of standard size ($z = 0.5$ mm), but can be increased to ~ 260 eV for a 'high resolution' beam size ($z = 0.15$ mm). The combined angular resolution of the detector and analyser is $\sim 0.3°$. Some distortions in both the energy axis and angular axis arise in the data acquired, but these can be corrected by comparing to data obtained from reference samples.

3.2.5 Data Acquisition

The 2-D detector produces four charge pulses which are amplified and shaped electronically to produce a 2-D data set, known as a tile, which is $\sim 27°$ wide. The data acquisition software collects data for a given preset integrated current arriving at the sample to allow consistency in the tiles obtained. After acquiring each tile, the analyser steps down through pass energies to collect 2-D tiles which span the required energy range and these tiles can be joined together to create a spectrum such as that shown in Figure 3.10. This example spectrum shows two regions with a high intensity of backscattered ions, which are known as 'surface peaks' (one for palladium and one for vanadium), each marked between a set of two red lines. Surface peaks arise in spectra when the ion beam is aligned to a crystallographic direction, which causes the majority of backscattered ions being scattered from surface atoms. A full angular range is required for experiments on surface crystallography, this is obtained by rotating the analyser $10° - 20°$ (depending on the degree of distortion in the tile at the extremes of angle) and collecting neighbouring spectra.

The data obtained can be analysed in two ways. Surface peaks can be projected onto the angular axis to produce a blocking curve; or a small number of channels from the angular axis can be projected onto the energy axis to produce an energy cut, which is useful for depth profiling, as shown in Figure 3.10. The sharp drop in intensity of backscattered ions at the outer edges of the obtained blocking curve come about due to the distortions mentioned previously and demonstrate the need for a reasonable level of overlap between neighbouring data sets in the angular range.

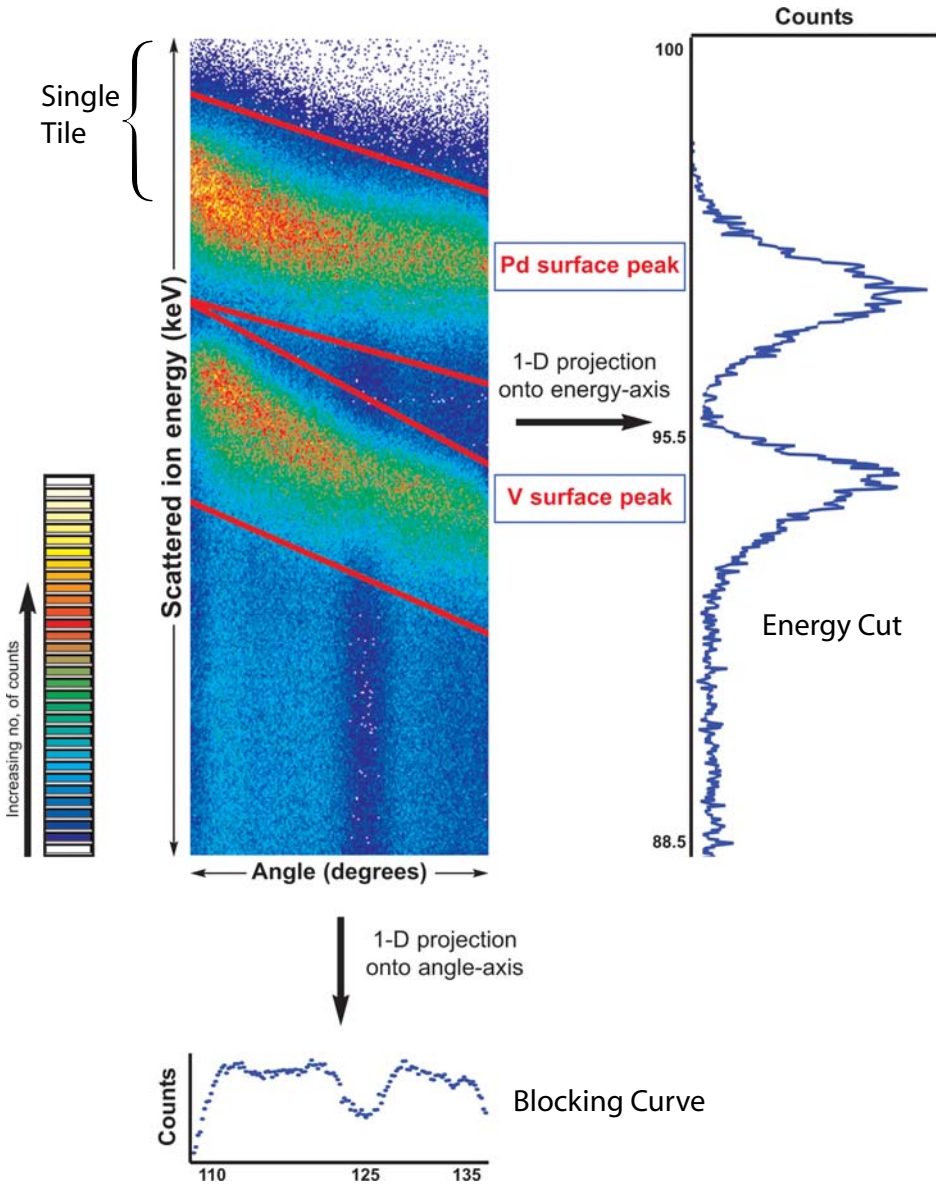

Figure 3.10: 2-D tiled spectrum obtained from five individual tiles. Spectrum is acquired for 100 keV H^+ ions incident along $[\overline{1}10]$ direction of a Pd(111) substrate with a thin $V_2O_3(0001)$ overlayer, scattering detection is centred on the [112] blocking direction. Also shown are an example 1-D projection onto the energy-axis producing an energy cut, and an example 1-D projection onto the angle-axis producing a blocking curve.

3.2.6 Sample Preparation

Metal samples used were cut to a thickness of approximately 2 mm by spark erosion from single crystal bars of diameter $\sim$ 10 mm, the crystallographic orientation of which was determined by Laue X-ray diffraction. The surfaces were then polished mechanically using successively finer grades of diamond paste. At the Daresbury MEIS facility, samples are mounted onto a sample holder, see Figure 3.11, consisting of a grounded molybdenum backplate, and electrically isolated filament for sample heating and a thermocouple connected to the backplate to monitor sample temperature. The sample is held in place on the backplate using tantalum clips. The holder is designed to allow transfer between the different chambers.

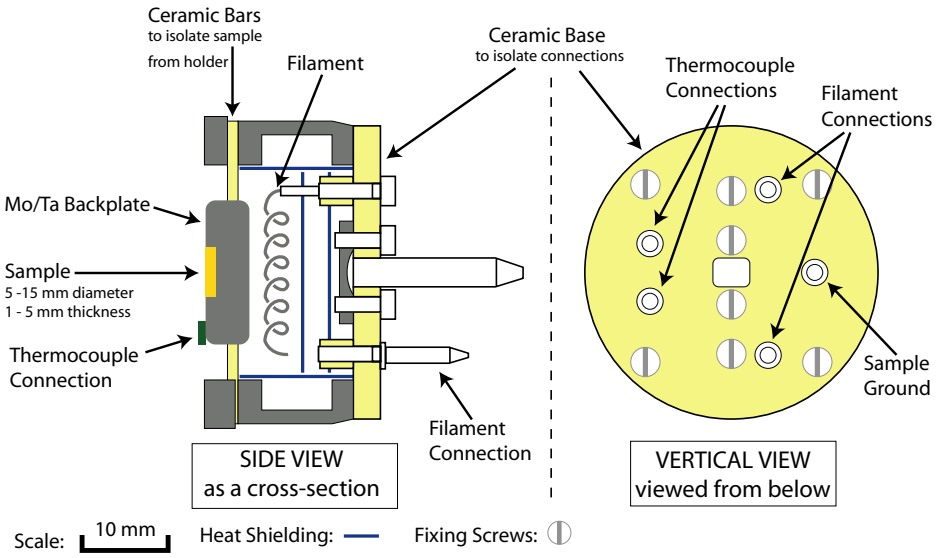

Figure 3.11: Schematic scale diagram of the sample holder used at the UK MEIS facility. The cross-section demonstrates that the sample is mounted on a backplate, which is in isolation to the rest of the sample holder, with the electrically isolated heating filament located beneath. The plan view shows the connections present on the sample holder.

Once in the preparation chamber and under UHV, the sample is cleaned of atmospheric contaminants using cycles of sputtering (ion bombardment) followed by annealing. Typically, each sputtering cycle is conducted using 1.5 keV Ar^+ ions at a pressure of 1×10^{-5} mbar, which gives rise to a sample drain current

of $\sim$ 10 μA, for a time of 20 minutes. The sputtering process removes atoms, including contaminants, from the top layers of the crystal leaving the surface with substantial atomic damage. The order of the surface is restored by annealing the sample to a crystal dependent temperature. The samples used in this thesis all have high melting points, so were typically heated to $\sim 600^{\circ}$C. These high temperatures are not possible using radiative heating from the filament alone, and were instead achieved via electron bombardment (e-beam heating). A potential of up to 1 kV (but typically in the range of $300-500$ V) is applied to the backplate causing the filament to act as an electron source, with the electrons hitting the sample producing effective heating. Annealing often causes bulk impurities to preferentially segregate to the surface, which for the substrates studied in this thesis proved to be particularly problematic for sulphur segregating out of copper, so further sputter/anneal cycles are required to produce a clean surface.

AES was typically used to confirm that there are no chemical contaminants in the surface region, whilst LEED was used to verify that the surface of the sample was well-ordered (when the pattern was a sharp 1×1 pattern at energies of 60 eV, consistent with the surface region). When both of these criteria are satisfied, the sample was judged to be clean.

Chapter 4

$V_2O_3(0001)$ Thin Films Grown on Au(111) and Pd(111)

4.1 Introduction

Transition metal oxides play a fundamental role in practical heterogeneous catalysis. One such transition metal is vanadium, which plays an extensive role due to the large number of different formal valence charges in which it can exist (V^{+x}, where $2 \leq x \leq 5$); this leads to several compounds of vanadium oxides existing, comprising different structures and stoichiometries including VO, VO_2, V_2O_3, V_2O_5 and V_6O_{13}. Perhaps the most commonly used in industry is V_2O_5, however, it is widely believed that the vanadium, in the surface of V_2O_5 based catalysts, takes on lower oxidation states during the catalytic process [47, 48]. Therefore elucidating the surface of V_2O_3 could yield important information about this reaction.

V_2O_3 forms two different phases: an antiferromagnetic monoclinic phase below the phase transition temperature, $150 - 170$ K; or a paramagnetic trigonal corundum phase above the phase transition temperature. It is the (0001) surface of the corundum structure that is investigated for the purpose of this thesis. The most reliable method of producing well-ordered $V_2O_3(0001)$ films for surface studies is by epitaxial growth in situ in the UHV experimental chamber, and it has been

shown that it is possible to grow such films on a range of different substrates, such as: Au(111) [49, 50], $Cu_3Au(100)$ [51], Pd(111) [52, 53, 54], Rh(111) [55, 56] and W(110) [49, 50].

The $V_2O_3(0001)$ crystal formed consists of alternating layers of vanadium and oxygen parallel to the surface, with the oxygen layers consisting of three planar atoms per unit mesh, forming a quasi-hexagonal arrangement. The vanadium layers, which are buckled, comprise two atoms per unit mesh situated in three-fold coordinated sites with respect to the oxygen atom layers. This results in a layer structure of the form $\cdots V'O_3VV'O_3V\cdots$, where VV' represents the two components of vanadium in the buckled layer. There are thus three theoretical bulk terminations for the (0001) surface: $\cdots VV'O_3$ (oxygen termination); $\cdots O_3VV'$ (double-metal termination); or $\cdots V'O_3V$ (half-metal termination), see Figure 4.1. Total-energy calculations show that the most energetically stable of these is the half-metal termination. However, it is widely believed that producing the $V_2O_3(0001)$ films epitaxially in UHV leads to the formation of a vanadyl termination, $\cdots V'O_3V{=}O$, consisting of surface vanadyl species created by oxygen atoms atop the vanadium atoms of the half-metal termination. This termination has been predicted, using DFT [57, 58], to be the most stable under UHV.

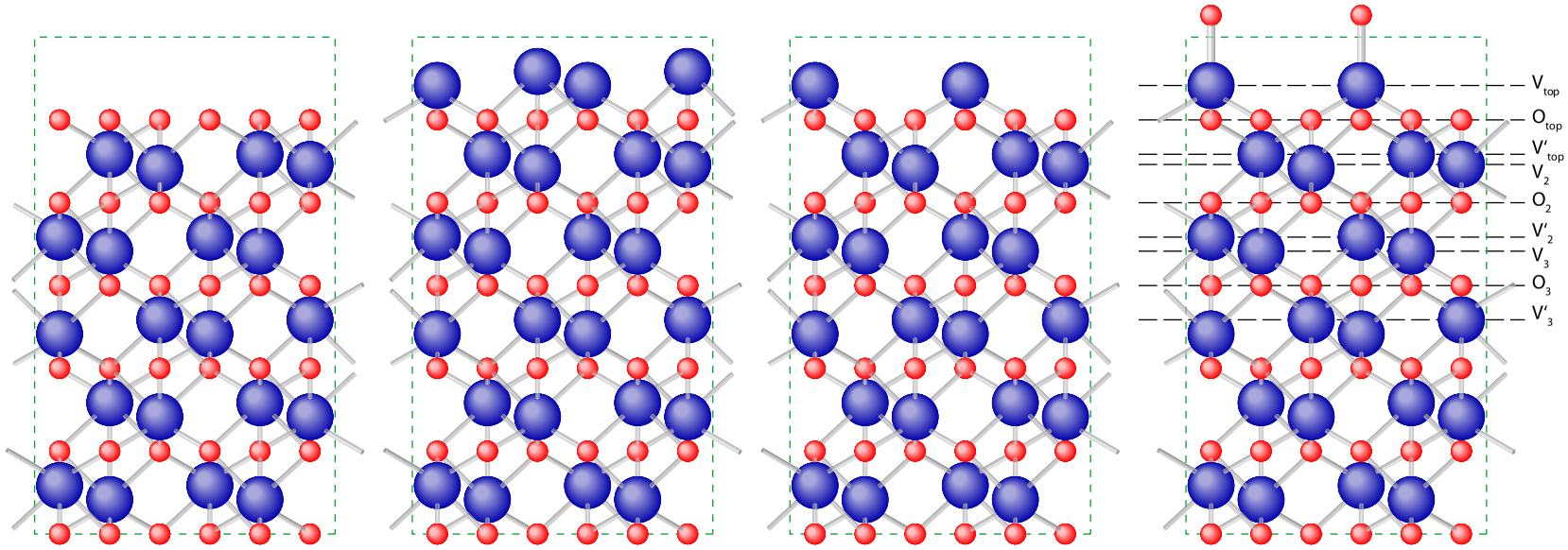

(a) $\cdots$VV'O_3 (oxygen termination).

(b) $\cdots O_3$VV' (double-metal termination).

(c) $\cdots$V'O_3V (half-metal termination).

(d) $\cdots$V'O_3V=O (vanadyl termination).

Figure 4.1: Side view of four possible terminations for the $V_2O_3(0001)$ surface. The large blue atoms represent the vanadium atoms and the smaller red atoms represent the oxygen. The dashed green box represents the size of the unit cell. Three terminations arise from the bulk structure: Figure (a) shows an oxygen termination, Figure (b) shows a double-metal termination and Figure (c) shows a half-metal termination. The energetically stable vanadyl termination predicted by DFT is shown in Figure 4.1(d) along with the notation used to identify each layer of the structures.

4.2 Previous work

Since the early 1990s, considerable interest has been given to modelling the surface of vanadium oxides due to the major role that they play in heterogeneous catalysis. As a result, a large number of surface science studies exist. However, the majority of these previous investigations are either theoretical or qualitative, with just one known previous study attempting to provide quantitative experimental data on the structure of the $V_2O_3(0001)$ surface [59].

Whilst there is little in the way of quantitative structural evidence on the $V_2O_3(0001)$ surface, some studies do exist on the two analogous corundum systems of $\alpha-$alumina (Al_2O_3) and chromia (Cr_2O_3), so it may be possible to glean some information from these on plausible $V_2O_3(0001)$ terminations. $Al_2O_3(0001)$ has been studied using surface X-ray diffraction (SXRD) [60], quantitative LEED [61] and ion scattering [62]; the $Cr_2O_3(0001)$ surface has also been studied using SXRD [63] and quantitative LEED [64]. All of these investigations favoured a half-metal termination with a strong contraction of the outermost layer spacing relative to the ideal bulk structure termination, although the SXRD study of $Cr_2O_3(0001)$ found evidence of significant Cr occupation of interstitial subsurface sites. A vibrational spectroscopy study [65] of epitaxial films grown on Cr(110) has been interpreted as showing the presence of a chromyl (Cr=O) group atop the Cr atoms of the half-metal termination, a termination that has also been shown to exist under oxygen-rich conditions [66]. The chromyl termination is similar to the vanadyl termination, one of the terminations of the $V_2O_3(0001)$ surface that is favoured by total-energy calculations.

Despite the lack of quantitative experimental understanding, information about the $V_2O_3(0001)$ surface structure has been inferred from a wealth of studies using scanning tunnelling microscopy (STM) [55, 51] and DFT [67, 68, 58, 57]. The STM images imply that the as-prepared epitaxially grown films are consistent with an absence of any surface reconstruction, whilst the DFT studies find a large contraction

of the outermost layer of the half-metal termination to be energetically stable with the total-energy calculations for the vanadyl termination proving particularly favourable.

Additional support for the vanadyl termination comes from studies using reflection-absorption infra-red spectroscopy (RAIRS) [49] and electron energy loss spectroscopy (EELS) [49, 69], which identify a vibrational mode in the spectra that is attributed to the V=O stretching frequency. However, a low energy ion scattering spectroscopy (ISS) study of $V_2O_3(0001)$ grown on $Cu_3Au(100)$, coupled with STM [51], identifies the surface as a double-metal termination stabilised by one third of an oxygen layer, with the oxygen atoms located in pseudo-bridge positions; oxygen atoms in an atop site, as would be expected for a vanadyl termination, are specifically excluded.

Another energetically stable model identified using DFT and proposed by Kresse *et al.* [57] is derived from the oxygen termination. A continuation of the bulk corundum $V_2O_3(0001)$ structure terminating with an oxygen layer ($\cdots$VV'O_3VV'O_3) produces a polar surface that would be unstable; instead, the proposed structure is made thermodynamically stable by shifting a vanadium atom from the second vanadium layer into the first, creating a vanadium trilayer, with the layers arranged in the form $\cdots$V'O_3VO_3VV"V'O_3 (known hereafter as the 'Kresse O_3 model'), see Figure 4.21(b). However, this structure is reported to be stable only at 'high' oxygen partial pressures, although the necessary pressures are not stated. Some support for an oxygen termination comes from an STM study by Surnev *et al.* [70], which found two $V_2O_3(0001)$ terminations occurring with almost equal formation energies. One of the terminations was identified as the vanadyl termination, and the other was identified as an oxygen termination with three oxygen atoms per unit cell, as in the bulk.

The study by Kröger *et al.* [59], using scanned-energy mode photoelectron diffraction (PhD), found clear support for a strongly-relaxed half-metal termination

as favoured by theoretical studies and in agreement with the comparable studies of the $Al_2O_3(0001)$ and $Cr_2O_3(0001)$ surfaces. Whilst this best fit structure did not include the predicted vanadyl termination, the R-factor for the model including the surface vanadyl group lies within an acceptable variance of the best fit structure and therefore could not be excluded.

4.3 Experimental Method

4.3.1 Preparation

The single metal crystal substrates were cleaned by cycles of cold sputtering and annealing, see Section 3.2.6, with annealing to temperatures of 600 °C for the Au(111) crystal, and 700 °C for the Pd(111) crystal. After several such cycles, the crystals had no peaks attributable to contamination in the AES spectra, therefore they were judged to be clean and they had sharp well-ordered (1×1) LEED patterns down to 56 eV.

For the thinnest $V_2O_3(0001)$ films (< 20 Å), the corundum $V_2O_3(0001)$ film was grown using a previously established method for growth on Pd(111), see Kröger *et al.* [59] and references therein. This method involved creating the $V_2O_3(0001)$ films via several short doses, where each dose was performed as follows. The metal substrate was held at a temperature of ~ 300 °C throughout the deposition. The chamber was opened to an oxygen atmosphere of 2×10^{-7} mbar. Vanadium was evaporated from a vanadium rod evaporator for a period of 10 minutes, after which the sample was slowly cooled to a temperature of 100 °C. At this stage the oxygen was removed from the system and the sample was flashed to ~ 400 °C for $1-2$ mins to allow the surface to order and to remove any excess, unreacted oxygen from the surface. Typically, three such doses are necessary in order to prepare a film of a reasonable thickness, although data were taken on preparations with a range of one to five doses.

However, the above method was found to lead to island formation of $V_2O_3(0001)$ on the Au(111) substrate. In addition, in order to conduct the structural analysis using MEIS, it was necessary to grow much thicker $V_2O_3(0001)$ films (of the order of 100 Å) to enable alignment to a crystallographic direction within the film, and using the above method would have taken a prohibitively long time. Therefore, a slightly different approach was used, as proposed by Dupuis *et al.* [49]. Thicker films were grown as follows. The metal substrate was held at a temperature of ~ 300 °C throughout the deposition. The chamber was opened to an oxygen atmosphere of 2×10^{-7} mbar. Vanadium was evaporated from a vanadium rod evaporator for the full period of deposition, typically $1-3$ hrs, after which the sample was annealed for $10-20$ mins at 500 °C, to allow the surface to order, whilst exposed to an oxygen partial pressure of 5×10^{-8} mbar.

4.3.2 Characterisation

After deposition, the sample yielded a well ordered $(\sqrt{3}\times\sqrt{3})$ LEED pattern relative to that of the metal substrate at 56 eV, as expected for a (1×1) termination of the $V_2O_3(0001)$ structure, see Figure 4.2. The Auger spectrum showed peaks only attributable to vanadium, oxygen and the relevant substrate (gold or palladium), see Figure 4.3 for an example spectrum obtained from a film grown on a palladium substrate. The shape of the spectrum in the region $450-550$ eV qualitatively agreed with that expected for V_2O_3 [71].

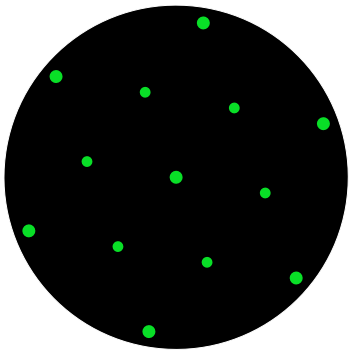

(a) Theoretical $\sqrt{3} \times \sqrt{3}$ LEED pattern relative to that of the metal substrate.

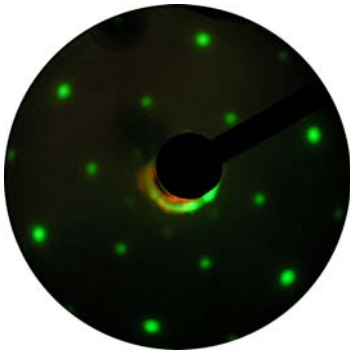

(b) LEED pattern obtained at 56 eV after sample preparation of a $V_2O_3(0001)$ surface, confirming a $\sqrt{3} \times \sqrt{3}$ LEED pattern relative to that of the metal substrate.

Figure 4.2: Figure showing comparison between theoretical LEED pattern and experimentally obtained LEED pattern for the $V_2O_3(0001)$ surface. Figure (a) shows the theoretical pattern, Figure (b) shows the experimentally obtained LEED pattern confirming the presence of a $\sqrt{3} \times \sqrt{3}$ LEED pattern relative to that of the metal substrate.

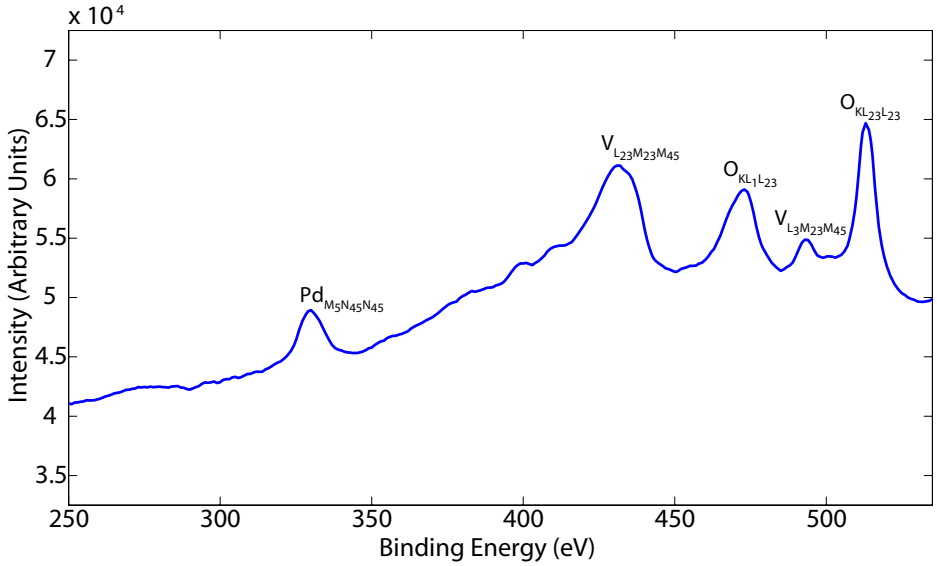

Figure 4.3: An example Auger spectrum obtained from a preparation of $V_2O_3(0001)$ on Pd(111). The spectrum is not differentiated to allow for a qualitative comparison of the expected shape for V_2O_3 [71].

Further confirmation of the correct stoichiometry was obtained from the MEIS data. Figure 4.4 demonstrates the process used to determine the correct stoichiometry of the vanadium oxide films. Figure 4.4(a) shows the raw uncorrected data of an energy spectrum obtained from one preparation of vanadium oxide on palladium. The vanadium and oxygen peaks both sit on a background from the palladium, so the signal from the palladium is removed first. The vanadium background increases with energy loss, so a simple linear background (as shown in Figure 4.4(a)) is also removed from the data. The result of the background removal is given in Figure 4.4(b), along with a simple fit to the data obtained using SIMNRA [72], a software package used to simulate depth profiles for RBS and MEIS data. The oxygen peak is then extracted, and scaled in amplitude by a ratio of the squared atomic numbers, $\frac{23^2}{8^2}$, to correct for the different scattering cross-sections of vanadium and oxygen, and further scaled in amplitude by $\frac{2}{3}$ to account for the necessary ratio of vanadium to oxygen in V_2O_3. The scaled oxygen surface peak is then translated in energy, to account for the difference in energy losses, and is overlaid on the vanadium surface peak giving rise to Figure 4.4(c). This figure clearly shows that the surface peaks are now essentially identical, confirming the stoichiometry of the vanadium oxide films to be V_2O_3, as required.

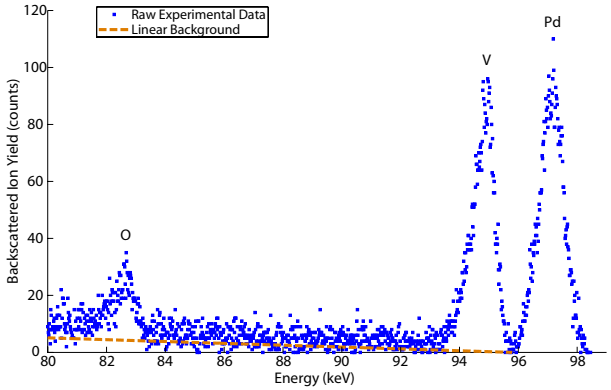

(a) Uncorrected raw data, shown as points, with linear background shown as a dashed line.

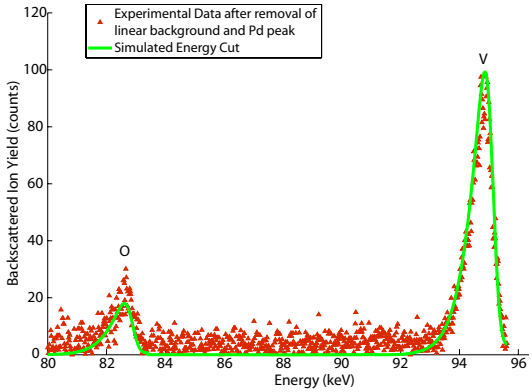

(b) Data with background and palladium peak removed, shown as points. Also shown, as a solid line, is the corresponding SIMNRA simulation.

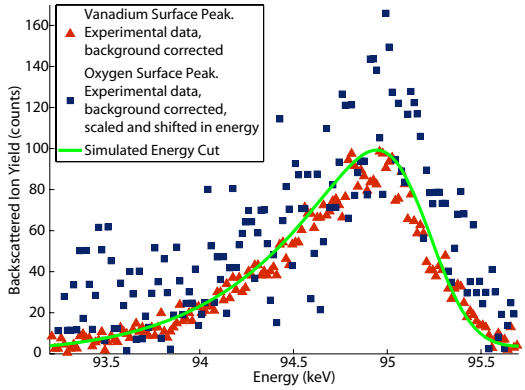

(c) Vanadium surface peak, shown as red triangles, with solid line representing the SIMNRA simulation. The scaled and shifted oxygen surface peak, shown as blue squares, is essentially identical in shape and magnitude to the vanadium surface peak.

Figure 4.4: Figure showing stages used for confirming stoichiometry of the vanadium oxide films, for a film grown on a palladium substrate. Figure (a) shows an energy cut with raw uncorrected data, Figure (b) shows the data corrected for background along with SIMNRA simulation and Figure (c) compares the corrected vanadium surface peak along with a scaled and shifted oxygen peak. The peaks overlap confirming stoichiometry of 2:3.

4.3.3 Measurements

MEIS data were taken using an 100 keV H^+ ion beam with a dose of 4 μC per tile, and with no area of the surface exposed to more than 16 μC, after which signs of radiation damage can be observed (see Section 4.3.4 for more details). Data were obtained on several different preparations of the $V_2O_3(0001)$ surface, for a number of different coverages on each of the two different substrates, palladium and gold.

For preparations $\lesssim$ 25 Å thick, data were taken in incidence geometries aligned along crystallographic directions within the substrate. The directions chosen for this were nominal one layer illuminations for the substrate, $\langle\overline{1}00\rangle$ and $\langle\overline{11}0\rangle$, which should minimise backscattered ion yield from the substrate. The scattering angles for data taken was for 27° (one tile) centred on 125° for both of the geometries as the films were too thin to obtain structural information, and these data were deemed to be sufficient to obtain information on the interface between the film and substrate.

For thicker films, of the order of 100 Å, data were taken in incidence geometries aligned along crystallographic directions of the $V_2O_3(0001)$ film, in order to obtain structural information about the surface. Some data were taken in the $\{2\overline{11}0\}$ azimuth of the $V_2O_3(0001)$ film (parallel to the $\{\overline{11}2\}$ azimuth of the substrate), along the $\langle 10\ \overline{10}\ 03\rangle$ direction, see Figure 4.5. This direction lies very close to the $\langle\overline{1}00\rangle$ incidence direction for the substrate. The majority of data were taken in the $\{10\overline{1}0\}$ azimuth of the $V_2O_3(0001)$ film (parallel to the $\{\overline{11}0\}$ azimuth of the substrate), and along the $\langle 50\overline{5}1\rangle$ direction, see Figure 4.6. For both of these geometries, data were obtained in the largest possible range of scattering angles, to maximise the number of data points for fitting. Two inequivalent domains exist for the $V_2O_3(0001)$ film, by rotation of the crystal through 60° (equivalently 180°) about the surface normal. This is due to a combination of the rumpling of the vanadium layer and the different possibilities for the vanadium layer that terminates the structure. Both domains are shown in Figure 4.6, for the $\{10\overline{1}0\}$ azimuth of the $V_2O_3(0001)$ film. Whilst each domain should theoretically exist with equal

probability, typically small differences in backscattered ion yield were found in the experimental data for the two different domains. Therefore, data were taken in each of these directions to allow for averaging. Simulations were also run on both possible domains and averaged to obtain the simulated blocking curves.

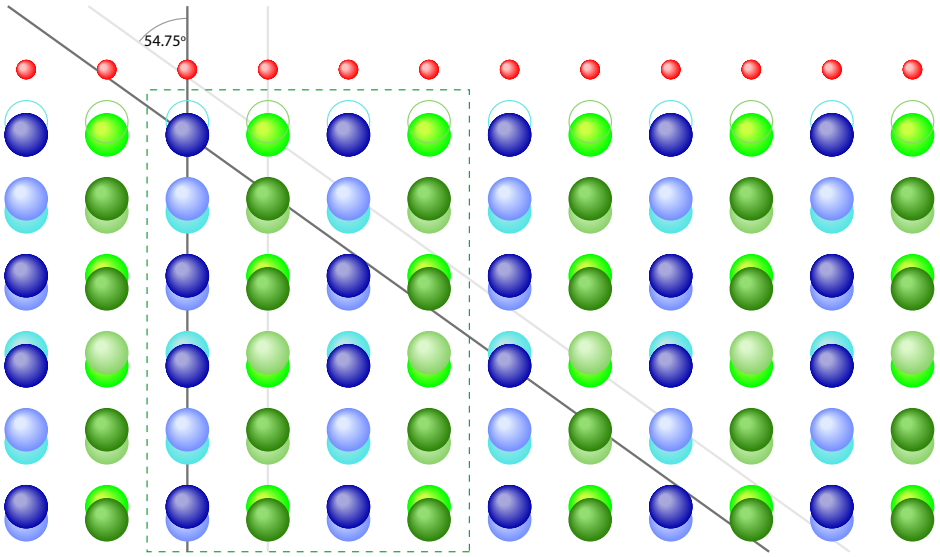

Figure 4.5: Figure showing a side view of the positions of vanadium atoms in the $\{2\overline{1}\overline{1}0\}$ azimuth of the $V_2O_3(0001)$ film with bulk like spacings. Each of the different colours for the larger vanadium atoms lies in a different vertical plane and therefore blocking/shadowing interactions cannot occur between the different colours. The hollow circles mark the position of the double-metal layer, which is excluded from the majority of the simulations. The smaller red atoms show the position of the proposed vanadyl oxygen. The green dashed box marks the unit cell for the $V_2O_3(0001)$ corundum structure. Also included is the incidence direction used.

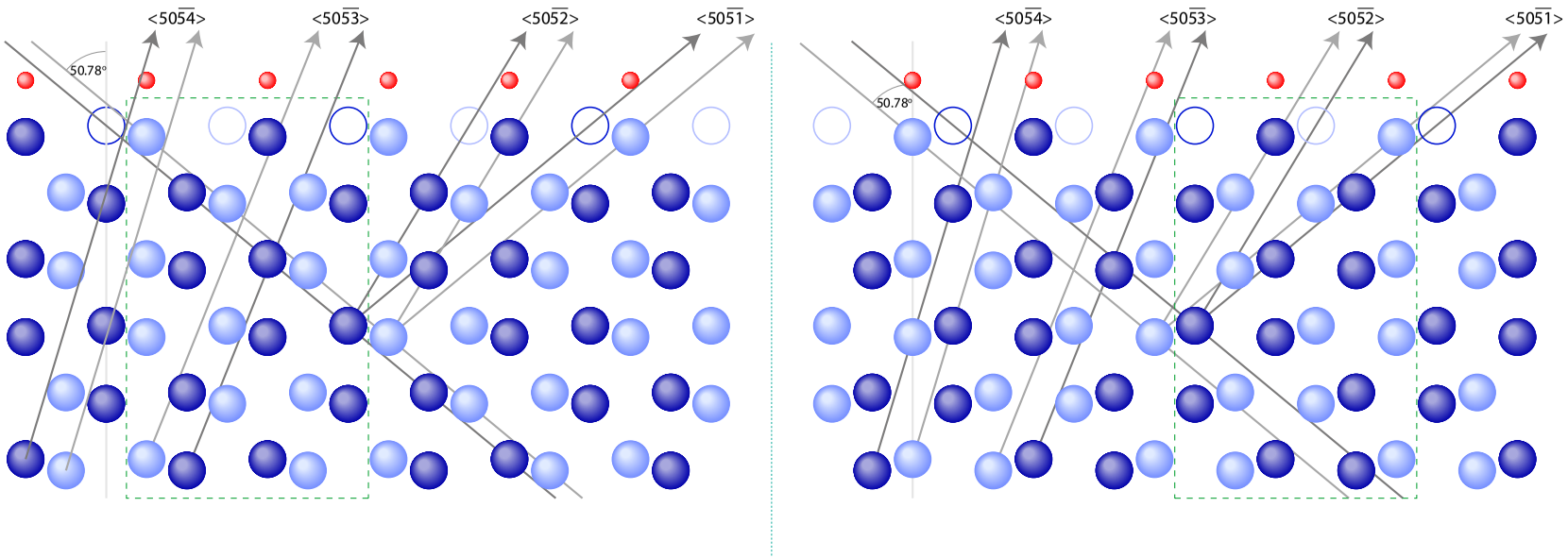

Figure 4.6: Figure showing a side view of the positions of vanadium atoms in the two inequivalent domains, one each side of the central dotted line, of the $\{10\bar{1}0\}$ azimuth of the $V_2O_3(0001)$ film with bulk like spacings. The light blue atoms lie in a different vertical plane to the dark blue atoms and therefore blocking/shadowing interactions cannot occur between the two different shades. The hollow circles mark the position of the double-metal layer, which is excluded from the majority of the simulations. The smaller red atoms show the position of the proposed vanadyl oxygen. The green dashed box marks the unit cell for the $V_2O_3(0001)$ corundum structure. Also included is the incidence direction used and the major blocking directions.

4.3.4 Beam Damage Survey

Beam-induced damage to sample surfaces results from the transfer of momentum, from incident ions to atoms in the sample, during the back-scattering process. The potential for damage is always a concern in MEIS, therefore incident ion doses are normally kept as low as possible to minimise any risk and so for the majority of crystal surfaces, MEIS is deemed to be non-destructive. This is justified because the back-scattered ion contains information about the surface before the collision, when the surface was in an undamaged state, and the probability of a second ion backscattering from a damaged region is very small with the low ion doses used. However, in the case of a compound surface the collision cascade of the recoiling target atom can induce atomic mixing; and there is the potential for additional damage through electronic excitations, which are unlikely to result in damage in metal surfaces. The combination of these factors results in a larger region, compared to that in a metal single crystal, of damage centred on the scattering event. This is likely to be exacerbated by the relatively low atomic numbers of both vanadium and oxygen, which will result in a large recoil energy via equation 2.1. Two previous MEIS studies of oxide materials [73, 74], have indeed both found that beam-induced damage of the surface occurs at a high rate compared to metal surfaces. Therefore it was necessary to investigate the rate of any beam-induced damage to the V_2O_3 to determine if this surface could be studied using MEIS and, if so, the maximum reasonable exposure possible for experimentation.

Experiments to investigate the scale of beam-induced damage for 100 keV H^+ incident ions were conducted by recording the vanadium surface peak for successive incident ion doses on the same position of the crystal surface. Because the $V_2O_3(0001)$ was grown onto metal substrates with significantly higher atomic numbers than the oxide overlayer, the vanadium surface peak sits on a background from the substrate. Therefore it was necessary to align the ion beam to the most surface specific geometry within the substrate, namely a double-alignment geometry, to minimise the backscattered ion yield obtained from the substrate and

hence allow for an intensity of ions backscattered from the vanadium, large enough above the background to observe any signs of damage occurring. The geometry chosen was $\langle\bar{1}00\rangle$ incidence, $\langle 111\rangle$ detection with respect to the substrate, because these directions also lie on, or close to, major crystallographic directions within the $V_2O_3(0001)$, providing good surface sensitivity within the film.

Figure 4.7 shows the scattered ion energy spectra corresponding to scattering from the vanadium atoms. Whilst it is expected that the oxygen atoms would suffer more severely from beam-induced damage, due to the much smaller scattering cross-section, the signal-to-noise ratio for the oxygen surface peak is too poor to obtain similar spectra for the oxygen atoms. The data were recorded in increments of 1 μC for low cumulative doses, up to increments of 4 μC for higher cumulative doses. For clarity, these were combined to 16 μC increments for the figure, although one spectrum for 8 μC, doubled so that it appears on the same scale, is also included.

The figure demonstrates that up to 16 μC, the spectra remain essentially identical; but at 32 μC, changes begin to appear in the spectra, which increase with each subsequent dose. The oxide study by Parkinson *et al.* [74] demonstrated that when beam-induced damage occurs in TiO_2 the visible effect is a broadening of the low energy shoulder of the surface peak, which results from an increase in ions scattered from the subsurface, indicative of atomic displacements. However, this is not the case for the vanadium peak in Figure 4.7, which instead shows an increase in backscattered ion yield across the entire surface peak with each increase of dose, due to a rise in the gold background on which the vanadium peak sits. This enhancement of the background is indicative of an increase in the ions scattered from the gold substrate, suggesting that beam-induced damage is occurring within the gold. Visual inspection of the gold crystal after data were taken agrees with the proposal that the gold has suffered from beam-induced damage, see Figure 4.8.

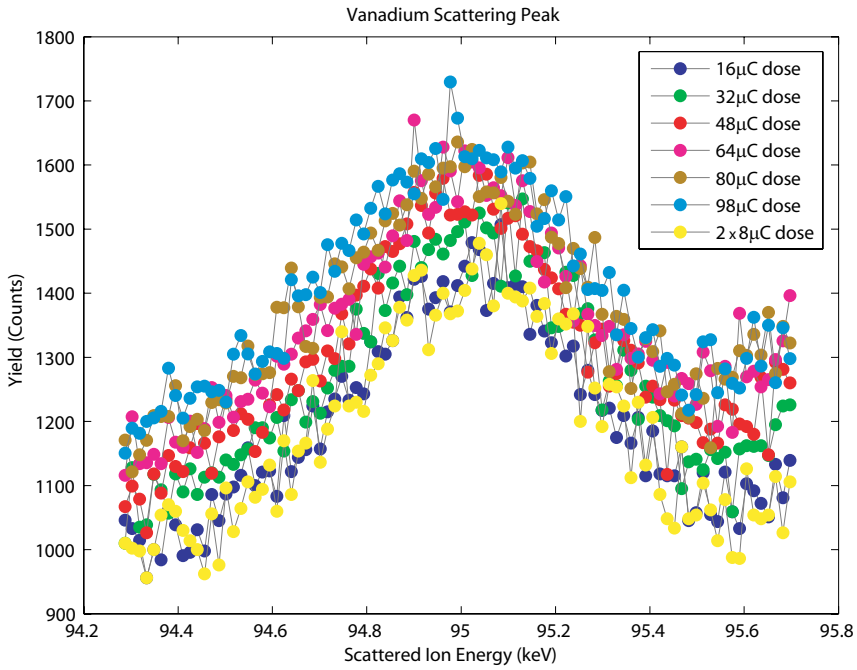

Figure 4.7: Beam-induced damage survey. The energy spectra are obtained by scattering from vanadium atoms for a $V_2O_3(0001)$ film grown on Au(111), for successive ion beam doses on one crystal spot. The peak remains constant up to 16 μC after which point the background on which the peak sits rises with increasing dose.

Figure 4.8: Photograph of the Au(111) sample showing visible signs of damage after MEIS data acquisition for the beam-induced damage survey.

In order to gauge the rate of beam-induced damage, each peak was integrated and scaled to account for different measured doses. This backscattered ion yield (in counts per μC) is plotted against the cumulative dose, to show how the yield varies with the total dose received on the sample. The result of this plot can be seen in Figure 4.9. This plot confirms that the backscattered ion yield remains approximately constant up to a dose of 16 μC, at which point the yield begins to rise steadily with increasing dose.

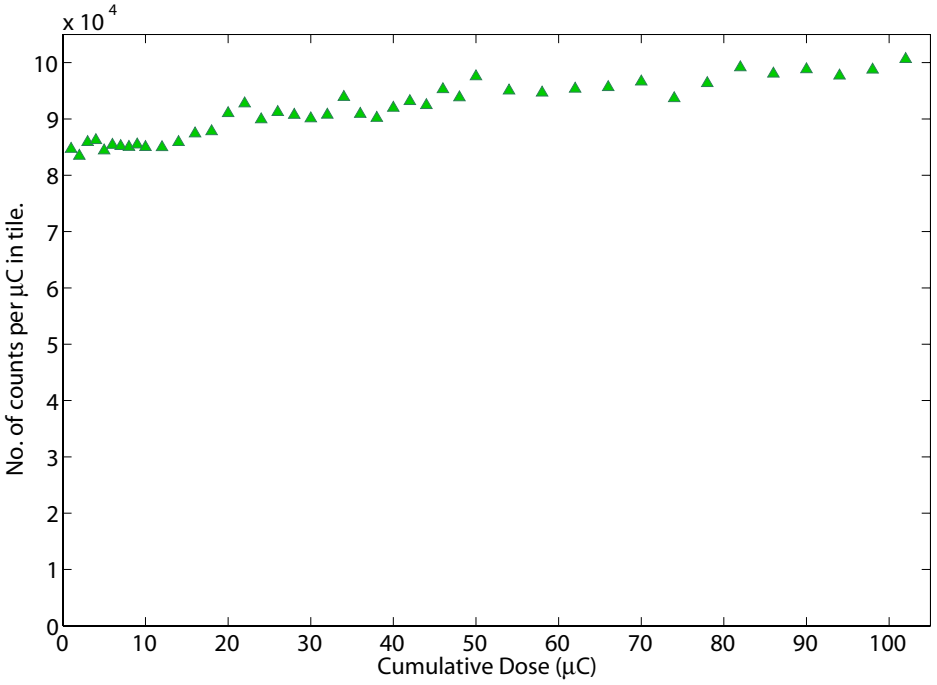

Figure 4.9: The plot of backscattered ion yield against cumulative dose demonstrates how the yield varies with the total dose received on the V_2O_3(0001) sample. The data remains roughly constant up to 16 μC, after which the yield rises steadily with increasing dose.

Based on this evaluation, the total dose taken at any one position on the crystal was kept below 16 μC, with this condition achieved by regularly changing the position of the ion beam spot on the surface by moving the sample in a direction perpendicular to the beam. This maximum dose was chosen because the data showed no detectable sign of any form of damage occurring, and whilst there is no indication of damage to the V_2O_3 itself at any dose, any damage to the gold substrate should also be

avoided. This could lead to a decrease in the quality of $V_2O_3(0001)$ films grown on that surface during further new preparations onto the clean, damaged gold surface.

A similar study on the $V_2O_3(0001)$ films grown on the palladium substrate yielded no obvious change in the scattered ion energy spectra, with increasing dose, up to a total dose of > 100 μC. This suggests that no significant damage occurs within either the palladium substrate or the $V_2O_3(0001)$ overlayer. However, the total dose taken at any one position on the palladium crystal was still kept below 16 μC to ensure data were obtained within 'safe' limits.

4.4 Results and Discussion

4.4.1 Interface Information

Unlike the majority of other surface science techniques, MEIS is not intrinsically surface specific and is therefore capable of yielding information about the interface between the $V_2O_3(0001)$ films and the substrate crystal. A qualitative study was carried out in order to inspect the quality of the interfaces between the $V_2O_3(0001)$ films and the two different substrates for films prepared under a range of conditions. The quality of the interface can potentially impact upon the crystallinity of the overlayer film, which in turn can affect the usefulness of any such film in industrial applications.

In order to evaluate the interfaces, simple simulations of the energy cuts for the different preparations were performed. The simulation software, written by P. D. Quinn [75] and based upon a number of previous studies [15, 22, 23], creates a theoretical energy cut from a model of the crystal. The software is able to model different parameters for the ion beam and is able to fit these parameters, as well as the composition and hitting probabilities for atoms in the crystal, to the experimental data.

4.4.1.1 V_2O_3(0001) films grown on Pd(111)

Figure 4.10 shows the results of some of the simulations performed for the Pd(111) substrate. Figures 4.10(a) and 4.10(b) are both recorded from relatively thin V_2O_3(0001) films, the first of which is composed of two 'doses' (as defined in Section 4.3.1) and the second is composed of five 'doses'. Figure 4.10(c) is a much thicker film prepared using the second method in Section 4.3.1, the broad palladium peak now lies between the vanadium and oxygen peaks.

For the first two doses, all peaks are relatively symmetric and narrow, indicative of the thin films with minimal thickness distribution. As more doses of the V_2O_3(0001) film are applied to the substrate, the vanadium and oxygen peaks develop a broadening of the low energy, back, edge of the peak, and the palladium peak develops a corresponding broadening to the high energy, front, edge. This suggests that the V_2O_3(0001) films are growing with an increasing range of thicknesses, with each successive dose of the overlayer. For the very thick film, the vanadium peak is generally narrow and symmetric suggesting a good degree of crystallinity in the film, the only diversion from this is a slight broadening of the back edge of the peak indicative of a slightly rough film, with a small thickness distribution. The presence of a rough film appears likely due to the very broad palladium peak, however, some peak broadening is expected due to an increase in straggling because the palladium is buried beneath a thick overlayer. Therefore these observations were used to build initial crystal models on which to perform and optimise energy cut simulations.

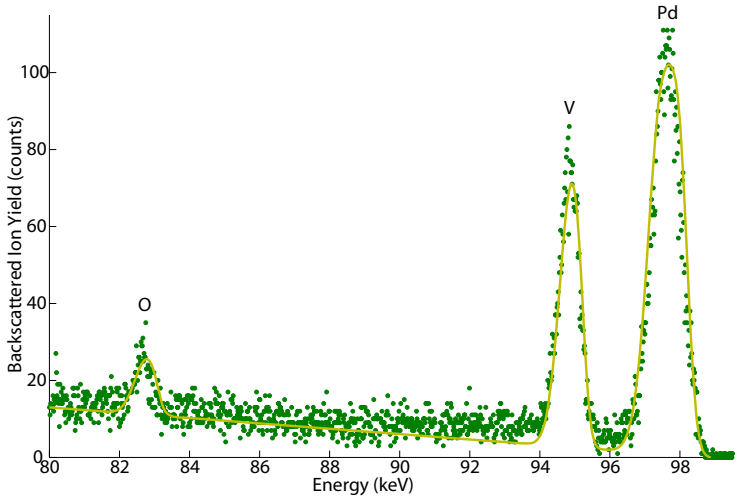

(a) Two doses of $V_2O_3(0001)$ on Pd(111).

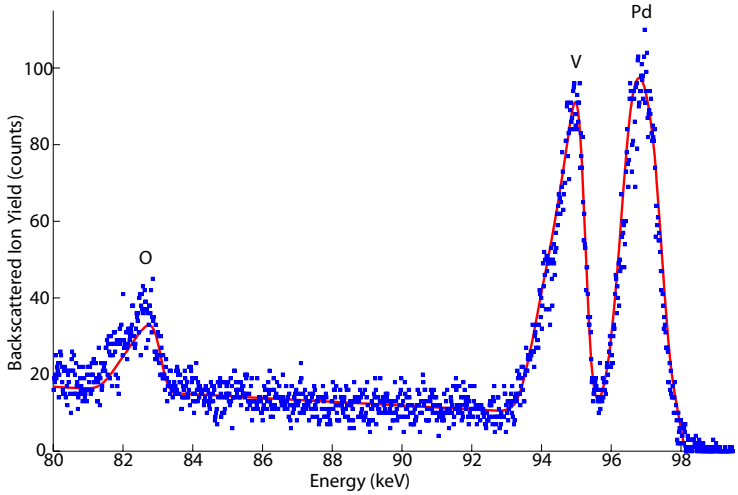

(b) Five doses of $V_2O_3(0001)$ on Pd(111).

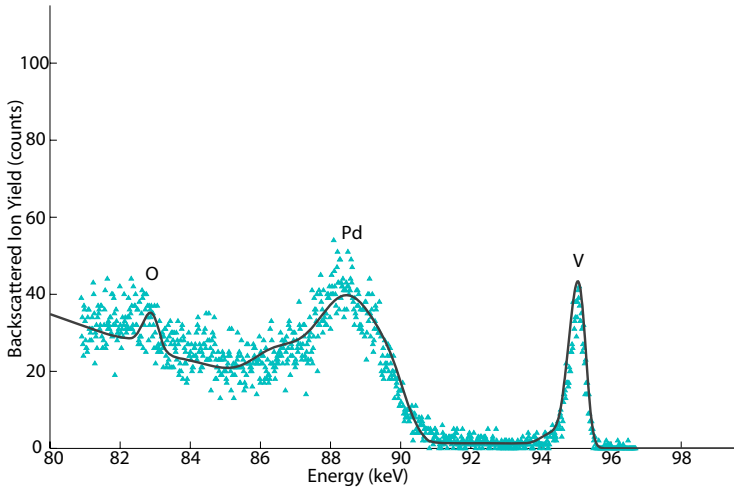

(c) 2 hr deposition of $V_2O_3(0001)$ on Pd(111), followed by a 20 min anneal at 500 °C.

Figure 4.10: Plots showing simulation (solid line) and experimental data (data points) for energy cuts obtained from three different preparations of $V_2O_3(0001)$ on Pd(111). Each energy cut is the projection of 3 channels from the $[\overline{1}10]$ incidence direction and $[21\overline{1}]$ outgoing direction with respect to the Pd(111) substrate.

Inelastic energy losses on the ions due to electronic stopping as they travel through the $V_2O_3(0001)$ film cause an increasing shift of the palladium peak to lower energy with increasing film thickness. This shift can be used to obtain an average film thickness using a value for the stopping power of the ions through $V_2O_3(0001)$, which can be obtained using SRIM [19]. The various determined thicknesses are given in Table 4.1, alongside the distribution of film thicknesses determined from the energy cut simulations. The ion beam used in MEIS has a relatively large area and therefore the data obtained are an average over a large section of the prepared film, this averaging explains why thicknesses smaller than interlayer distances are possible.

Film Preparation	Average overall thickness of $V_2O_3(0001)$ layer, determined by energy shift of substrate peak, (Å)	Variation in thickness of V_2O_3 layer, determined by energy cut simulation, (Å)
1 dose (Figure not shown)	1.3	1
2 doses (Figure 4.10(a))	5.4	3
3 doses (Figure not shown)	7.7	4
4 doses (Figure not shown)	11.4	7
5 doses (Figure 4.10(b))	20.1	11
2 hr deposition followed by 20 min anneal (Figure 4.10(c))	192.4	38

Table 4.1: Summary of the thicknesses of the $V_2O_3(0001)$ films grown on the Pd(111) substrate, determined through the energy shift of the palladium peak, and the corresponding thickness distributions for a range of different film preparations.

For the thinner films, the $V_2O_3(0001)$ overlayer is very rough, with a large range of thicknesses present forming $50-75\%$ of the total $V_2O_3(0001)$ thickness. For the thicker film the thickness distribution is proportionally reduced, making up $\sim 20\%$

of the total $V_2O_3(0001)$ film thickness. The thicker film, as predicted, also showed a large degree of crystallinity, as the simulation required hitting probabilities for the pure $V_2O_3(0001)$ layer similar to those expected for an ideal crystal (1 for the surface atoms, rapidly decreasing to 0 over the next few layers of subsurface atoms). The thinner films required larger hitting probabilities (remaining above 0 for a large number of layers of subsurface atoms) indicative of a poor quality crystal.

4.4.1.2 $V_2O_3(0001)$ films grown on Au(111)

Figures 4.11 and 4.12 show the results of some of the energy cut simulations performed for the Au(111) substrate. Figure 4.11 gives results obtained by deposition of a number of short doses with one 'dose' as defined in Section 4.3.1. Figure 4.11(a) consists of one dose, whilst Figure 4.11(b) consists of two doses. Figure 4.12 shows the results from thicker films prepared using the second method detailed in Section 4.3.1. Figure 4.12(a) was prepared with a 40 min deposition and shows the energy spectra before and after a 20 min post deposition anneal at 500 °C, and Figure 4.12(b) was prepared with a 3 hour deposition followed by a 20 min anneal at 500 °C.

For the films prepared using the initial method of applying several short doses of vanadium, Figure 4.11, the $V_2O_3(0001)$ films appeared to be forming islands with bare regions of gold present in between. This is evidenced in the gold peak, which appears to be a sum of a narrow peak at $\sim$ 100 keV, which is an identical energy to that expected for clean gold, and a broader peak at lower energy ($\sim$ 99 keV in Figure 4.11(a), and $\sim$ 98 keV in Figure 4.11(b)) as expected for a buried gold layer. The contribution from the uncovered gold surface decreases with increasing number of doses of $V_2O_3(0001)$ suggesting that the islands are covering a larger proportion of the surface, however data obtained from samples using this deposition method always produced similar effects.

For the thicker films, Figure 4.12, the gold peak consists only of a single peak at energies below 100 keV as predicted for a buried layer demonstrating that the metal surface is completely covered with $V_2O_3(0001)$. For the 40 min deposition, Figure 4.12(a), the vanadium peak at $\sim$ 95 keV is broad before the anneal suggesting a disordered overlayer, with this peak becoming significantly narrower after the anneal indicating the development of a high degree of crystallinity as expected following an anneal. The gold peak, at $\sim$ 97 keV, has a slight broadening of the high energy edge suggesting the existence of a small distribution of thicknesses of the $V_2O_3(0001)$ film. The 3 hr deposition, Figure 4.12(b), yields a narrow vanadium peak at $\sim$ 95 keV with very low background behind the peak indicative of a high degree of crystallinity. Again these observations were used to develop initial models for performing and optimising energy cut simulations. The oxygen peak, at $\sim$ 83 keV, was included in the simulations, however, it was not included in the optimisation because it is not clearly distinguishable from the background.

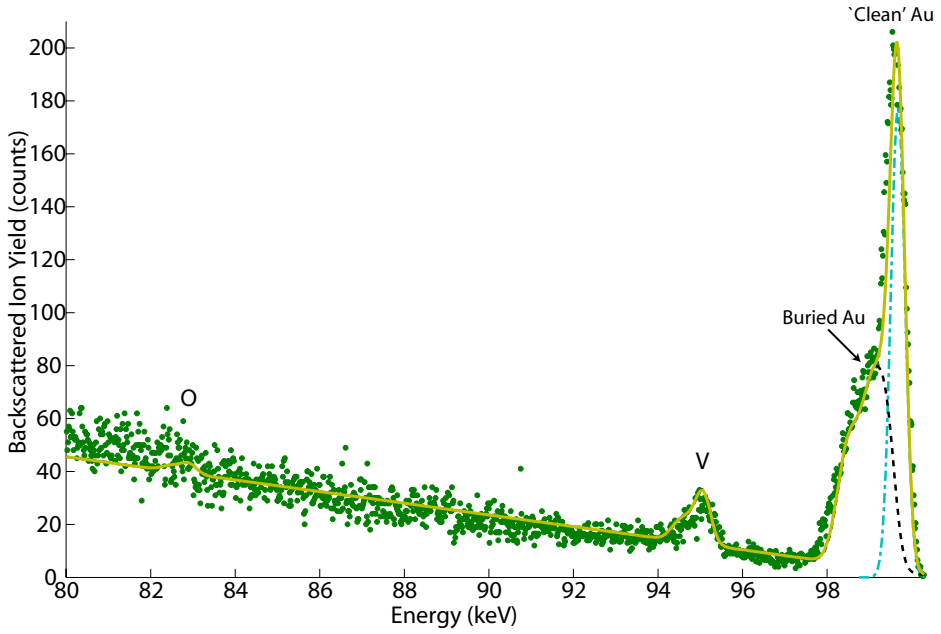

(a) One dose of $V_2O_3(0001)$ on Au(111).

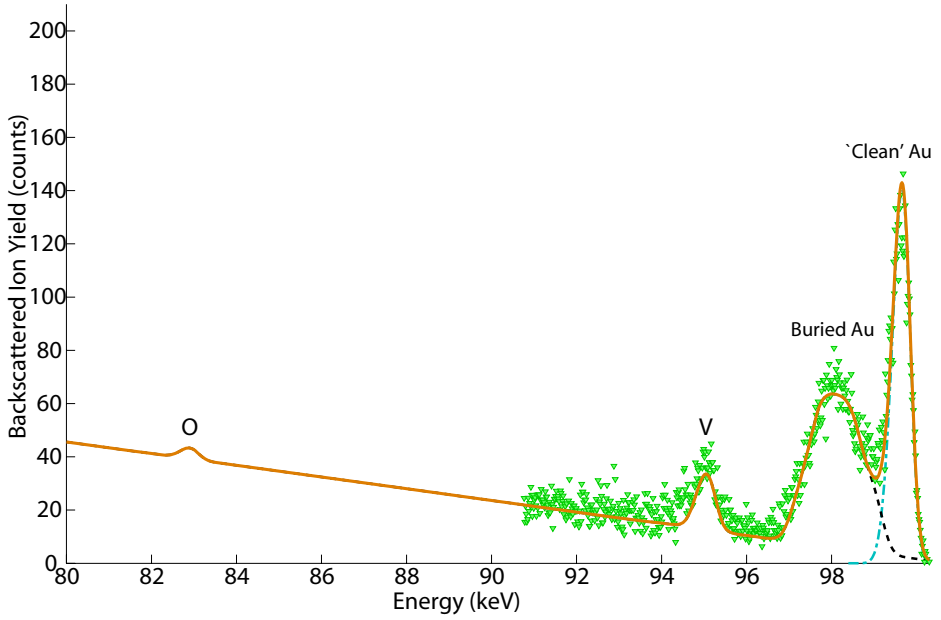

(b) Two doses of $V_2O_3(0001)$ on Au(111).

Figure 4.11: Plots showing simulation (solid line) and experimental data (data points) for energy cuts obtained from preparations of two different thicknesses of $V_2O_3(0001)$ on Au(111). Each energy cut is the projection of 3 channels from the [100] incidence direction and [111] outgoing direction with respect to the Au(111) substrate. The dashed line shows the contribution from the buried gold, the dot-dash line shows the contribution from the uncovered gold.

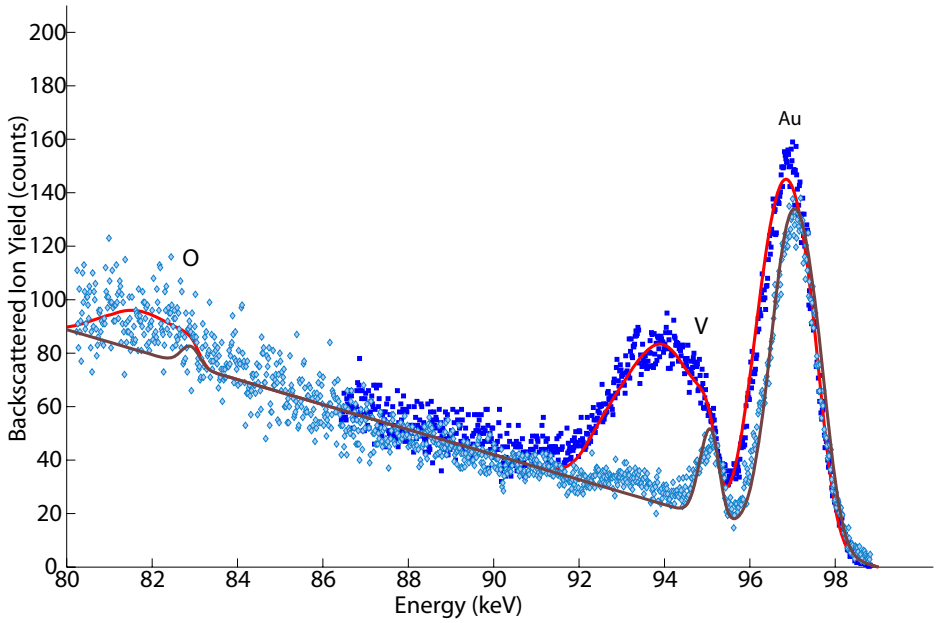

(a) 40 min deposition of $V_2O_3(0001)$ on Au(111), before 20 min anneal at 500 °C (dark blue squares for experimental data and red line for simulation) and after 20 min anneal at 500 °C (light blue diamonds for experimental data and dark brown line for simulation).

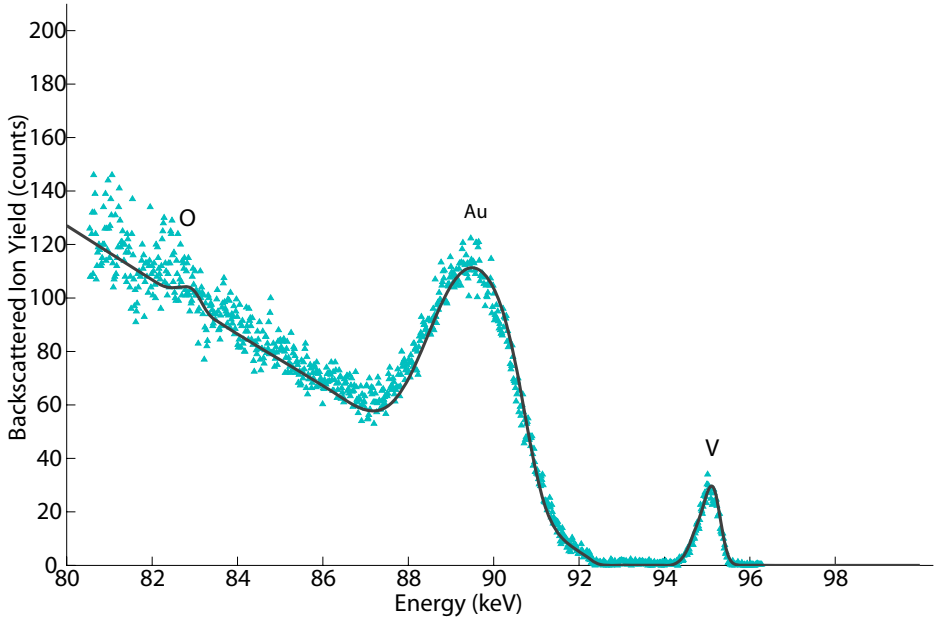

(b) 3 hr deposition of $V_2O_3(0001)$ on Au(111), followed by 20 min anneal at 500 °C.

Figure 4.12: Plots showing simulation (solid line) and experimental data (data points) for energy cuts obtained from preparations of two different thicknesses of $V_2O_3(0001)$ on Au(111). Each energy cut is the projection of 3 channels from the [100] incidence direction and [111] outgoing direction with respect to the Au(111) substrate.

The various thicknesses for the films, as determined using the energy shift of the gold peak, are given in Table 4.2, alongside the thickness distribution for each.

Film Preparation	Average overall thickness of $V_2O_3(0001)$ layer, determined by energy shift of substrate peak (Å)	Variation in thickness of V_2O_3 layer, determined by energy cut simulation (Å)
1 dose (Figure 4.11(a))	5.70	2
2 doses (Figure 4.11(b))	18.16	7
40 min deposition followed by 20 min anneal (Figure 4.12(a))	49.40	16
3 hr deposition followed by 20 min anneal (Figure 4.12(b))	202.04	16

Table 4.2: Summary of the thicknesses of the $V_2O_3(0001)$ films grown on the Au(111) substrate, determined through the energy shift of the gold peak, and the corresponding thickness distributions for a range of different film preparations.

For the thinner films, the $V_2O_3(0001)$ overlayer is slightly rough, with a thickness distribution of $\sim 30 - 40\%$ of the total $V_2O_3(0001)$ thickness. For the thickest film the thickness distribution is proportionally reduced, making up $\sim 8\%$ of the total $V_2O_3(0001)$ film thickness. The thicker film, as predicted, showed a large degree of crystallinity, as the simulation required hitting probabilities for the pure $V_2O_3(0001)$ layer similar to those expected for a perfect crystal. The films prepared using short doses required the predicted combination of a clean Au(111) simulation and a simulation of a $V_2O_3(0001)$ film grown on Au(111), confirming the presence of islands of $V_2O_3(0001)$ with bare gold patches forming using this deposition method.

4.4.2 Surface Structure Analysis

For the purposes of the surface structure analysis, the data acquired from thick $V_2O_3(0001)$ films grown on the Au(111) substrate were used. This was because, based on the depth profiling analysis, these were the best quality films. The films grown on Au(111) were found to produce more uniform films than those grown on Pd(111) and had a higher degree of crystallinity, which should produce better quality blocking curves on which to conduct the structural analysis.

4.4.2.1 Evaluation of Existing Models

Initial investigations concentrated on performing VEGAS simulations for a variety of structural models from the literature, in order to assess the quality of fit between these models and the experimentally obtained MEIS data. The interlayer spacings for these models are defined in Table 4.3, and the MEIS R-factors calculated for each of the simulations for these structures are shown. The model structures were built to a depth of 1 unit cell ($\approx$ 11 Å), this was found to be sufficiently deep to produce complete blocking curves; with any additional layers below this merely increasing computational time and making no change to the simulated data. Any layers below those with parameters listed in Table 4.3 were set to 'bulk' interlayer spacings. VEGAS simulations were initally run with the vibrational amplitudes of the atoms in the bulk of the crystal fixed at mean-square values of 0.070 Å^2 for the vanadium atoms and 0.066 Å^2 for the oxygen atoms, as determined in the study by Kröger *et al.* [59].

Whilst the oxygen atoms were included in all simulations it is important to note that, with the exception of the vanadyl oxygen atom, the oxygen atoms lie entirely within a different vertical plane to the vanadium atoms for the chosen geometries. Because of this, the bulk oxygen atoms have no effect on the blocking curves obtained and therefore no information on their true position could be extracted. Hence, this MEIS study is only able to identify interlayer spacings between vanadium layers, with the position of the oxygen layers relative to the vanadium layers assumed based upon

previous studies. Figures 4.13 − 4.17 show the plots obtained from these existing structures and their associated layer spacings for both azimuths.

	$\cdots$V'O_3V half-metal					$\cdots$V'O_3V=O vanadyl					$\cdots O_3$VV' double-metal
Parameter	Bulk [59]	Czekaj [67]	Czekaj vanadyl minus=O	Kresse [76]	Kröger [59]	Bulk half-metal+=O	Czekaj half-metal+=O	Czekaj [67]	Kresse [76]	Kröger [59]	Bulk [59]
$\langle 50\overline{5}1\rangle$ R-factor	0.060	0.19	0.069	0.31	0.13	0.090	0.16	0.056	0.033	0.066	0.063
$\langle 10\ \overline{10}\ 03\rangle$ R-factor	0.95	0.32	0.46	0.40	0.36	1.1	0.44	0.58	0.95	0.58	0.61
Total R-factor	0.56	0.26	0.29	0.36	0.26	0.64	0.32	0.35	0.54	0.35	0.37
$V_{top}-V'$ (Å)	–	–	–	–	–	–	–	–	–	–	0.36
$V_{top}=O$ (Å)	–	–	–	–	–	1.61	1.61	1.59	1.61	1.55	–
$O_{top}-V_{top}$ (Å)	0.98	0.68	0.82	0.35	0.68	0.98	0.68	0.82	0.75	0.69	0.98
$V'_{top}-O_{top}$ (Å)	0.98	0.98	0.93	1.12	0.93	0.98	0.97	0.93	0.99	1.05	0.98
$V_2-V'_{top}$ (Å)	0.36	0.27	0.34	0.22	0.35	0.36	0.27	0.34	0.28	0.34	0.36
O_2-V_2 (Å)	0.98	0.96	0.96	1.13	1.02	0.98	0.96	0.96	1.08	0.95	0.98
V'_2-O_2 (Å)	0.98	0.98	0.98	1.01	0.98	0.98	0.98	0.98	0.99	0.98	0.98
$V_3-V'_2$ (Å)	0.36	0.36	0.36	0.38	0.36	0.36	0.36	0.36	0.41	0.36	0.36
O_3-V_3 (Å)	0.98	0.98	0.98	1.01	0.98	0.98	0.98	0.98	1.00	0.98	0.98
V'_3-O_3 (Å)	0.98	0.98	0.98	0.98	0.98	0.98	0.98	0.98	0.98	0.98	0.98

Table 4.3: Summary of structural models and corresponding MEIS R-factors obtained from comparison between these simulations and the experimentally obtained blocking curves for the two geometries investigated.

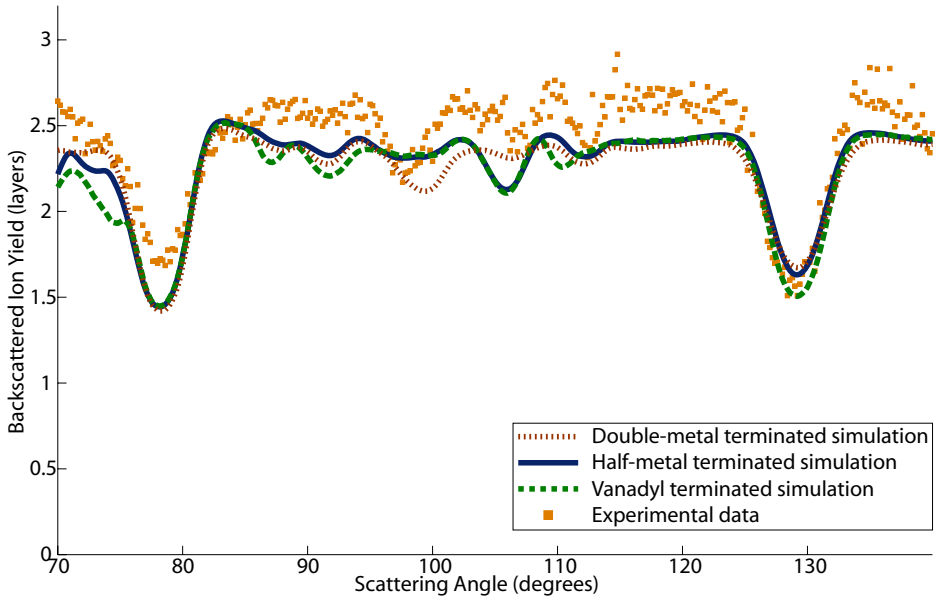

(a) $\langle 50\bar{5}1 \rangle$ incidence direction.

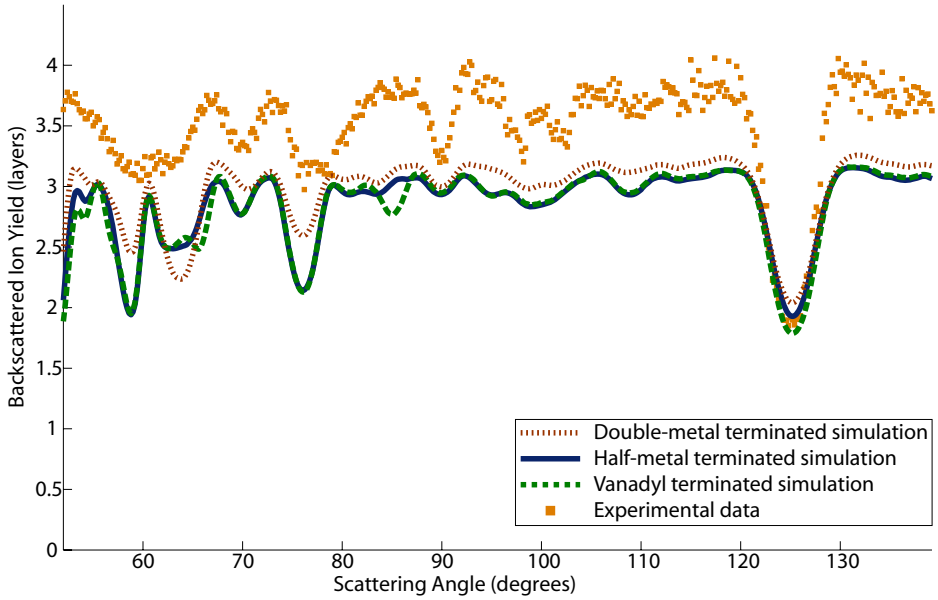

(b) $\langle 10\ \overline{10}\ 03 \rangle$ incidence direction.

Figure 4.13: VEGAS simulations for the bulk-like structure with the dotted red line representing the double-metal termination, the dashed green line representing the vanadyl termination and the solid blue line representing the half-metal termination. All are plotted against the experimental data, shown as orange squares.

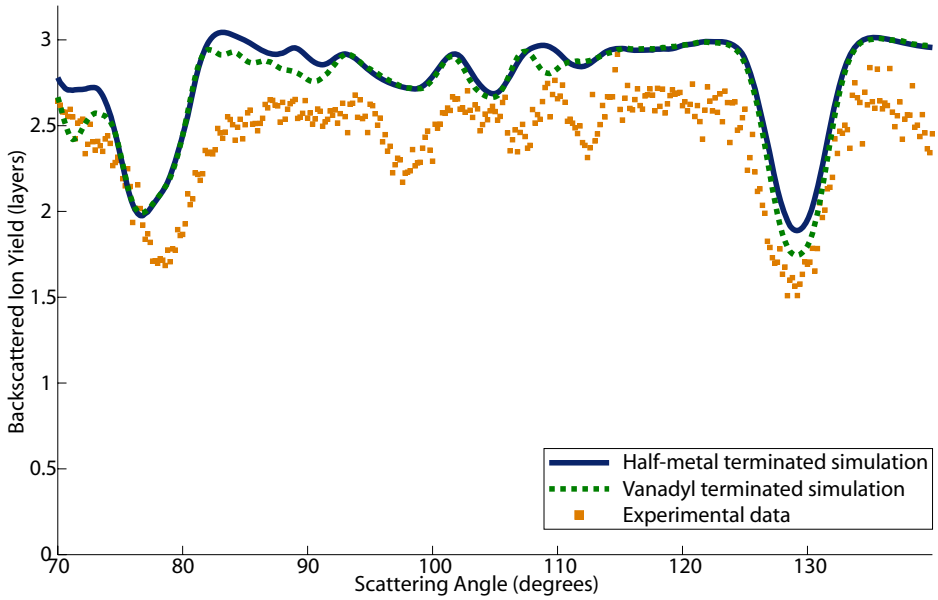

(a) $\langle 50\overline{5}1 \rangle$ incidence direction.

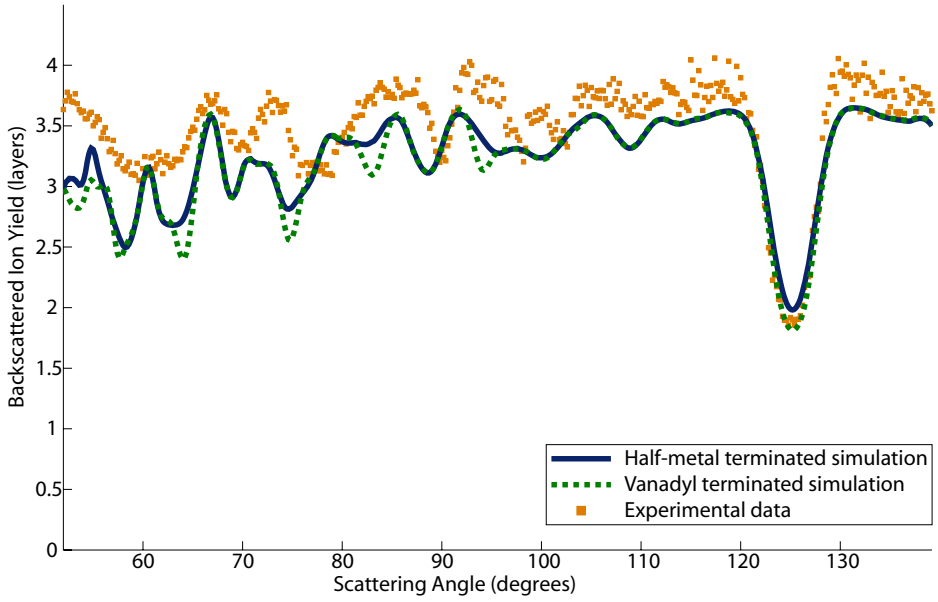

(b) $\langle 10\ \overline{10}\ 03 \rangle$ incidence direction.

Figure 4.14: VEGAS simulations for the Czekaj half-metal structure with the dashed green line representing the vanadyl termination and the solid blue line representing the half-metal termination. They are plotted against the experimental data, shown as orange squares.

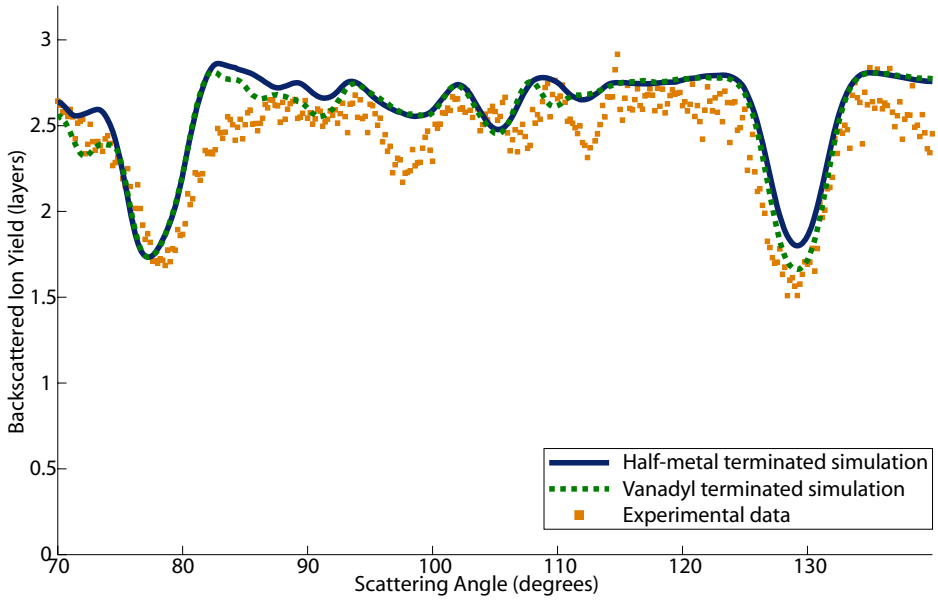

(a) $\langle 50\overline{5}1 \rangle$ incidence direction.

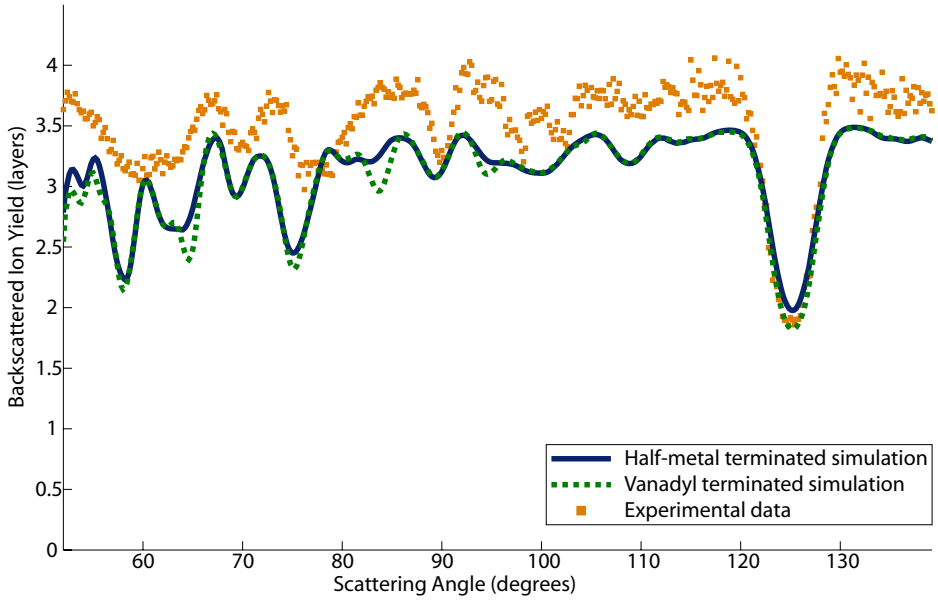

(b) $\langle 10\ \overline{10}\ 03 \rangle$ incidence direction.

Figure 4.15: VEGAS simulations for the Czekaj vanadyl structure with the dashed green line representing the vanadyl termination and the solid blue line representing the half-metal termination. They are plotted against the experimental data, shown as orange squares.

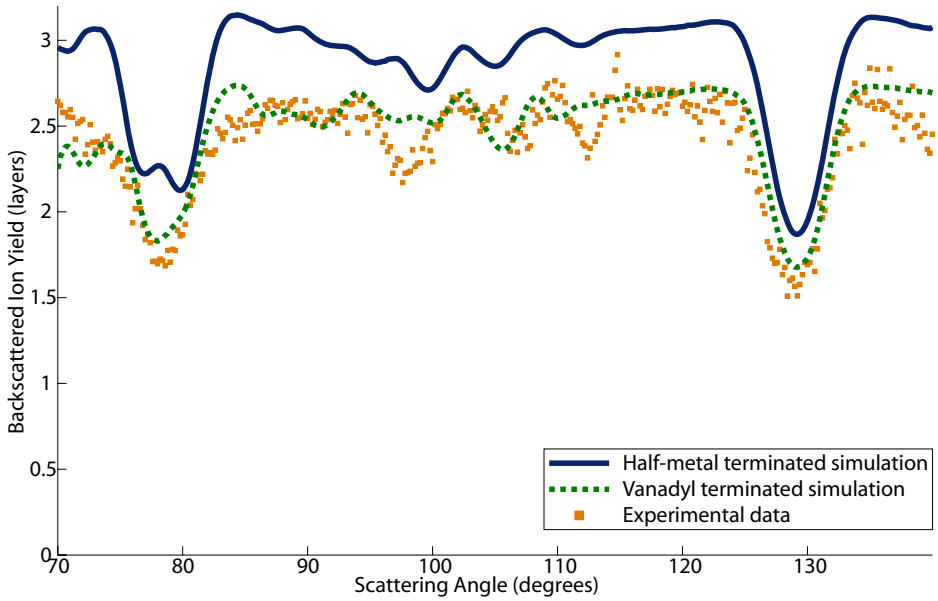

(a) $\langle 50\bar{5}1 \rangle$ incidence direction.

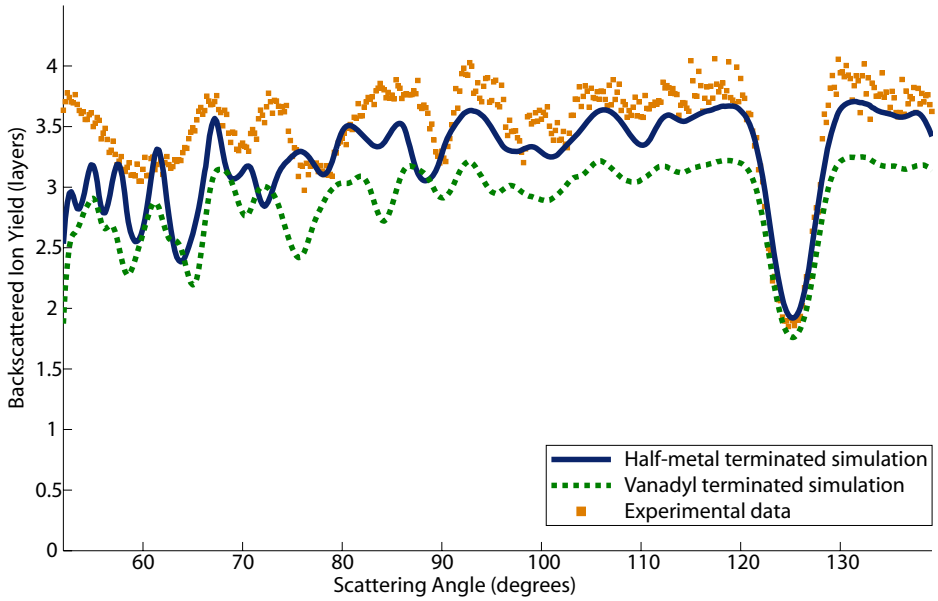

(b) $\langle 10\ \overline{10}\ 03 \rangle$ incidence direction.

Figure 4.16: VEGAS simulations for the Kresse structure with the dashed green line representing the vanadyl termination and the solid blue line representing the half-metal termination. They are plotted against the experimental data, shown as orange squares.

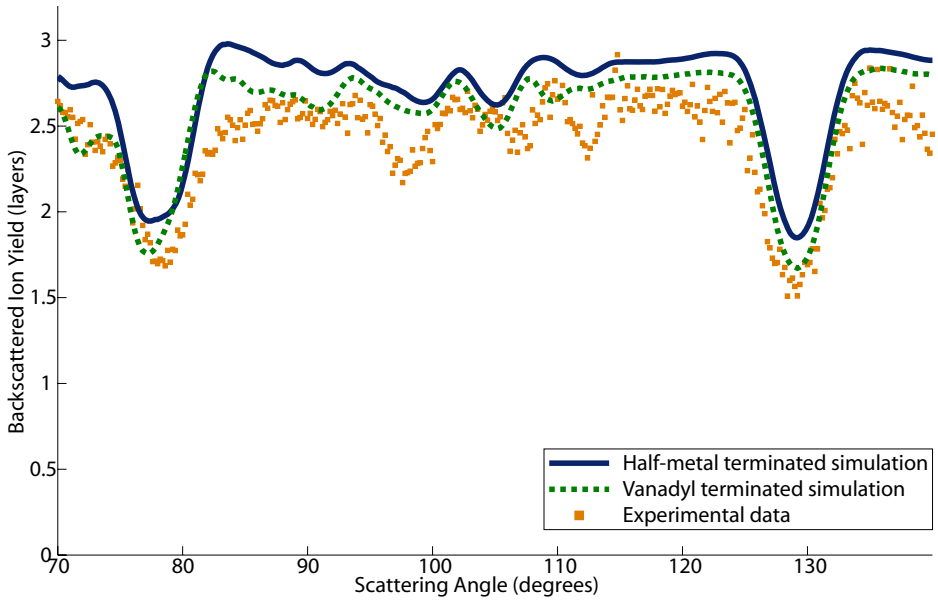

(a) $\langle 50\bar{5}1 \rangle$ incidence direction.

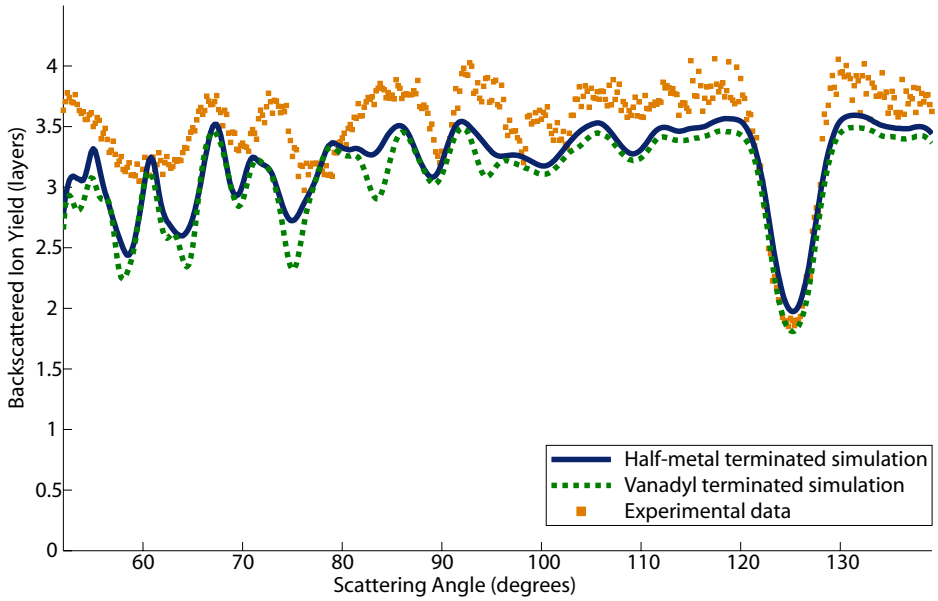

(b) $\langle 10\ \overline{10}\ 03 \rangle$ incidence direction.

Figure 4.17: VEGAS simulations for the Kröger structure with the dashed green line representing the vanadyl termination and the solid blue line representing the half-metal termination. They are plotted against the experimental data, shown as orange squares.

Generally these structures provide a reasonable fit, in terms of R-factor, for the $\langle 50\bar{5}1\rangle$ incidence direction. However, despite the low R-factors, the blocking dips in the central region ($95° - 115°$ scattering angle) of the experimental blocking curve are poorly reproduced in the simulations, as demonstrated in Figure 4.18, which shows a magnification of this area for one of the structures.

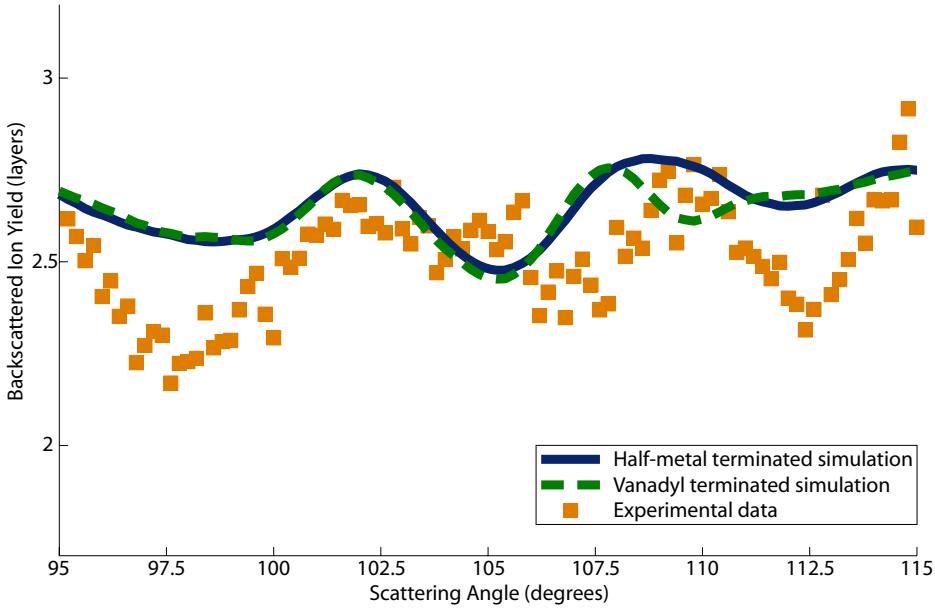

Figure 4.18: Magnification of the central region ($95° - 115°$ scattering angle) of the experimental blocking curve showing the poor fit in this region between the experimental data, shown as orange squares, and the VEGAS simulations. The simulation shown is that of the Czekaj vanadyl structure, with the dashed green line representing the vanadyl termination and the solid blue line representing the half-metal termination.

The R-factor remains small because the data at low scattering angle contribute proportionally more to the R-factor than data at higher scattering angle and the fit at the low scattering angle, $\langle 50\overline{51}\rangle$ blocking dip at $\sim 75°$, is generally good. The weighting towards fitting at low scattering angle is because the χ^2 R-factor is calculated from the data with the Rutherford scattering cross-section re-applied, which results in a higher yield of backscattered ions at low scattering angle in comparison to higher angles.

For the Czekaj structures (Figures 4.14(a) and 4.15(a)) and Kröger structures (Figure 4.17(a)), the $\sim 98^\circ$ blocking dip, arising from blocking along the $\langle 50\overline{5}\overline{2}\rangle$ direction (see Figure 4.6), is located at the same angle as the dip in the experimental data. However the magnitude of this dip is greatly reduced in comparison to the experimental data. A large contribution to this dip arises from blocking by the V' layer, and because the uppermost V' layer is not present in either the half-metal or vanadyl terminations the dip is small in comparison to the double-metal termination where this layer does exist.

The $\langle 50\overline{5}3\rangle$ and $\langle 50\overline{5}4\rangle$ blocking dips, located at $\sim 107^\circ$ and $\sim 112^\circ$ respectively in the experimental data, are strongly shifted to lower angle in all of the simulations, other than those with bulk interlayer spacings. This shift corresponds to the large inward relaxation of the outermost vanadium atom, which is predicted by the DFT studies. This feature does not appear to be reproduced in the experimental data. The exceptionally large contraction of this layer in the Kresse half-metal termination (Figure 4.16(a)) yields a double dip at 78°, a large angular shift in the 98° dip and also an enhancement in the overall backscattered ion yield due to greater subsurface illumination. These factors give this structure the largest R-factor for this azimuth out of the structures examined.

The blocking curve from the $\langle 10\ \overline{10}\ 03\rangle$ incidence direction is rather more complex and contains many blocking features, see Figures 4.13(b), 4.14(b), 4.15(b), 4.16(b), 4.17(b). Whilst the overall shape of the experimental blocking curve is produced in the simulations, none of the structural models tested replicate the individual dip positions well, especially those dips below 90° scattering angle, leading to rather high R-factors ($R \gg 0.32$) for this geometry. Another common feature for the simulations in this geometry is that the overall yield is rather lower than that of the experimentally obtained data. When the experimental blocking curves are produced from the raw data, the yield is converted from raw counts to layers via a calibration factor derived from data obtained from a calibration sample (see Section 5.4.2.1 for

more details), the typical error in the yield using this method is ±5%. Additionally, the yield could be increased by enhancing the vibrational amplitudes of the atoms in the structure. However, even taking into account the possible ±5% from the calibration factor, the yield needs to be increased by 15% in order to achieve the right magnitude for the backscattered ion yield, which would require an unphysically high vibrational amplitude. In addition, increasing the vibrational amplitudes would also affect the yield of the blocking curve obtained from the $\langle 50\bar{5}1 \rangle$ incidence direction, leading to a worsening of this fit. Therefore increasing the vibrational amplitude does not lead to an improvement in the overall quality of the fit.

For each of the different existing structures, it can be seen that the half-metal termination yields a marginally better fit between simulation and data than the vanadyl termination. However, the differences in the blocking data are subtle and the R-factors lie within an acceptable variance of the half-metal termination so that the vanadyl termination cannot be excluded.

The position of all of the blocking dips in the simulations with bulk interlayer spacings most closely resemble those obtained in the two sets of experimental data.

4.4.2.2 Analysis of the Possible Role of Imperfections in the V_2O_3(0001) Thin Films

Of the existing structures tested, one of the best fits, in terms of blocking dip position, between simulation and experimental data is given by a bulk like double-metal termination, see Figure 4.13. This structure has been shown in DFT studies to be energetically unstable, so is unlikely to be the true structure. However, the implication that bulk structural parameters dominate the blocking features suggests that there could be greater then expected bulk illumination in the experimental data.

If the V_2O_3(0001) films were not perfectly formed, there could be some orientational mismatch between different areas of the film. The effect of this would be that perfect

alignment along a crystallographic direction would not be possible when averaging over the area of the ion beam spot. This 'misalignment' would allow the ion beam to penetrate deeper into the bulk and so contributions to the blocking curve from subsurface layers would increase. These contributions could include blocking by subsurface double-metal layers, which might explain why the experimental blocking curve appears to show dips from this structure.

The effect of imperfect alignment along a crystallographic direction was then examined in two different orientations. Firstly, by varying the incidence angle of the ion beam in the VEGAS simulation, which equates to sections of films that do not lie perfectly flat with respect to each other along the plane parallel to the surface of the substrate crystal. Secondly, the rotation of the crystal about the normal to the crystal surface was varied. The best fits of simulation to experimental data were found when the crystal was $\sim 1^\circ$ out of alignment in either of the two directions.

Figure 4.19 shows the blocking curves obtained with the incidence direction 1° off the expected value. Simulations were run for vanadyl and half-metal terminations with bulk like parameters, and also for bulk like parameters but with the outer vanadium layer (V_{top}) contracted by $\sim 30\%$, in line with DFT predictions [67] and favoured by other experiments [59], to 0.68 Å. These simulations yield a significant improvement to the fit of the $\langle 10\ \overline{1}0\ 03\rangle$ blocking curve when compared to the previous structures tested. However, the simulations with bulk parameters still provide a marginally better fit than the structures with a contracted outer vanadium layer, although this structure lies within an acceptable variance. Table 4.4 shows the R-factors obtained for these structures.

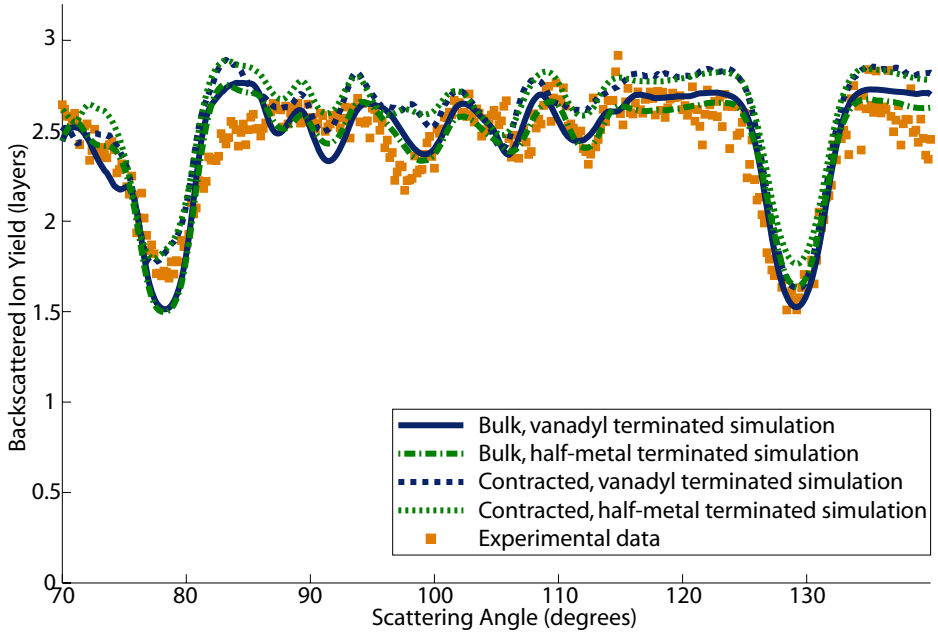

(a) $\langle 50\overline{5}1\rangle$ incidence direction.

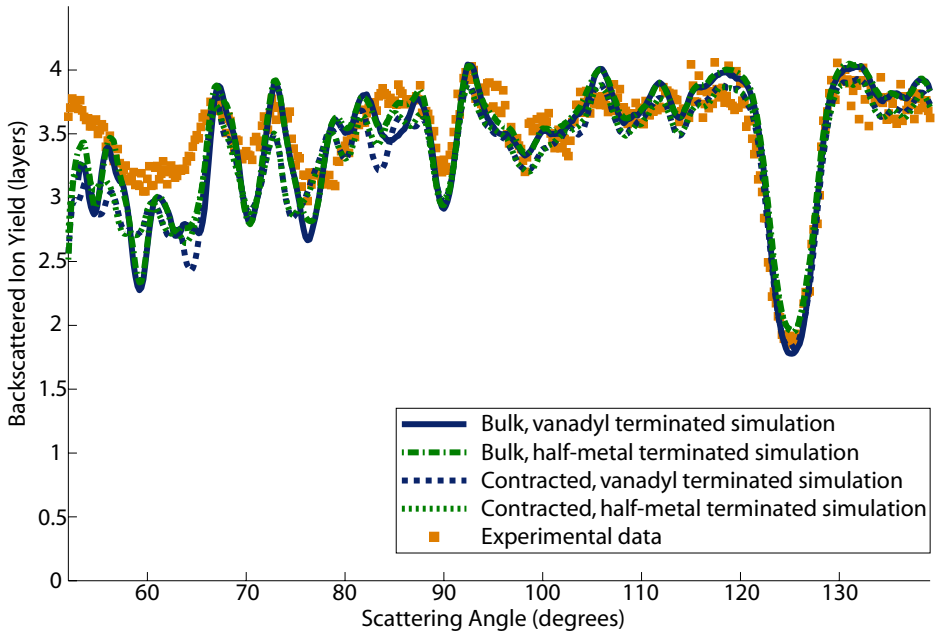

(b) $\langle 10\ \overline{10}\ 03\rangle$ incidence direction.

Figure 4.19: VEGAS simulations for the structures with incidence direction 1° off from the expected value. The bulk vanadyl is represented by a solid blue line, the bulk half-metal is represented by a dot-dashed green line. The contracted vanadyl is represented by a dashed blue line and the contracted half-metal is represented by a dotted green line. They are all plotted against the experimental data, shown as orange squares.

Parameter	bulk like half-metal termination	bulk like vanadyl termination	contracted outer layer half-metal termination	contracted outer layer vanadyl termination
$\langle 50\overline{5}1\rangle$ R-factor	0.030	0.035	0.068	0.056
$\langle 10\ \overline{10}\ 03\rangle$ R-factor	0.32	0.23	0.33	0.24
Total R-factor	0.19	0.14	0.22	0.16

Table 4.4: Summary of the MEIS R-factors obtained for VEGAS simulations of the structures examined with the incidence direction 1° off from the expected value.

Figure 4.20 shows the blocking curves obtained with the rotation about the normal to the crystal surface 0.9° from the predicted crystallographic direction. Simulations were again run for vanadyl and half-metal terminations with bulk like parameters, and also for bulk like parameters but with the outer vanadium layer (V_{top}) contracted to 0.68 Å, in line with DFT predictions [67]. These simulations also yield a significant improvement to the fit of the $\langle 10\ \overline{10}\ 03\rangle$ blocking curve, in comparison with the previous structures tested. The relative shape of the $\langle 50\overline{5}1\rangle$ blocking curve is also improved, however the yield for this simulation is larger than given by the experimental data, and the 98° dip is still shallow compared to the experimental data. These simulations are generally an improvement upon those with the incidence angle out of alignment. Table 4.5 gives the R-factors obtained for these structures.

Parameter	bulk like half-metal termination	bulk like vanadyl termination	contracted outer layer half-metal termination	contracted outer layer vanadyl termination
$\langle 50\overline{5}1\rangle$ R-factor	0.030	0.030	0.29	0.27
$\langle 10\ \overline{10}\ 03\rangle$ R-factor	0.16	0.17	0.11	0.10
Total R-factor	0.10	0.11	0.19	0.18

Table 4.5: Summary of the MEIS R-factors obtained for VEGAS simulations of the structures examined with the rotation about the normal to the crystal surface 0.9° from the predicted crystallographic direction.

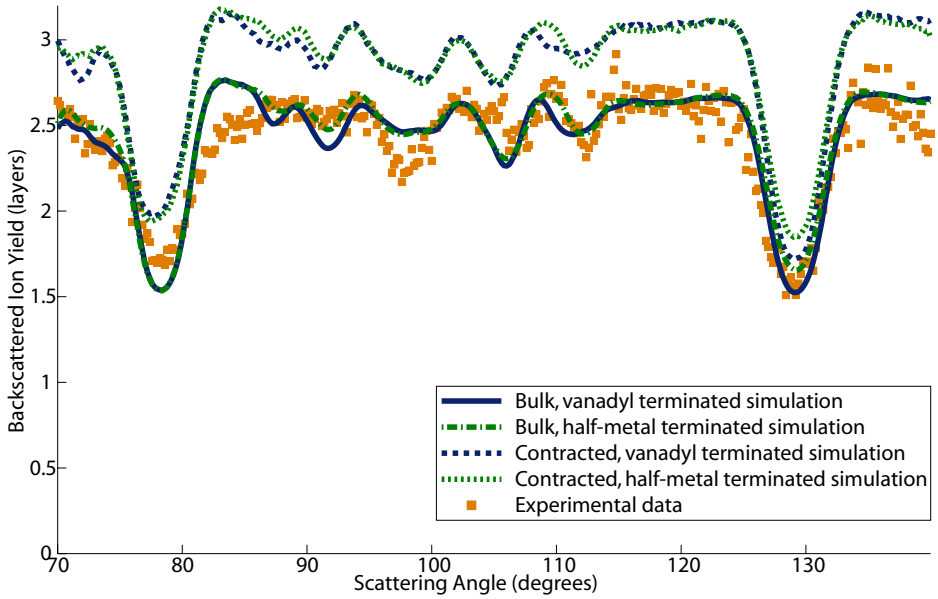

(a) $\langle 50\bar{5}1 \rangle$ incidence direction.

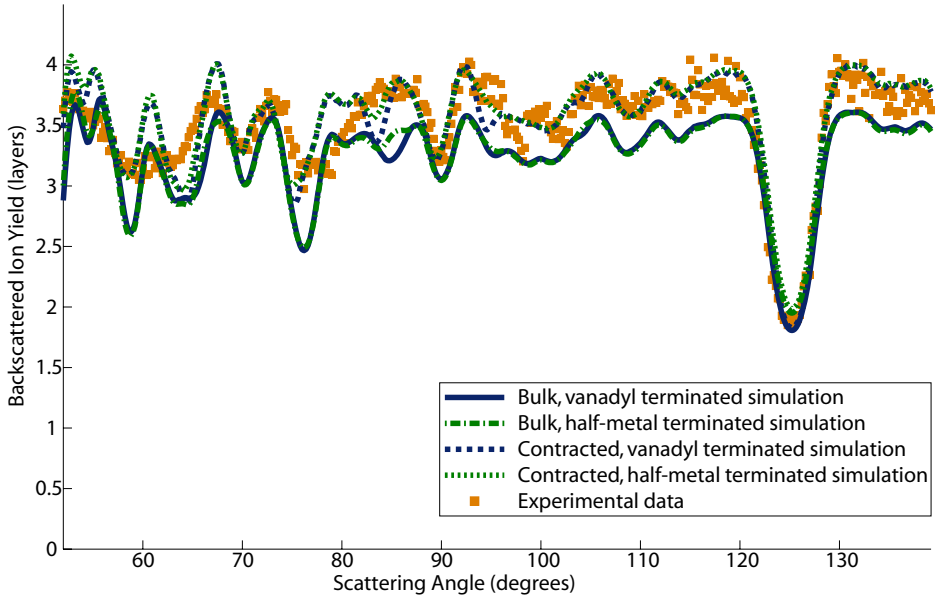

(b) $\langle 10\ \overline{10}\ 03 \rangle$ incidence direction.

Figure 4.20: VEGAS simulations for the structure with the rotation about the normal to the crystal surface 0.9° off from the predicted crystallographic direction. The bulk vanadyl is represented by a solid blue line, the bulk half-metal is represented by a dot-dashed green line. The contracted vanadyl is represented by a dashed blue line and the contracted half-metal is represented by a dotted green line. They are all plotted against the experimental data, shown as orange squares.

Whilst there is some change in yield between the models with a contracted outer layer, due to the enhanced subsurface illumination, and the model without a contracted outer layer, the positions of the blocking dips are relatively unchanged between the models. The difference between half-metal termination and vanadyl terminations are also minimal as demonstrated in the similarity in R-factors between the two terminations. Overall, the blocking dip positions for simulations of imperfect $V_2O_3(0001)$ films are improved in comparison to perfect existing structures, giving rise to better fits. However, with the improvement in blocking dip position comes a great enhancement in backscattered ion yields, with the $\langle 50\overline{5}1\rangle$ simulated curve becoming particularly unfavourable. In addition, the blocking dip positions for the simulations are largely bulk like, suggesting that models of imperfect films have lost sensitivity to the fine structure of the surface, with only minor differences appearing in the simulated curves for different surface structural models.

4.4.2.3 Optimisation of the Kresse O_3 Model

One previously proposed structure that was not examined in the original MEIS study of existing models is that of the Kresse O_3 model, see Figure 4.21. This was excluded from the original study of existing models because it is expected that this structure would form only in an oxygen rich environment, which was not believed to be present during the film preparations, based upon the recorded partial pressures of 2×10^{-7} mbar of oxygen in the preparation chamber.

An initial VEGAS simulation on this trial structure yielded promising blocking curves, see Figure 4.22, with the experimental blocking features being broadly reproduced in the simulation, with low R-factors of 0.054 for the $\langle 50\overline{5}1\rangle$ incidence direction, and 0.25 for the $\langle 10\ \overline{10}\ 03\rangle$ incidence direction giving an overall R-factor of 0.16. This structure was then optimised using R-factor analysis. Four different structural parameters were varied for the structure: rumpling of the vanadium trilayer, $V_2{-}V"_{top} = V"_{top}{-}V'_{top}$; interlayer spacing between vanadium trilayer and single vanadium layer, $V_3{-}V_2$; interlayer spacing between single vanadium

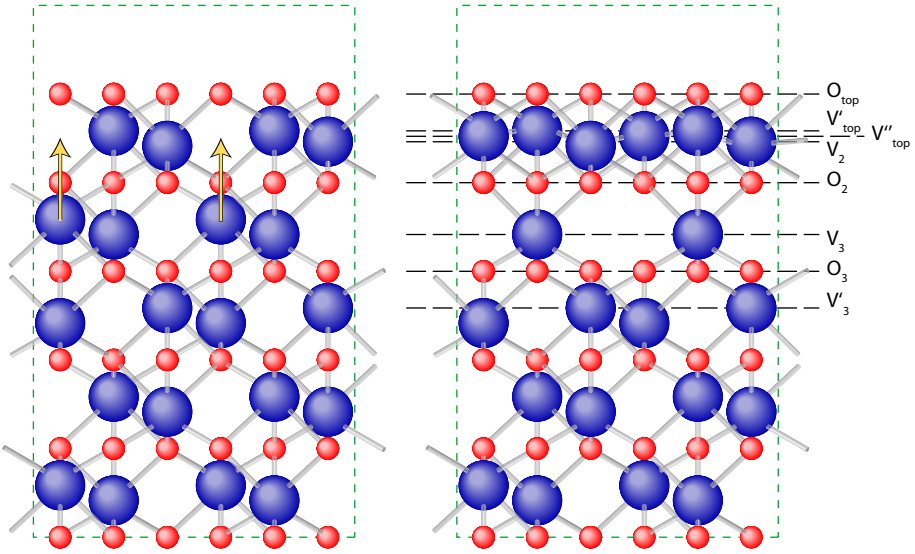

(a) Bulk-like oxygen termination. (b) Kresse O_3 model for an energetically stable, oxygen terminated $V_2O_3(0001)$ surface.

Figure 4.21: Side view of two oxygen terminated $V_2O_3(0001)$ structures. The large blue atoms represent the vanadium atoms and the smaller red atoms represent the oxygen. The dashed green box represents the size of the unit cell. Figure (a) shows the bulk like corundum structure terminated with an oxygen layer, the arrows demonstrate the shift of the vanadium atoms from the second layer into the first, which produces the Kresse O_3 model shown in Figure (b).

layer and double-metal vanadium layer, V'$_3$−V$_3$; and vibrational amplitude of the vanadium atoms, with vibrational amplitudes of vanadium atoms in different sites considered independently. Once again, whilst oxygen atoms were included in the model structure, no information could be ascertained about their true position, or similarly their vibrational amplitudes, which were set to the same value as the bulk vanadium atoms. In order to reduce computation time, the R-factor analysis was performed on just the $\langle 50\bar{5}1 \rangle$ incidence direction.

Figure 4.23 shows an R-factor contour plot for varying the interlayer spacing, V$_3$−V$_2$, against varying the interlayer spacing, V'$_3$−V$_3$, as these two parameters proved to have the greatest affect on the overall shape of the blocking curve. Enhanced vibrational amplitudes of 0.085 Å^2 were optimal for all atoms apart from

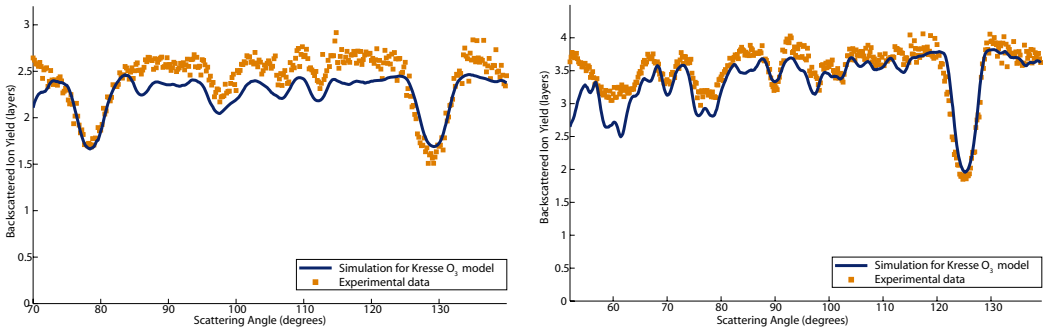

(a) $\langle 50\overline{5}1\rangle$ incidence direction.

(b) $\langle 10\ \overline{10}\ 03\rangle$ incidence direction.

Figure 4.22: VEGAS simulations for the Kresse O_3 structure, shown as a solid blue line, plotted against the experimental data, shown as orange squares.

the vibrational amplitude of the vanadium trilayer perpendicular to the surface, which was found to be 0.12 Å^2, because the trilayer is only relatively weakly bound to the oxygen layer below. Using the R-factor contour plot, the optimum interlayer spacings were deduced from the minimal R-factor. Figure 4.24 shows the simulated blocking curves against the experimental data for the two azimuths studied with these interlayer spacings. The fits are visually very good, and both azimuths have low R-factors contributing to a low overall R-factor. The final parameters of this structure with its R-factors are given in Table 4.6 and compared to the best structural parameters based on the initial study of existing models and also the best structural parameters obtained assuming an imperfect film with an outer vanadium layer contraction. The absolute backscattered ion yield is determined via use of the calibration sample (see section 5.4.2.1), with the typical error in the yield by use of this method deemed to be ±5%. Based on this error in the yield, there must also be some uncertainty in the calculated interlayer spacings between any two consecutive vanadium layers. This is estimated to be ±0.06 Å.

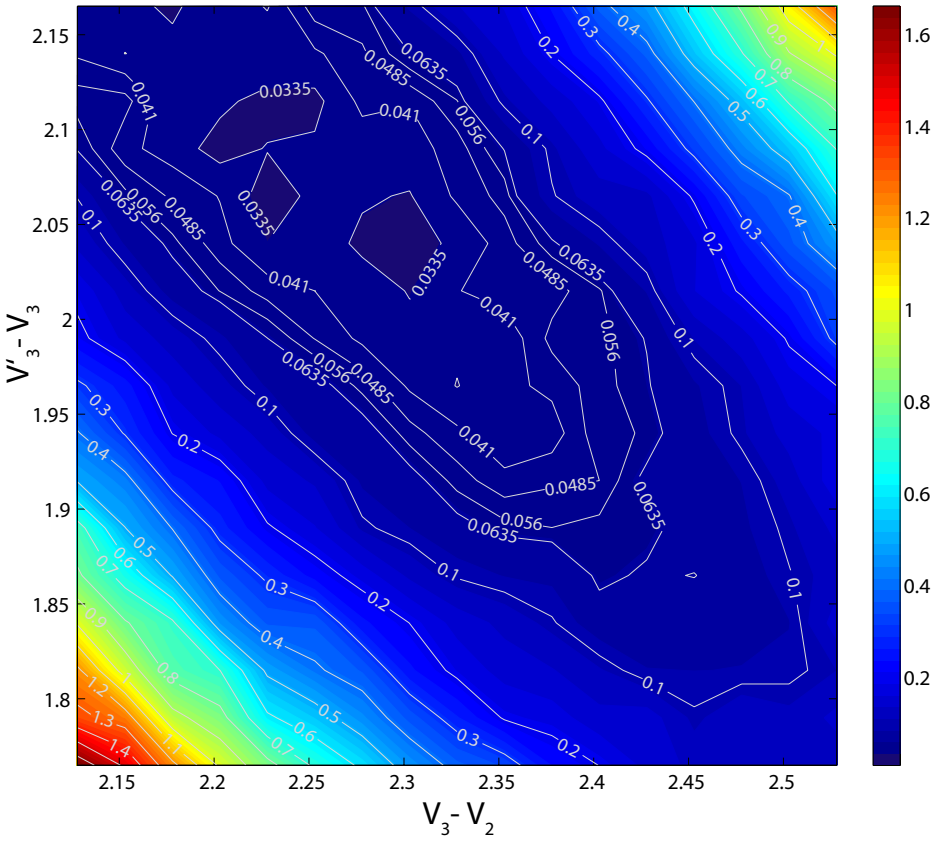

Figure 4.23: R-factor contour plot showing the change in R-factor with two changing interlayer spacings: V"$_2$−V$_2$ against V'$_3$−V"$_2$. This plot was used to find a global R-factor minimum in order to optimise the Kresse O$_3$ model.

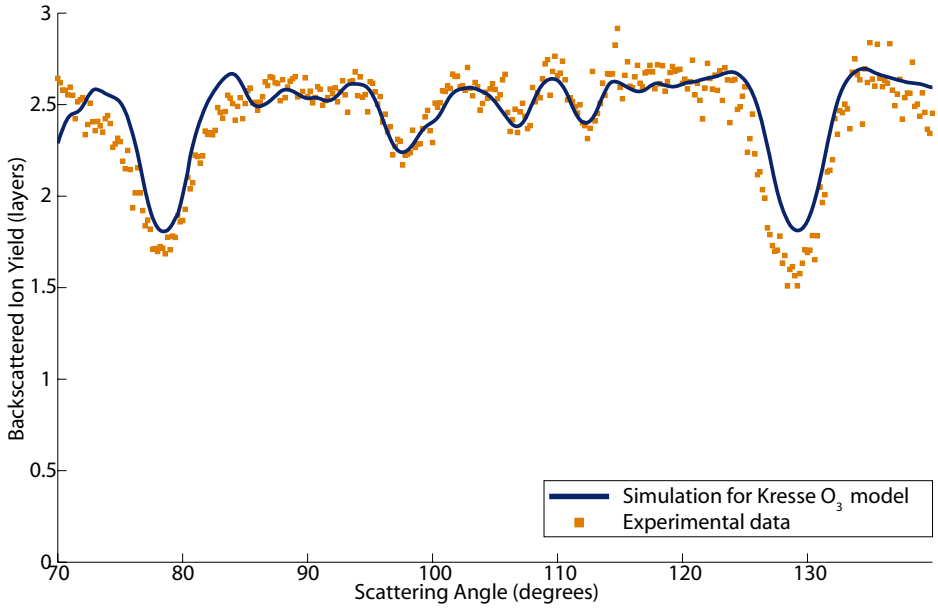

(a) $\langle 50\overline{5}1 \rangle$ incidence direction.

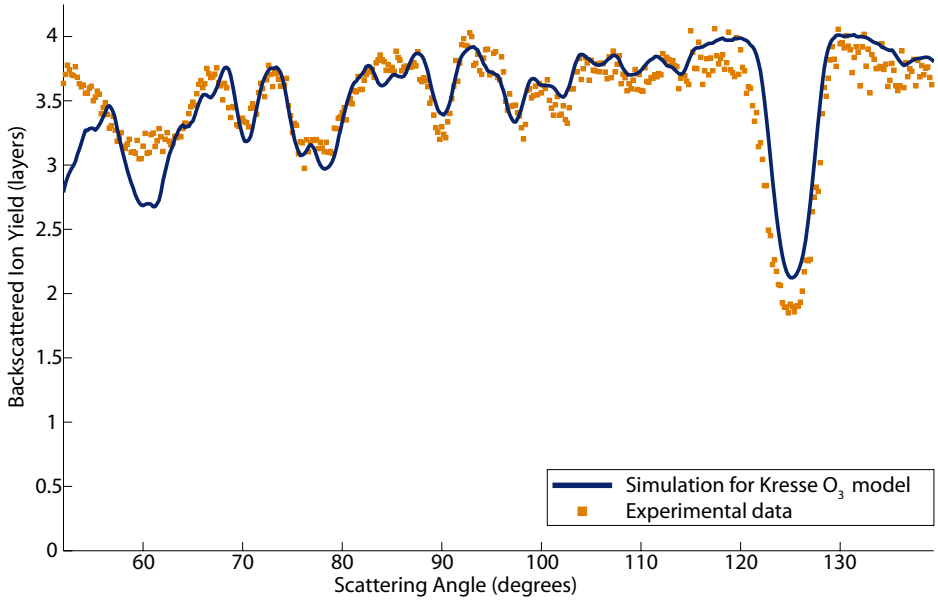

(b) $\langle 10\ \overline{10}\ 03 \rangle$ incidence direction.

Figure 4.24: VEGAS simulations for the optimised Kresse O_3 structure, shown as a solid blue line, plotted against the experimental data, shown as orange squares.

Parameter	Best structural parameters from an existing model: Kröger half-metal	Best structural parameters from an imperfect film: vanadyl structure, 1° off aligned incidence	Optimised Kresse O_3 structure	Initial Kresse O_3 structure
$\langle 50\bar{5}1\rangle$ R-factor	0.13	0.056	0.032	0.054
$\langle 10\ \overline{10}\ 03\rangle$ R-factor	0.36	0.24	0.16	0.25
Total R-factor	0.26	0.16	0.10	0.16
V_{top} =O (Å)	–	1.60	–	–
$O_{top}-V_{top}$ (Å)	0.68	0.68	–	–
$V'_{top}-O_{top}$ (Å)	0.93	0.98	0.98	0.98
$V''_{top}-V'_{top}$ (Å)	–	–	0.18	0.20
$V_2-V''_{top}$ (Å)	–	–	0.18	0.20
$V_2-V'_{top}$ (Å)	0.35	0.36	–	–
O_2-V_2 (Å)	1.02	0.98	0.98	1.00
V'_2-O_2 (Å)	0.98	0.98	–	–
V_3-O_2 (Å)	–	–	1.25	1.44
$V_3-V'_2$ (Å)	0.36	0.36	–	–
O_3-V_3 (Å)	–	–	0.98	1.06
O_3-V_3 (Å)	0.98	0.98	–	–
V'_3-O_3 (Å)	0.98	0.98	1.11	1.00

Table 4.6: Summary of the best structural parameters obtained from the structures tested and the corresponding MEIS R-factors found by comparison of the simulations with the experimental data.

4.5 Conclusions

4.5.1 Interface Analysis

$V_2O_3(0001)$ films have been prepared on two different substrates, Au(111) and Pd(111) using a variety of different growth conditions. Simulations of energy cuts compared to data obtained from these preparations yielded qualitative information about the different types of interface formed.

Thin $V_2O_3(0001)$ films in a range of thicknesses, could be formed on the Pd(111) surface, using a well established method, see Kröger *et al.* [59] and references therein. However, it was found that these thin $V_2O_3(0001)$ films, when grown on palladium, had a large distribution of thicknesses, with a variation of $50-75\%$ in the thickness of the $V_2O_3(0001)$ films.

Thicker films (> 100 Å) could also be grown on the Pd(111) surface using a method proposed by Dupuis *et al.* [49] for growth of films on Au(111). These films yielded a good degree of crystallinity in the $V_2O_3(0001)$ overlayer. Whilst the thickness distribution of the thick films was decreased compared to thinner films, the variation of thicknesses was still relatively high at $\sim 20\%$ of the thickness of the $V_2O_3(0001)$ films.

Thin $V_2O_3(0001)$ films grown on Au(111) were found to form islands with bare patches of gold still visible, rather than the more uniform coverage possible on the Pd(111) substrate. Increasing the number of doses of $V_2O_3(0001)$ onto the Au(111) substrate increased the proportion of Au(111) surface coverage, however islands were found to form in every study conducted using this preparation method on Au(111).

Depositing for longer periods of time produced $V_2O_3(0001)$ films grown on the Au(111) surface with a high degree of crystallinity and with only a small distribution of thicknesses found, with a variation of $\sim 8\%$ in the thicknesses of the thick

$V_2O_3(0001)$ films. Overall, this method of growing films on the Au(111) substrate yielded the highest quality $V_2O_3(0001)$ films, with minimal thickness distribution in the $V_2O_3(0001)$ films and a high degree of crystallinity. Therefore these were the films used for the structural analysis.

4.5.2 Structural Analysis

Initial investigations concentrated on running VEGAS simulations of previous existing models. For each of these structures, it was found that the half-metal termination yielded a marginally better fit between simulation and data than the vanadyl termination. However in general the differences in the simulations were relatively subtle and none produced a satisfactory simulated blocking curve for both azimuths tested.

Further investigations were then conducted on imperfect films as the experimental data yielded more bulk blocking features than predicted for a perfect film. This analysis was performed by assuming two different types of misalignment in the channelling direction, which could be consistent with imperfections between different regions of the $V_2O_3(0001)$ films. The simulation producing the best fit was found to be a vanadyl structure 1° off aligned incidence. However, the sensitivity to fine structural detail of the surface was inhibited by increased subsurface illumination resulting from assuming imperfections.

The final investigation was based upon optimising the promising Kresse O_3 structure. This structure yielded a very good visual fit and low R-factors in both azimuths, so this model is favoured by the MEIS structural investigation. However, it is unclear from the study by Kresse *et al.* as to the magnitude of the oxygen rich environment necessary in order to form this structure; as such it is not known whether the oxygen partial pressure, in which the films for this study were grown, was high enough for the formation of the Kresse O_3 structure. It is also important to consider how this result could be consistent with existing studies. Based upon

the results from this study, the PhD data of Kröger *et al.* was re-examined and simulations were performed for the Kresse O_3 structure [77]. This new investigation found that the Kresse O_3 structure does indeed yield simulations that are compatible with the experimental PhD data. The identification of a V=O stretching frequency in the EELS studies [49, 69] does not appear to be consistent with this proposed oxygen termination, however, an STM study [70] has been interpreted as showing the existence of regions with two different terminations: the vanadyl termination and an oxygen termination, therefore it is plausible that both terminations can coexist. Now that this MEIS investigation has identified further positive evidence of this possibility, further MEIS studies on the termination of the $V_2O_3(0001)$ surface in the future could examine in detail how different concentrations of the two terminations affect the simulated MEIS blocking curves, and how different conditions for sample preparation affect this potential coexistence.

Chapter 5

Ag_2S films Grown on Ag(111)

5.1 Introduction

Thick metal sulphide films have a number of different applications in technology: they are used as passive barriers to prevent corrosion; they can serve as active components of microelectronic devices; they can be used to model systems for studying heterogeneous catalysis. In order to understand the properties of these films it is often useful to first elucidate the structure of much thinner films, as well as studying the interface between the film and the substrate. Monolayer adsorption of sulphur on single crystal metals is believed to have potential applications in light-emitting and photovoltaic devices [78], which provides further incentive to investigate the structure of these ultrathin films.

A great deal of interest in the Ag_2S/Ag(111) system also comes about due to its similarity with the surface produced by deposition of methylthiolate (CH_3S-) onto an Ag(111) surface by exposing the surface to either methanethiol (CH_3SH) or dimethyl disulphide ($(CH_3)_2$) [79]. This system forms an alkanethiolate self-assembled monolayer (SAM), which produces a $(\sqrt{7} \times \sqrt{7})R19.1^\circ$ surface phase - the same phase as seen for thin silver sulphide films grown on Ag(111). SAMs have a wide variety of potential uses in technology because they form a stable, well-ordered, organic surface. Methanethiol is the simplest of the alkanethiols and as a

result its reaction with different noble metal surfaces, has been widely studied. The structure of methanethiol on Ag(111) has been proposed based on STM analysis [80], and corroborated using NIXSW [81] and MEIS [82]. The result from these studies provides insight into the possible structure expected for the similar phase of the silver sulphide.

5.2 Previous work

The first major investigation into silver sulphide on Ag(111) was conducted in the late 1970s by Schwaha *et al.* [83], depositing atomic sulphur from gas-phase S_2 onto the Ag(111) surface. Using LEED, two different phases were identified. After deposition of one layer of sulphur atoms, a complex LEED pattern was observed, which was attributed to a $(\sqrt{39} \times \sqrt{39})R16.1^\circ$ structure, with two possible structural models proposed. Upon further sulphur deposition, a second LEED pattern was formed, which was identified as corresponding to a $(\sqrt{7} \times \sqrt{7})R19.1^\circ$ structure. It was suggested that the existence of this structure was a result of epitaxial growth of (111) oriented $\gamma-Ag_2S$ on the Ag(111) surface, with a slight ($< 1\%$) contraction in the crystal structure of the film required to avoid lattice mismatch, however the locations of the silver atoms were not identified. The uptake of sulphur onto the surface was also examined, using AES, which determined that the sulphur uptake curve levelled off; whilst the thermal desorption uptake curve increased linearly. These curves together imply that a saturated sulphur coverage does not occur and instead a silver sulphide surface with a fixed ratio of S:Ag was growing with increasing sulphur deposition.

In the following period, a number of further investigations were made into the surface phases formed by atomic sulphur deposition onto the Ag(111) surface. These studies used a variety of different sources of the atomic sulphur: gas-phase H_2S [84, 85]; solutions of Na_2S and H_2S [85]; and a solid state electrochemical cell [86, 78, 87, 88]. Irrespective of the deposition method, these studies all identified the presence of a

$(\sqrt{7} \times \sqrt{7})R19.1^\circ$ structure. These papers, all implying Schwaha *et al.* to have made a full structural determination of this phase, provided little in the way of new insight into any reconstruction of the silver atoms. It wasn't until the early 2000s that a more complete structural investigation was undertaken, using neutron diffraction [89]. This study also identified the presence of a $\gamma-Ag_2S$ (although labels it as an $\alpha-$phase). It was proposed that the S atoms of this structure occupy fcc lattice sites, and the majority of Ag atoms appear to occupy tetrahedral sites, although some evidence exists for partial occupation of mixed sites.

A more recent study by Yu *et al.* [1] identified two distinct phases using STM and LEED, in agreement with the early study of Schwaha *et al.* However an alternative interpretation of the LEED pattern observed at low coverage was proposed, namely with a unit mesh described in matrix notation by $\begin{pmatrix} 3.67 & 0.00 \\ 3.00 & 3.50 \end{pmatrix}$. It was suggested that this phase may be too complicated for a full structural investigation to be realised with any current technique, but using normal incidence X-ray standing waves (NIXSW) data estimated a minimum sulphur coverage of 11 S atoms in the unit mesh. This phase is known hereafter as the 'low coverage complex phase'. The study investigated in more depth the higher coverage $(\sqrt{7} \times \sqrt{7})R19.1^\circ$ phase, which was agreed to involve the formation of an epitaxially grown (111) oriented $\gamma-Ag_2S$. Unlike previous studies, an attempt was made to more completely determine this structural phase, and in particular the interface between the silver sulphide and the Ag(111) substrate. The lateral periodicity, whilst identical to that formed by methylthiolate bonded to an Ag(111) surface, was found to form a different structure based on the NIXSW data. The interpretation of the data was that the interface layer is formed with 2/3 of the density of the S atoms in the bulk sulphide with an unreconstructed Ag(111) layer below, and a reconstructed layer of Ag atoms above, consisting of an identical layer to that of a single silver layer in the Ag_2S, as shown in Figure 5.1. The STM data were interpreted as showing a reconstructed Ag layer above the S atoms, however there is no direct evidence of a silver reconstruction.

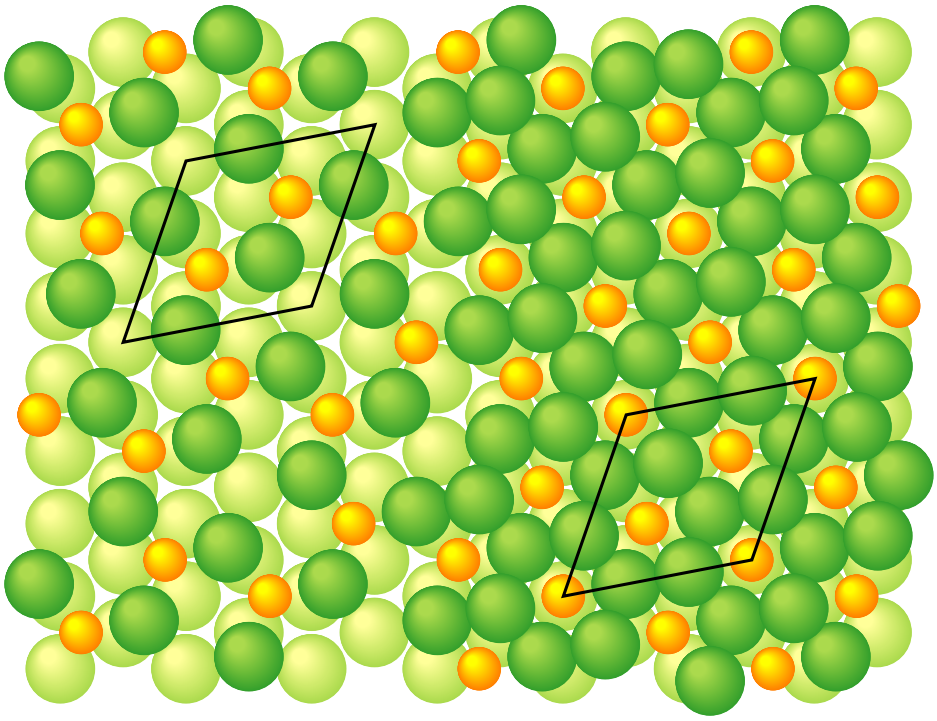

Figure 5.1: Plan view of the model of the Ag(111)($\sqrt{7} \times \sqrt{7}$)R19.1°−S, as proposed by Yu *et al.* [1]. The left hand side shows the first layer of the interface and the right hand side shows the continuation of the epitaxial Ag_2S(111). The surface mesh, which has dimension $\sqrt{7}$ times that of the substrate, is marked by a continuous line. The light green atoms represent the silver atoms in the substrate, the dark green atoms represent the silver atoms in the silver sulphide film, and the small yellow atoms represent the sulphur.

MEIS can be used as a depth profiling tool to confirm that the silver sulphide film thickness continues to increase with increasing sulphur deposition, as deduced by Schwaha *et al.* [83] but so far uncorroborated. MEIS is also capable of confirming the presence of a silver reconstruction as this leads to an enhancement in the yield of backscattered ions. The MEIS blocking curves can be used to conduct a structural investigation of the ($\sqrt{7} \times \sqrt{7}$)R19.1° phase to complement existing studies using other techniques.

5.3 Experimental Method

5.3.1 Preparation

The single metal Ag(111) crystal substrate was cleaned by several cycles of cold sputtering and annealing, see Section 3.2.6, with annealing to temperatures of 600 °C. After several such cycles, the crystal had no peaks attributable to contamination in the AES spectra, therefore it was judged to be clean and had a sharp well-ordered (1×1) LEED pattern down to 56 eV.

The silver sulphide overlayers were prepared by dosing sulphur directly onto the clean Ag(111) surface, using the same method as Schwaha *et al.* [83]. The sulphur was produced using a solid state $Pt/Ag/AgI/Ag_2S/Pt$ electrochemical cell [90], which delivers a flux consisting almost entirely of S_2 molecules. The cell was operated with an applied potential of ~ 150 mV, at a temperature of ~ 180 °C. The LEED pattern and Auger spectrum were examined at regular intervals throughout the deposition process to ensure no contaminants were appearing on the surface and that the expected phases were being produced. An approximation for the deposition rate of the sulphur source was obtained using the Auger spectra and the methodology described at the end of Section 3.1.1. Figure 5.2 shows the result of this analysis. The gradient of the graph changes every 6 mins, giving a deposition rate of ~ 0.15 layers of silver sulphide per min. After 4 layers have been deposited, the gradient becomes zero as it is only possible to detect Auger electrons from within this region of the surface. This analysis provides only an indication of the deposition rate because unavoidable fluctuations in the temperature of the sulphur cell occurred over the period of deposition, which inevitably cause small variations in this rate.

5.3.2 Characterisation

At depositions of $\lesssim 20$ mins, the sample yielded a LEED pattern attributable to the low coverage, complex phase of the silver sulphide overlayer. According to the deposition rate, as determined using AES, 20 mins should produce ~ 3 layers

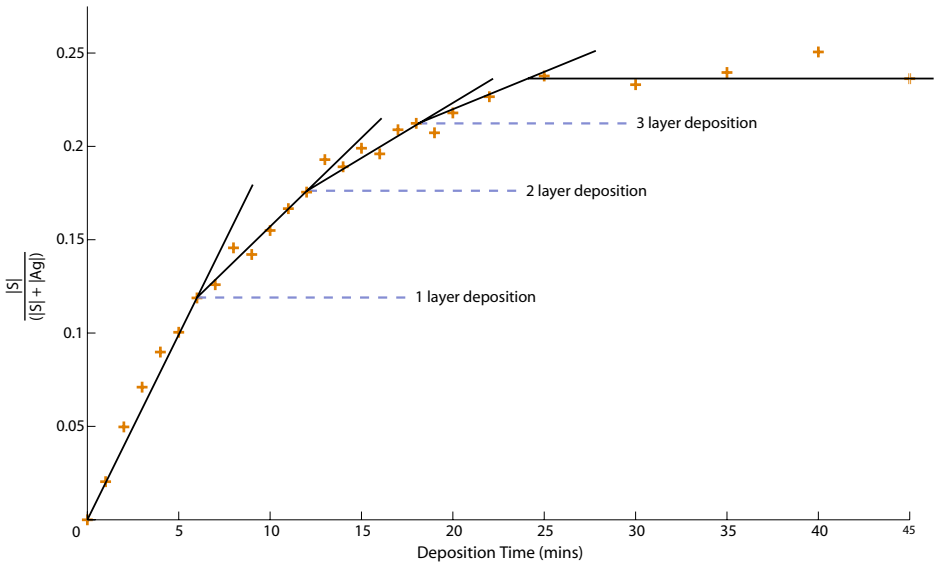

Figure 5.2: Plot of the change in ratio of Auger peaks, $\frac{|S|}{|S|+|Ag|}$, with time. The deposition rate of the sulphur source can be approximated by the gradient changes, which represent a 1 layer deposition.

of silver sulphide, which clearly should not yield the LEED pattern for the low coverage, complex phase (present for $\leq$ 1 layer). However, the $(\sqrt{7} \times \sqrt{7})R19.1°$ LEED pattern is contained within the more complex LEED pattern, so both LEED patterns must be present. This provided an early indication that the silver sulphide overlayer was forming with a range of thicknesses, such that both possible sulphide phases coexist for short ($\lesssim$ 20 mins) deposition times. After depositions of $>$ 20 mins, the sample yielded a well ordered $(\sqrt{7} \times \sqrt{7})R19.1°$ LEED pattern relative to that of the metal substrate, as expected for the Ag_2S structure, see Figure 5.3. The Auger spectrum showed peaks only attributable to silver and sulphur, see Figure 5.4 for an example spectrum obtained from a thick silver sulphide film.

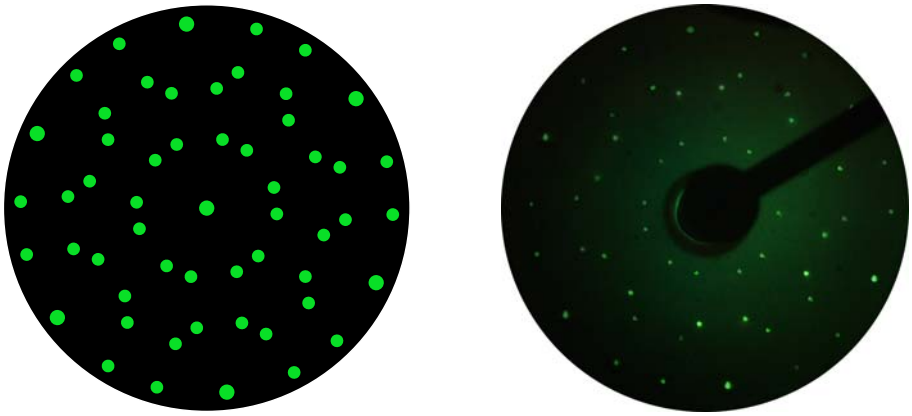

(a) Theoretical $(\sqrt{7} \times \sqrt{7})R19.1^\circ$ LEED pattern, relative to the metal substrate.

(b) LEED pattern obtained at 56 eV after silver sulphide sample preparation, confirming $(\sqrt{7} \times \sqrt{7})R19.1^\circ$ LEED pattern relative to the metal substrate.

Figure 5.3: Figure showing comparison between theoretical LEED pattern and experimentally obtained LEED pattern at 56 eV. Figure (a) shows the theoretical pattern, Figure (b) shows the experimentally obtained LEED pattern confirming the presence of a $(\sqrt{7} \times \sqrt{7})R19.1^\circ$ LEED pattern, relative to the metal substrate.

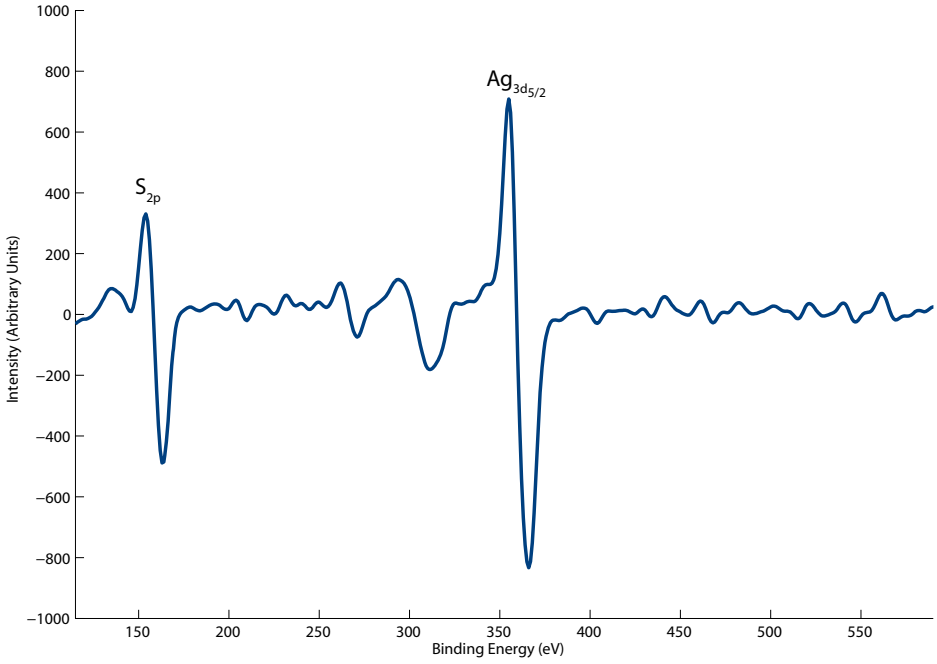

Figure 5.4: An example Auger spectrum of Ag_2S/Ag(111) obtained from a film yielding the LEED pattern for the $(\sqrt{7} \times \sqrt{7})R19.1^\circ$ phase.

Confirmation of the proposed Ag_2S stoichiometry was obtained from the MEIS data. Figure 5.5 demonstrates the process used to determine the correct stoichiometry of the silver sulphide films. Figure 5.5(a) shows the raw data obtained from an energy spectrum obtained from one preparation of a thick silver sulphide film. The sulphur peak sits on a background from the silver which increases with energy loss. This simple linear background from the silver (as shown in Figure 5.5(a)) is removed from the data. The result of the background removal is given in Figure 5.5(b), along with a simple fit to the data obtained using SIMNRA [72]. The sulphur peak is then extracted, and scaled in amplitude by a ratio of the squared atomic numbers, $\frac{47^2}{16^2}$, to correct for the different scattering cross-sections of silver and sulphur, and further scaled in amplitude by $\frac{2}{1}$ to account for the proposed ratio of silver to sulphur in Ag_2S. The scaled sulphur surface peak is then translated in energy, to account for the difference in energy losses, and is overlaid on the silver surface peak giving rise to Figure 5.5(c). Whilst the corrected sulphur peak is very noisy due to the low count rate of the relatively light element, this figure shows that the magnitude of the scaled sulphur surface peak is consistent with a stoichiometry of Ag_2S for the silver sulphide film.

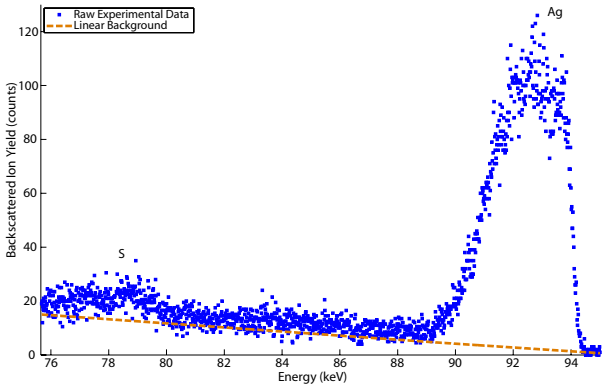

(a) Uncorrected raw data, shown as points, with linear background shown as a dashed line.

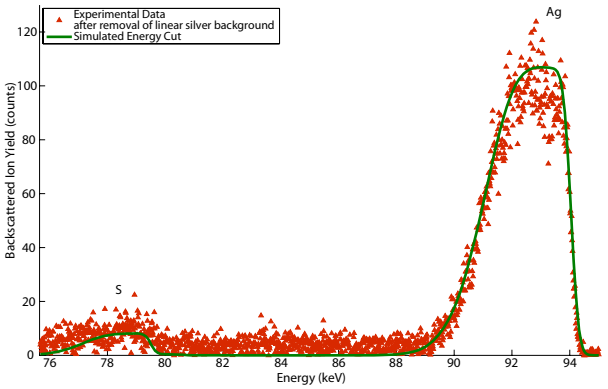

(b) Data with background removed, shown as points. Also shown, as a solid line, is the corresponding SIMNRA simulation.

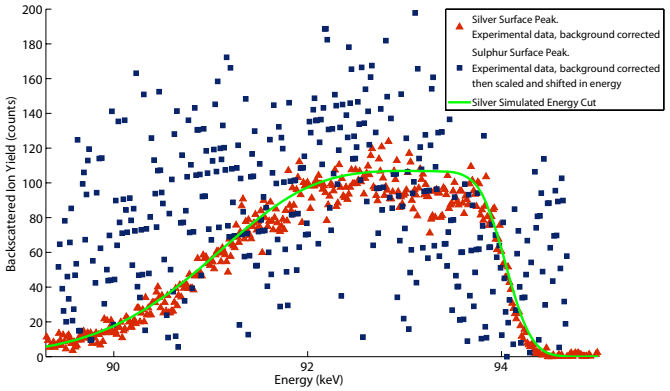

(c) Silver surface peak, shown as red triangles, with solid line representing the SIMNRA simulation. The scaled and shifted sulphur surface peak, shown as blue squares, is consistent in shape and magnitude to the silver surface peak.

Figure 5.5: Figure showing stages used for confirming stoichiometry of the silver sulphide films. Figure (a) shows an energy cut with the raw uncorrected data, Figure (b) shows the data corrected for background along with SIMNRA simulation and Figure (c) compares the corrected silver surface peak along with a scaled and shifted sulphur peak. The peaks overlap confirming a stoichiometry of 2:1.

5.3.3 Measurements

MEIS data were taken using an 100 keV He^+ ion beam with a dose of 0.25 μC per tile, and with no area of the surface exposed to more than 1 μC, after which unacceptable signs of radiation damage can be observed (see Section 5.3.4 for more details). A further three repeats of each data set were obtained, each on a different crystal spot, in order to improve statistics by creating a data set with an effective dose of 1 μC per tile. Data were obtained on different preparations of the Ag_2S surface, for different coverages, including one data set on the low coverage complex silver sulphide phase, and a number of different thicknesses which exhibited the $(\sqrt{7} \times \sqrt{7})R19.1^\circ$ LEED pattern. Some data were also obtained on the clean Ag(111) surface for comparison, particularly of the backscattered ion yields.

Data were taken in incidence geometries aligned along crystallographic directions within the Ag(111) substrate. These data were taken with a nominal one layer illumination of the substrate, $\langle\overline{11}0\rangle$ incidence direction, over a scattering range of $83^\circ - 134^\circ$, and a nominal two layer illumination of the substrate, $\langle\overline{211}\rangle$ incidence direction, over a scattering range of $85^\circ - 134^\circ$. Figure 5.6 shows these incidence directions within the relevant plane of the substrate, along with the major blocking directions observed in the data. Also included is a section of a silver sulphide film above the Ag(111) surface, for the structure proposed by Yu *et al.* [1] (see Figure 5.1 for a plan view of this model). It is important to note that due to the rotation of the film with respect to the substrate, the atoms shown do not lie perfectly within this vertical plane of the substrate, and will only be partially visible to the ion beam in the directions shown, as such the distribution of silver atoms is essentially random in the data acquired.

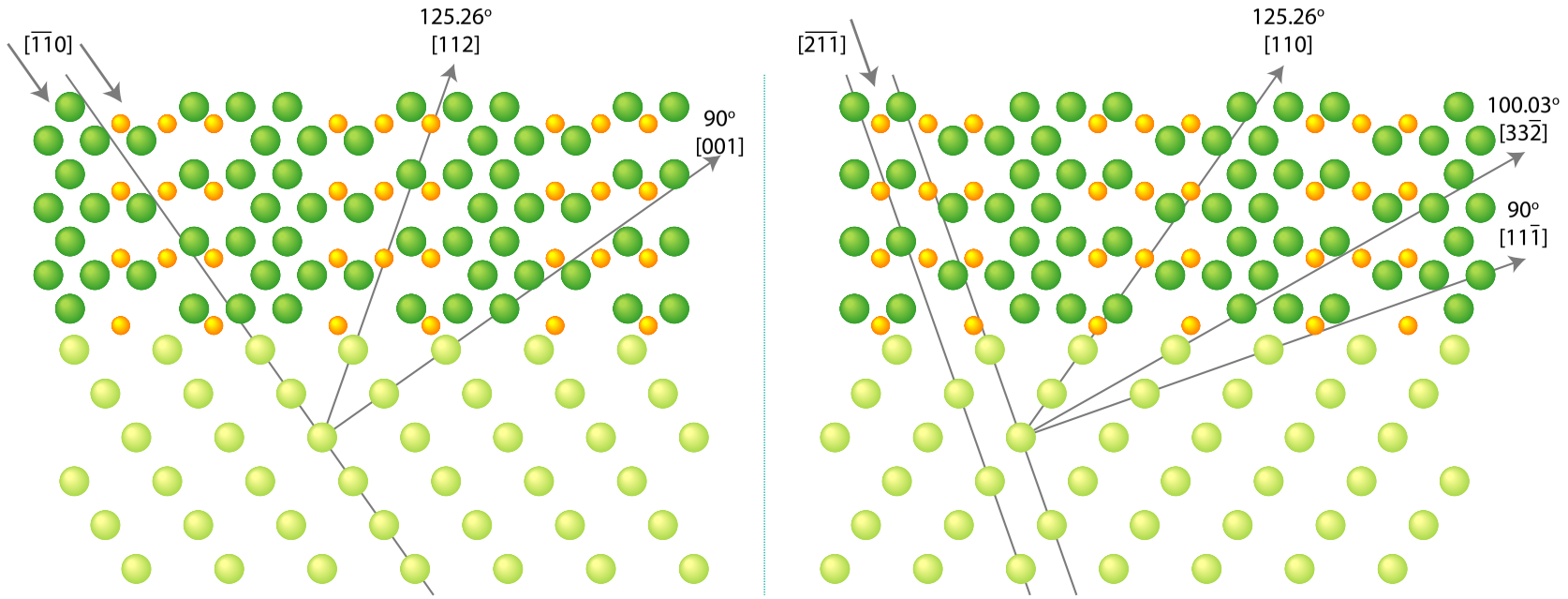

Figure 5.6: Side view of several layers of Ag_2S film grown on Ag(111). The figure shows a cross-section along the (211) azimuth of the Ag(111) substrate. The light green atoms represent the silver atoms in the substrate, the dark green atoms represent the silver atoms in the silver sulphide film, and the small yellow atoms represent the sulphur. Note that due to the rotation of the sulphide film with respect to the substrate, the atoms shown within the sulphide film do not lie in the same vertical plane as the substrate.

5.3.4 Beam Damage Survey

The technique of MEIS is generally considered to be non-destructive for the majority of crystal surfaces. However, in the case of a compound surface the potential for beam-induced damage is greatly increased when compared to a metal single crystal (see section 4.3.4 for more details). Sulphur has a relatively low atomic number and therefore, like the oxygen contained within the V_2O_3 discussed in section 4.3.4, will result in a large recoil energy via equation 2.1. There have been no known previous MEIS studies of metal sulphide surfaces, and therefore there was no indication as to the magnitude of any effect that the surface was likely to experience due to beam-induced damage. As such, it was important to investigate the rate of any beam-induced damage of the Ag_2S surface to determine if this surface could be successfully studied using MEIS and, if so, the maximum reasonable exposure possible for experimentation.

Initial experiments concentrated on investigating the scale of beam-induced damage for 100 keV H^+ incident ions. These were conducted by recording the low energy back edge of the silver surface peak for successive incident ion doses on the same position of the crystal surface. The low energy edge of the silver peak was recorded because this region represents backscattering from atoms just below the surface where beam-induced damage is known to typically occur. Therefore this region of the spectrum is likely to show the most significant effects. Preliminary data were obtained from the most surface specific geometry within the substrate, namely a double-alignment geometry. This was used to minimise the backscattered ion yield obtained from the Ag(111) substrate and hence the majority of the intensity of ions backscattered from the silver is from the sulphide, which enables the observation of any signs of damage occurring in the sulphide film. The geometry chosen was $\langle\overline{1}10\rangle$ incidence, $\langle\overline{1}14\rangle$ detection with respect to the substrate (15.78° grazing angle), with the low scattering angle chosen because the resulting longer ion trajectories through the film have potential for greater effects from beam-induced damage.

During data acquisition, it became quickly apparent that the silver sulphide was experiencing a severe beam-induced effect. Due to this, the survey was taken with an incremental dose of 0.1 μC between each tile to obtain an estimate for the rate at which beam-induced damage was occurring. At this low dose it was necessary to take a projection of the entire tile for the energy cut because the count rate was exceptionally low in the double-alignment blocking dip. The result of this is a reduction in surface sensitivity, because the data were no longer obtained from a double-alignment region. Further data acquisition was from $\langle\overline{1}10\rangle$ incidence, with detection over a full 27° angular range centred on $\langle\overline{1}14\rangle$ scattering angle (15.78° grazing angle). Figure 5.7 shows the resultant scattered ion energy spectra corresponding to scattering from the Ag atoms. After just a 0.3 μC dose, the magnitude of the spectrum has decreased and after a 2 μC dose, the spectrum is approximately half of the initial magnitude. In order to gauge the rate of

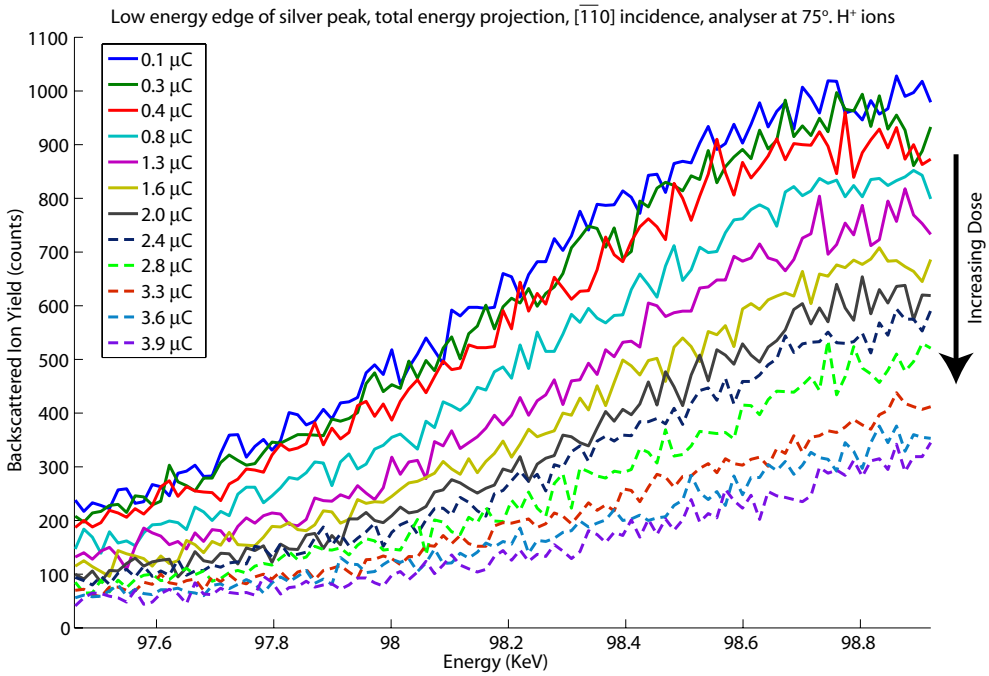

Figure 5.7: Beam-induced damage survey for 100 keV H^+ ion beam. The energy spectra are obtained by scattering from silver atoms for a silver sulphide film, for successive ion beam doses on one crystal spot. The peak magnitude decreases constantly with increasing dose.

beam-induced damage, each peak was integrated and plotted against dose, which shows how the backscattered ion yield (in counts) varies with the total dose received on the sample. The result of this plot can be seen in Figure 5.8.

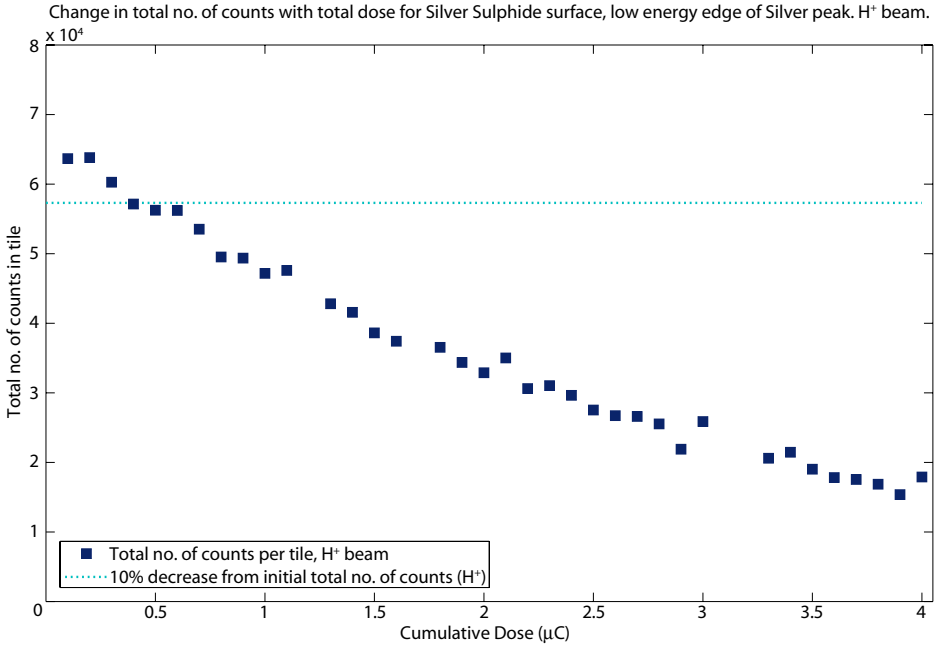

Figure 5.8: The plot of backscattered ion yield against cumulative dose demonstrates how the yield varies with the total dose of H^+ ions received on the silver sulphide sample. The yield decreases steadily with increasing dose.

Whilst it is far from ideal to take data on a system in which any sign of beam-induced damage is occurring, it is clear that it would be impossible to take data on the silver sulphide, using an hydrogen ion beam without accepting some small change in backscattered ion yield. If a 10% degradation in signal is accepted (the magnitude of this is marked by the dashed line in Figure 5.8), then the total ion dose possible on any one spot of the crystal must be limited to < 0.4 μC. The silver surface peak crosses two tiles and therefore the ion dose per tile must be < 0.2 μC. Data taken at this dose would be statistically poor and therefore many repeats would be necessary in order to obtain data of a high enough quality to observe any structural detail in blocking curves. Overall, one data set would require in excess of 100 different spots on the crystal, which is clearly unfeasible.

It appeared unlikely that this extreme level of beam-induced damage, which is highly unusual for an H^+ ion beam, could be a result of physical damage alone, and therefore a similar investigation was conducted for 100 keV He^+ incident ions. The greater mass of helium compared to hydrogen typically results in a more rapid beam-induced damage of the surface region, therefore the survey for the He^+ incident ions was conducted with the dose on the sample taken with an increment of 0.05 μC. As for the hydrogen beam, the energy cuts obtained from the projection of the entire tile were compared. The kinematic factor gives rise to a steeper gradient of the surface peak for helium and therefore projection of an entire tile loses definition of the surface peak. Figure 5.9 shows the resultant scattered He^+ ion energy spectra corresponding to scattering from the silver atoms. In this case, the first change in spectrum occurs at a 1 μC dose.

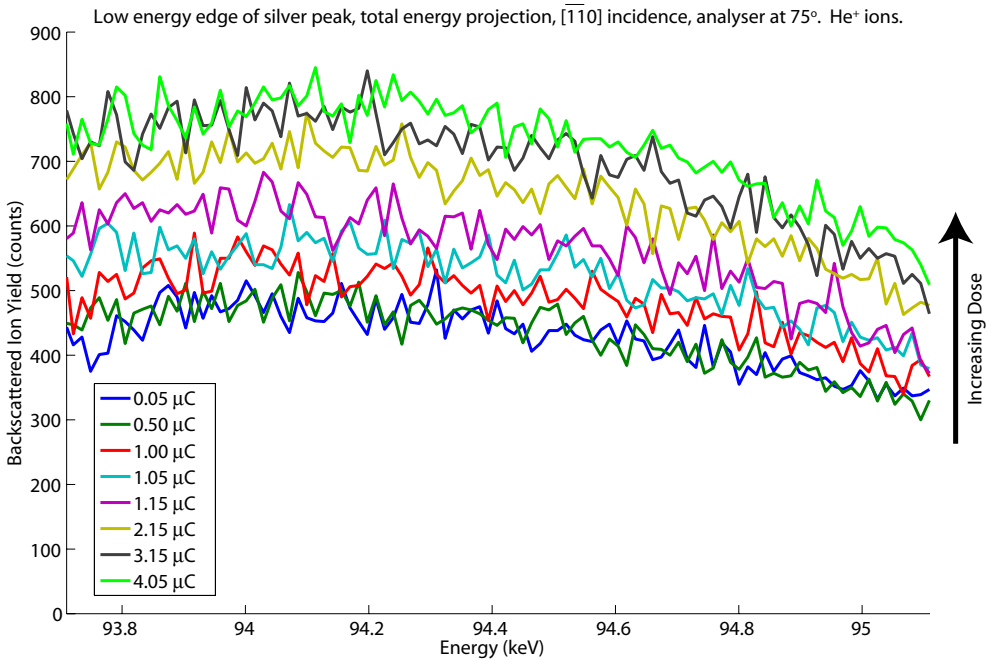

Figure 5.9: Beam-induced damage survey for 100 keV He^+ ion beam. The energy spectra are obtained by scattering from silver atoms for a silver sulphide film, for successive ion beam doses on one crystal spot. The peak magnitude decreases constantly with increasing dose.

In order to gauge the rate of beam-induced damage, each peak was integrated and plotted against dose, which shows how the backscattered ion yield (in counts) varies with the total dose received on the sample. The result of this plot can be seen in Figure 5.10.

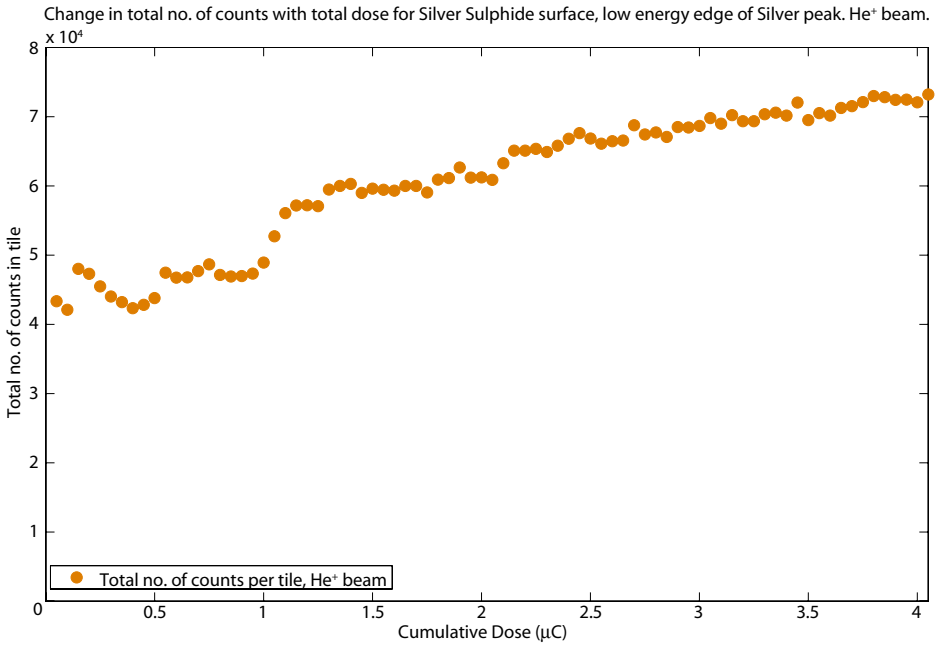

Figure 5.10: The plot of backscattered ion yield against cumulative dose demonstrates how the yield varies with the total dose of He^+ ions received on the silver sulphide sample. The yield remains approximately constant up to a dose of 1 μC, at which point there is a sharp increase in the yield and a steady rise thereafter with increasing dose.

This plot shows that the backscattered ion yield remains approximately constant up to a dose of 1 μC, at which point there is a sharp increase in the yield and a steady rise thereafter with increasing dose. This suggests that a total dose of 1 μC per crystal spot can be applied to the surface. The silver peak with an helium beam crosses 4 tiles due to its steep gradient, therefore each tile could receive a dose of 0.25 μC. Four data sets would be required to obtain reasonable statistics for the blocking curves. This would still require a large number of different spots on the crystal, however, this quantity would now be attainable.

Based on this evaluation, data were taken with an He^+ ion beam at a dose of 0.25 μC, with the total dose taken at any one position on the crystal kept at 1 μC. This condition was achieved by regularly changing the position of the ion beam spot on the surface, by moving the sample perpendicular to the beam. This maximum dose was chosen because the data were deemed to show no significant signs of damage occurring at this level.

Interestingly, the total number of counts per tile increases with increasing dose for the He^+ ion beam, but decreases with increasing dose for the H^+ ion beam. The behaviour of the data when the sample is subjected to an He^+ ion beam, is the effect expected when a surface experiences beam-induced damage. The ions produce physical damage in the sub-surface region of the silver sulphide film, causing atomic displacements. The displaced atoms lead to an increase in the backscattered ion yield from subsurface silver atoms and to more de-channelling. The behaviour of the data when the sample is subjected to an H^+ ion beam is far more unusual. It seems that the ions are not inducing physical damage within the near surface region, which would cause an increase in the backscattered ion yield; instead it appears that the most likely explanation is that the ions are inducing chemical damage. It is believed that hydrogen, originating from the H^+ ion beam, reacts with the sulphur in the silver sulphide forming H_2S, which is emitted from the surface. The removal of the sulphur from the silver sulphide layer causes the surface to revert to an ordered Ag(111) surface, with the restoration of this structure resulting in a decrease in the backscattered ion yield.

5.4 Results and Discussion

5.4.1 Depth Profile Information

Unlike the other surface science techniques that have been used to study the silver sulphide system, MEIS is not intrinsically surface specific and is therefore capable of determining the thicknesses of the silver sulphide films grown. Schwaha *et al.*

[83] interpreted the levelling off of the AES sulphur uptake curve, combined with a linear increase of the thermal desorption uptake curve, as the growth of a silver sulphide surface with a fixed ratio of S:Ag with increasing sulphur deposition. MEIS can yield information on the depth profile (the composition of sample as a function of depth) of the films and should therefore be able to confirm this interpretation.

In order to evaluate the depth profiles, simple simulations of the experimental ion energy spectra for the different preparations were performed. The simulation software used for this was SIMNRA [72], a code developed for RBS analysis but commonly used in MEIS depth profiling analysis for data obtained from an incidence direction of the ion beam not aligned to a crystallographic direction of the sample, which is the case for the silver sulphide overlayer. The software is able to model different parameters that characterise the sample including composition, surface roughness (rough layers or substrate) and layer thickness, which can be modelled as a distribution of thicknesses. The software is then able to modify these parameters in order to optimise the fit between the simulation and the experimental data.

Figures 5.11 and 5.12 show the results of the simulations performed for different preparations of the silver sulphide films, as well as a clean Ag(111) spectrum for comparison (shown in Figure 5.11(a)). Figure 5.11(b) gives results obtained by deposition of sulphur for a length of 20 minutes. This preparation yielded the LEED pattern for the complex phase, however the deposition rate indicated a greater than 1 ML deposition suggesting the possible coexistence of areas of the complex phase and areas of the $(\sqrt{7} \times \sqrt{7})R19.1^\circ$ phase (the LEED pattern for this phase is contained within the LEED pattern of the complex phase and therefore would not be separately identifiable). Figure 5.12(a) gives results obtained by deposition of sulphur for a length of 40 minutes and Figure 5.12(b) gives results obtained by deposition of sulphur for a length of 80 minutes. Both of these preparations yielded the $(\sqrt{7} \times \sqrt{7})R19.1^\circ$ LEED pattern.

After 20 mins deposition, the silver surface peak shows a considerably higher backscattered ion yield compared to the clean silver surface peak, which is expected for reconstruction of the silver within the sulphide overlayer. The surface peak has also broadened in comparison to the clean silver surface peak and both silver and sulphur surface peaks appear asymmetric, consistent with the distribution of thicknesses inferred from the LEED pattern observed and the deposition rate. After 40 mins deposition, the backscattered ion yield of the silver surface peak is further increased compared to the clean silver surface peak. The surface peaks have also broadened in comparison to those seen for the spectrum recorded after the shorter deposition time. Both factors are consistent with an increasing thickness of silver sulphide film. The surface peaks also show a greater degree of asymmetry implying a larger distribution of thicknesses in the sulphide films. After 80 mins deposition, the surface peaks are more rectangular than previously, consistent with a thicker film with atom positions that are inequivalent to the substrate. The peaks maintain an asymmetry implying that a distribution of thicknesses of the sulphide film still exists. All of the silver sulphide films had a stoichiometry consistent with Ag_2S films, determined as demonstrated in Section 5.3.2. These observations were used to create initial models for the depth profile, which were then optimised using SIMNRA.

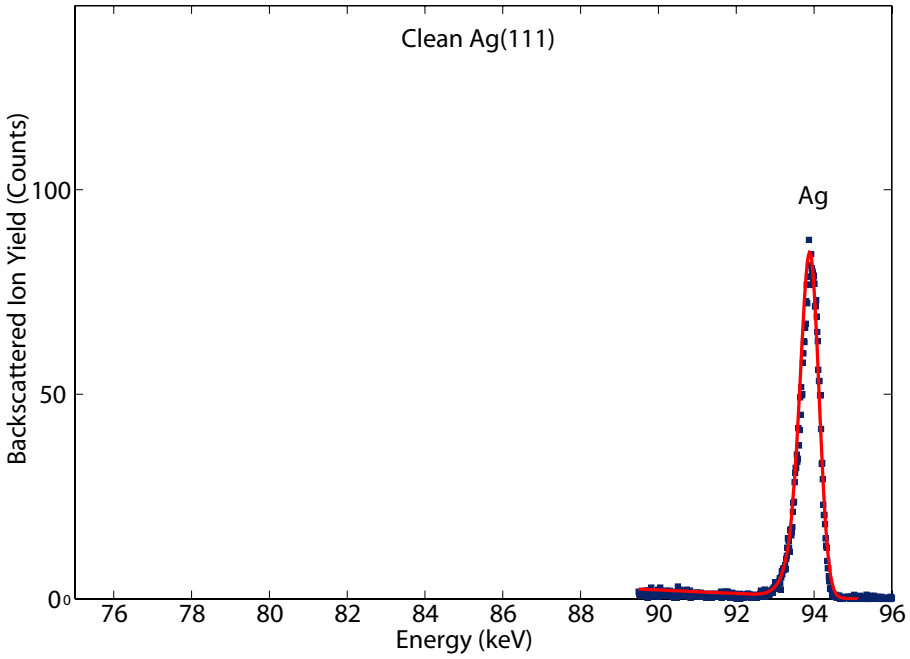

(a) Clean Ag(111).

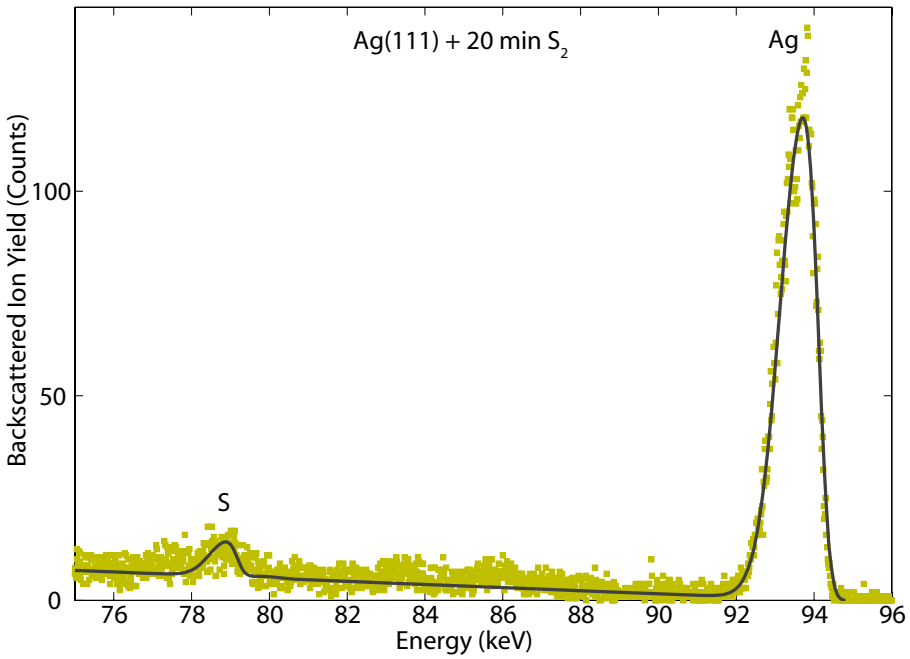

(b) 20 min dose of silver sulphide on Ag(111).

Figure 5.11: Plots showing simulation (solid line) and experimental data (data points) for energy cuts obtained from clean Ag(111) (Figure 5.11(a)) and a 20 minute dose of silver sulphide on Ag(111) (Figure 5.11(b)). Each energy cut is the projection of 3 channels from the $[\overline{1}\overline{1}0]$ incidence direction and $[21\overline{1}]$ outgoing direction with respect to the Ag(111) substrate.

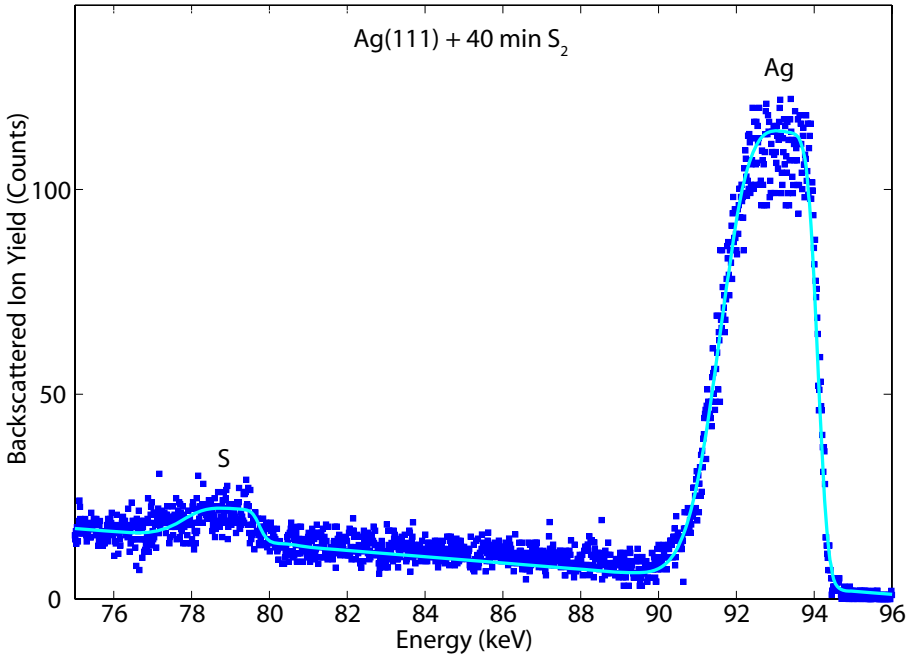

(a) 40 min dose of silver sulphide on Ag(111).

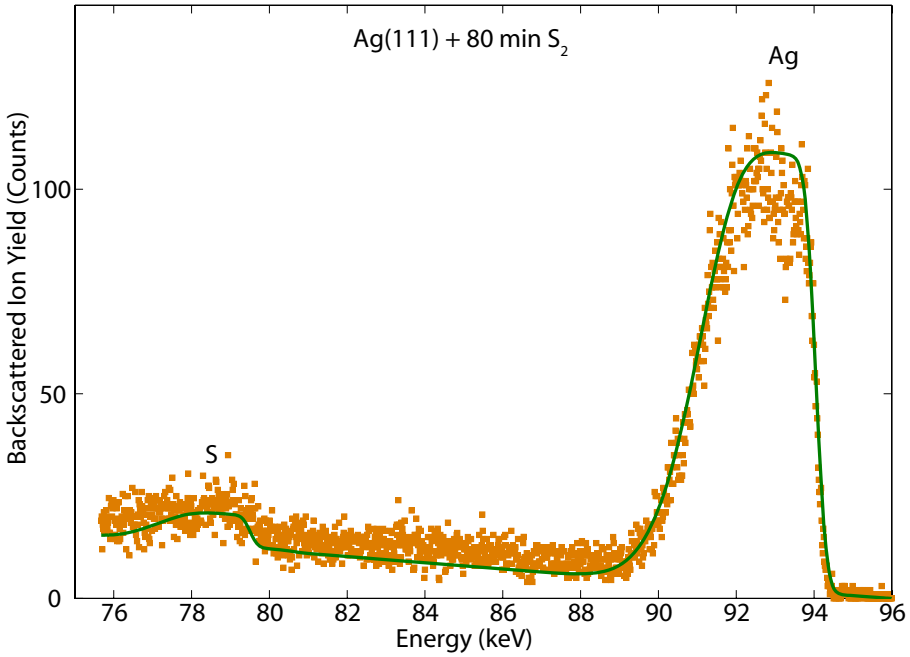

(b) 80 min dose of silver sulphide on Ag(111).

Figure 5.12: Plots showing simulation (solid line) and experimental data (data points) for energy cuts obtained from a 40 minute dose of silver sulphide on Ag(111) (Figure 5.11(a)) and an 80 minute dose of silver sulphide on Ag(111) (Figure 5.11(b)). Each energy cut is the projection of 3 channels from the $[\overline{1}10]$ incidence direction and $[21\overline{1}]$ outgoing direction with respect to the Ag(111) substrate.

The thicknesses of the films as determined via optimisation of the depth profiling simulations are given in Table 5.1, along with the thickness distribution of each of the films.

Film Preparation	Average thickness of Ag_2S layer, determined by energy cut simulation (Å)	FWHM of thickness distribution of Ag_2S layer, determined by energy cut simulation (Å)
20 min dose, Figure 5.11(b)	16.25	11.96
40 min dose, Figure 5.12(a)	36.19	30.00
80 min dose, Figure 5.12(b)	46.52	31.92

Table 5.1: Summary of the silver sulphide film thicknesses and distribution of thicknesses obtained through optimisation of the energy cuts using SIMNRA.

The data obtained are consistent with Ag_2S films with thickness increasing with further sulphur deposition. The data show thicknesses distributions indicative of rough films forming with a proportionally large range of thicknesses.

5.4.2 Surface Structure Analysis

In order to conduct a full structural analysis using MEIS, it is necessary for the surface atoms to lie in the same azimuth as the incidence direction, so that blocking features may arise from these atoms. For structural analysis of the $(\sqrt{7} \times \sqrt{7})R19.1°$ silver sulphide phase, the incidence direction $[\overline{1}12]$ in the Ag(111) substrate in the $\{1\overline{3}2\}$ azimuth, was identified as being in the same azimuth as the atoms in the proposed overlayer structure, see Figure 5.13. However, due to the strict limitations imposed on data acquisition by the severe beam-induced damage, it was not possible to obtain data for this incidence direction, which is a small channelling direction leading to more noise in the data. As a result of this, analysis of the surface structure would be restricted to showing consistency with the proposed surface model and would not be able to explicitly identify the structure.

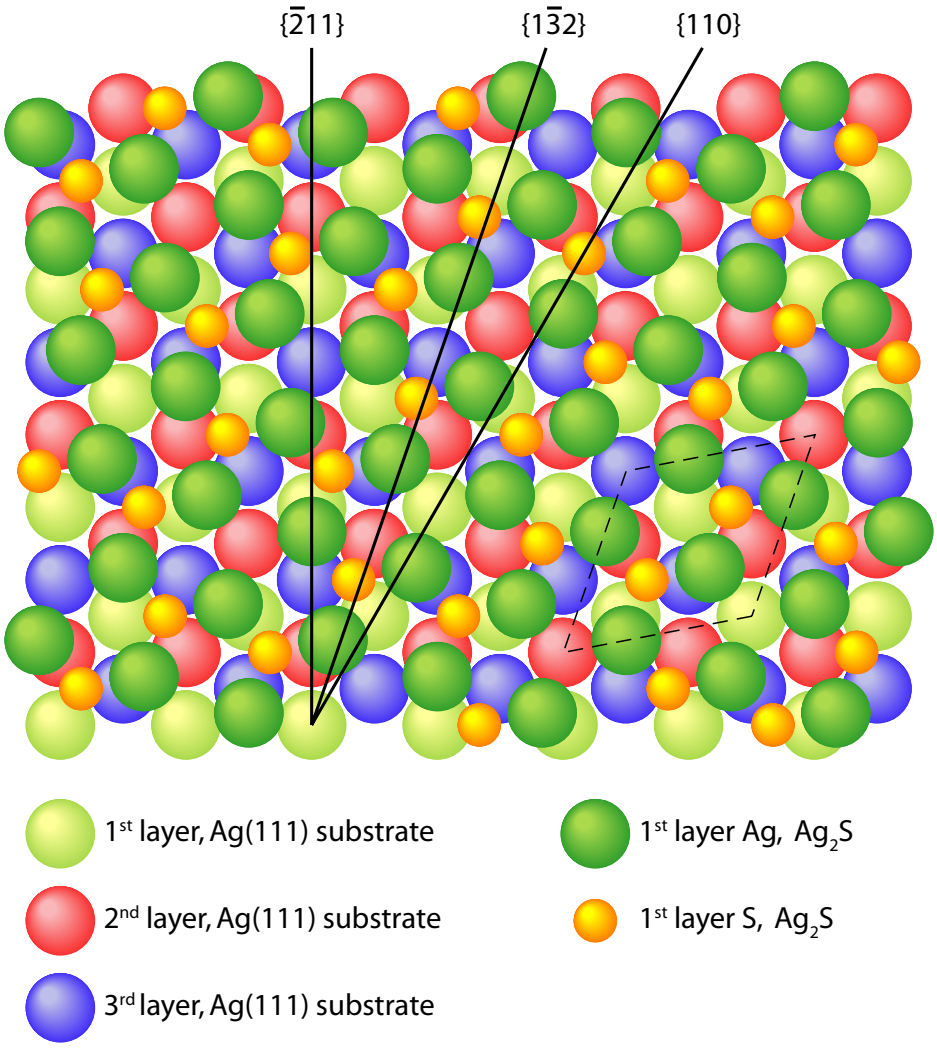

Figure 5.13: Plan view of the model of the Ag(111)($\sqrt{7} \times \sqrt{7}$)R19.1°−S, as proposed by Yu *et al.* [1]. The model shows three azimuthal planes for the Ag(111) substrate: the {110} azimuth and the {$\bar{2}$11} azimuth in which data were taken; and the {1$\bar{3}$2} azimuth, which is parallel to a plane in the proposed Ag(111)($\sqrt{7} \times \sqrt{7}$)R19.1°−S overlayer (one layer of which is shown). The light green atoms represent the first layer of silver atoms in the Ag(111) substrate, the red atoms represent the second layer of silver atoms in the Ag(111) substrate, the blue atoms represent the third layer of silver atoms in the Ag(111) substrate, the dark green atoms represent the silver atoms in the first layer of the silver sulphide film, and the small yellow atoms represent the first layer of sulphur atoms in the silver sulphide film.

5.4.2.1 Yield Calibration

The presence of a reconstruction of the silver atoms in the sulphide overlayer with respect to the clean surface should manifest itself as an increase in the backscattered ion yield in the blocking curve due to a greater number of silver atoms being illuminated by the ion beam. In order to successfully identify this yield change, the calibration of the absolute yields in terms of number of (111) layers of the undosed surface (Ag(111)) is critical. It is common in MEIS to use the undosed clean surface data (in this case Ag(111)) in order to establish a calibration factor, due to the relatively well known properties of a clean surface providing a good approximation to the number of visible layers. However, an independent additional source of calibration improves the accuracy of the determined absolute yields. This calibration was achieved using a crystalline Si(111) sample with a buried Cu layer of known concentration (known hereafter as the 'calibration sample'). The calibration sample, supplied by Rutgers University in the USA, contains shallowly implanted Cu atoms with a density of $3.12 \pm 0.09 \times 10^{15}$ atoms cm^{-2}, which has been established independently using conventional RBS. The sample was first aligned to the $[\overline{1}10]$ direction within the bulk of the crystalline Si. Data were then taken by rotating the crystal through $+7^{\circ}$ to 42.26° incidence, a region far from major channelling directions, in order to acquire data from a pseudo-random incidence direction. A pseudo-random incidence direction is essential in order to maximise the observed yield from the implanted Cu layer by minimising shadowing by the Si atoms. The calibration factor is a theoretical value for the number of counts per layer, which can be obtained by applying a correction to the number of counts obtained from the Cu after removing angular dependence of the Rutherford cross-section. The correction takes into account different cross-sections of the target atoms, the relative atomic density for the layers and the different incidence angles used, but assumes identical charge fractions between samples. The uncertainty of this method is $\sim \pm 5\%$ based upon the uncertainties in the value for the density of the Cu atoms obtained using RBS and day to day variations in the MEIS instrumentation.

5.4.2.2 Structural Analysis

Investigations into the surface structure, for the preparations that produced the $(\sqrt{7} \times \sqrt{7})R19.1^\circ$ LEED pattern, were conducted by building the proposed silver sulphide model and running simulations using the VEGAS code. Simulations were run for a number of different model thicknesses of the silver sulphide, which were deduced from the average thicknesses obtained during the depth profile study. The results of these simulations alongside the experimentally obtained data can be seen in Figure 5.14 (for the nominal one layer data) and Figure 5.15 (for the nominal two layer data). There is a clear difference in yield between each of the preparations, with the yield increasing with increasing sulphur deposition in agreement with the increasing thickness of silver sulphide established in the depth profile analysis. The experimental blocking curves do not appear to show any blocking features not apparent in the clean Ag(111) data. This is to be expected for a silver surface reconstruction in which the displaced atoms lie out of the azimuthal plane in which the incidence direction lies. This is consistent with the proposed model for the $(\sqrt{7} \times \sqrt{7})R19.1^\circ$ silver sulphide phase as evidenced by the VEGAS simulations.

The error in the absolute backscattered ion yield determined via use of the calibration sample is determined to be $\pm 5\%$. This yield is dependent on both the thickness of the silver sulphide film and the vibrational amplitudes of the silver atoms. These two parameters are coupled together such that a thinner film with a high vibrational amplitude could produce the same backscattered ion yield as a thicker film with a low vibrational amplitude. In order to produce the simulations, the thicknesses of the films were set originally to the thicknesses as obtained via the energy cut simulations, and with vibrational amplitudes of the silver atoms calculated using the Debye temperature (225 K). The thickness and vibrational amplitude were then optimised keeping the obtained values within relatively small bounds of the initial values, in order that the thickness did not deviate too far from that calculated via energy cut simulations and also to avoid the vibrational amplitude reaching an unphysical value.

Using this method, the vibrational amplitudes were determined to be 0.09 $Å^2$ for silver atoms in the bulk sulphide, and 0.13 $Å^2$ for silver atoms in the surface layer of the sulphide. The simulation for the 40 min dose required 20 silver layers, with the structure proposed by Yu *et al.* [1], in the silver sulphide overlayer to obtain a backscattered ion yield in comparison to the experimentally obtained data. This equates to an average silver sulphide thickness of 36.2 Å. The simulation for the 80 min dose required 24 silver layers, with the structure proposed by Yu *et al.* [1], in the silver sulphide overlayer to obtain a backscattered ion yield in comparison to the experimentally obtained data. This equates to an average silver sulphide thickness of 43.44 Å. The blocking curve for the low coverage complex phase obtained from a 20 min dose could not be directly simulated as no known structural model exists. The simulated blocking curve for this case is produced by translating the clean Ag(111) simulated blocking curve by an appropriate number of (111) layers. The increase in yield for this blocking curve was found to be equivalent to 3.2 (111) layers.

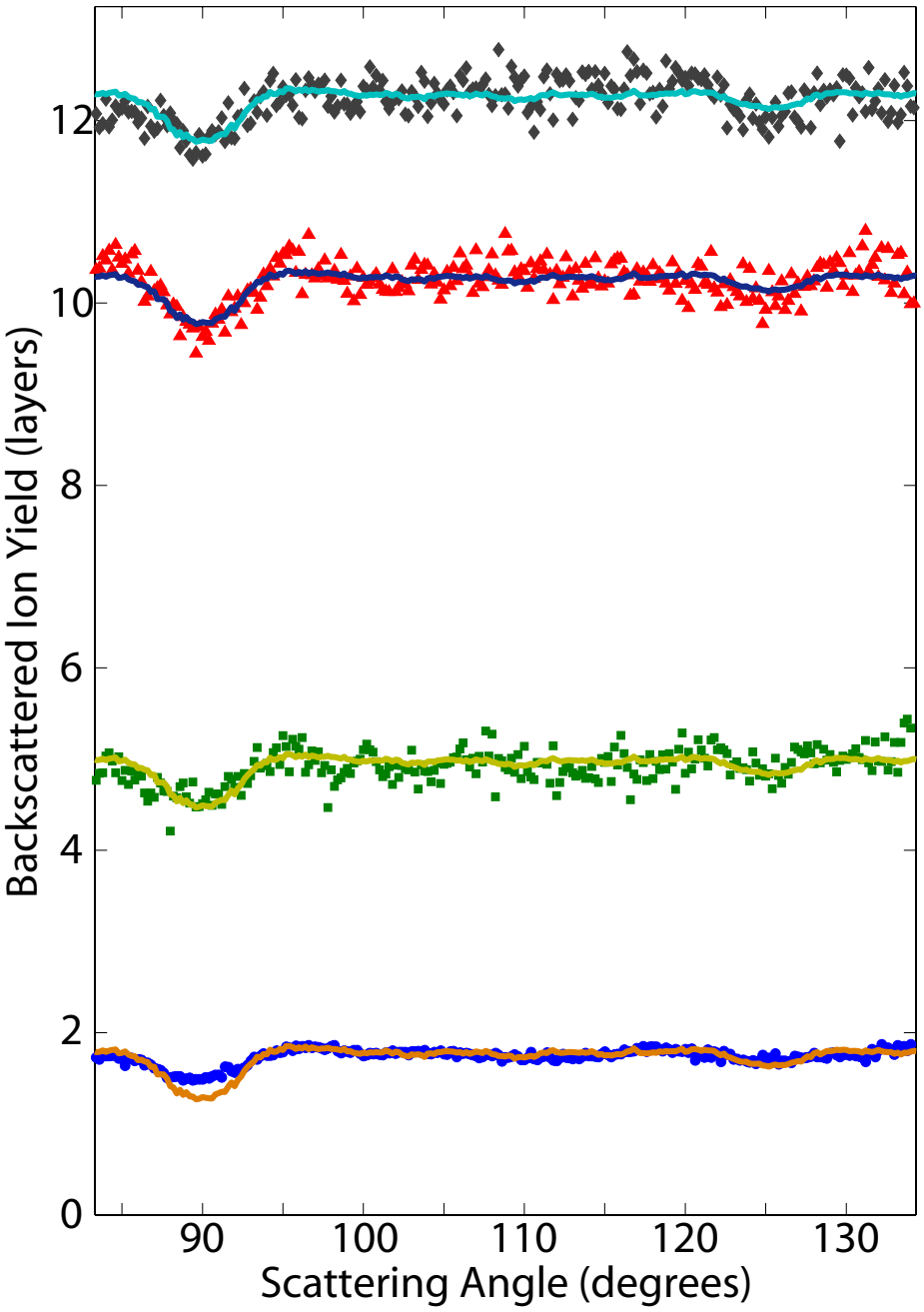

Figure 5.14: VEGAS simulations for the nominal one-layer illumination, $\langle \overline{1}10 \rangle$ incidence direction for clean Ag(111), and silver sulphide films of various thicknesses grown on Ag(111). The experimental data are represented as points and the simulations are represented by solid lines.

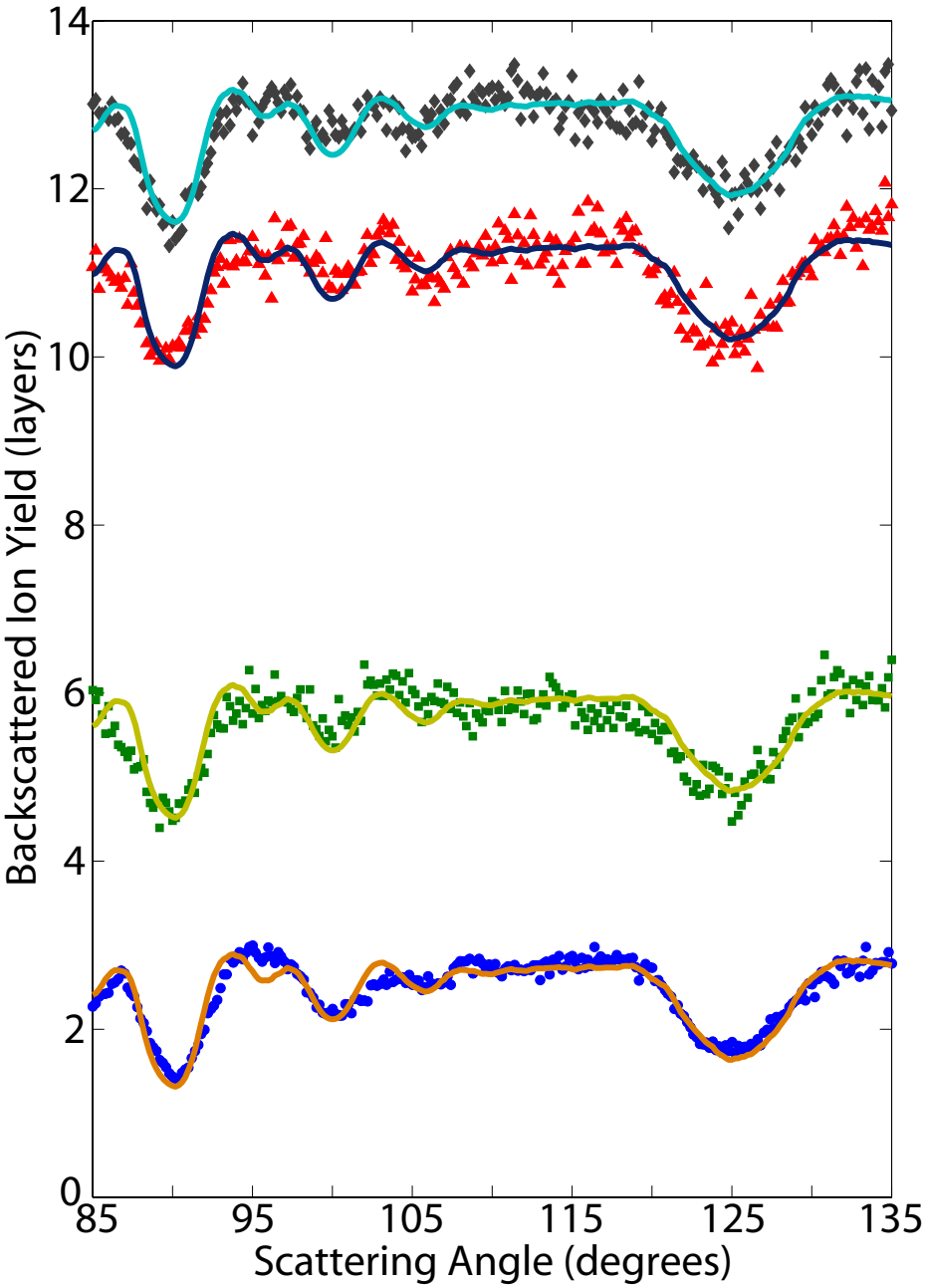

Figure 5.15: VEGAS simulations for the nominal two-layer illumination, $\langle\overline{211}\rangle$ incidence direction for clean Ag(111), and silver sulphide films of various thicknesses grown on Ag(111). The experimental data are represented as points and the simulations are represented by solid lines.

5.5 Conclusions

Ultrathin films of silver sulphide were prepared on an Ag(111) surface. Unusually, the silver sulphide suffered from severe beam-induced damage from an H^+ ion beam, believed to be as a result of a chemical reaction between hydrogen resulting from the H^+ beam and the sulphur in the surface. MEIS data acquisition was undertaken using an He^+ ion beam, however, the higher ion mass causes physical damage to the near surface region at a high rate and therefore doses on each crystal spot were kept low to avoid this beam-induced damage. This resulted in only a small number of data sets being obtained with a relatively large degree of noise in the data, limiting the information that could be deduced about the surface.

5.5.1 Depth Profiling Analysis

Silver sulphide films were prepared with a range of different deposition times, resulting in evidence of two different structural phases, a low coverage complex phase and a $(\sqrt{7} \times \sqrt{7})R19.1^\circ$ higher coverage phase. Simulations of energy cuts were compared to data obtained from these different preparations in order to evaluate the depth profile of the films.

The sulphur coverage did not saturate for the depositions studied because the silver sulphide films were found to continue to increase in thickness with increasing sulphur deposition, and were all found to have a stoichiometry consistent with Ag_2S. This demonstrated an epitaxial growth of a silver sulphide overlayer. The films were also found to have a large distribution of thicknesses indicative of the formation of rough films.

5.5.2 Structural Analysis

Simulations were run on the proposed silver sulphide model for thicknesses obtained using depth profiling analysis. The simulations were fitted to the experimentally obtained blocking curves for the silver surface peak, both of which showed a large

yield change consistent with a reconstruction of the silver atoms with respect to the Ag(111). The blocking curves did not yield any new blocking features in comparison to the clean Ag(111) surface, consistent with the reconstructed silver atoms of the sulphide overlayer lying in positions out of the azimuthal plane in which the data were acquired. In order to conduct a more thorough structural analysis on this surface it would be necessary to obtain data with an incidence direction for the Ag(111) substrate of $\langle\bar{1}12\rangle$. Any further data acquisition would require a great deal of care in order to avoid the beam-induced damage effects and obtain data with high enough statistics to observe subtle changes in the blocking curves obtained from the clean Ag(111) and Ag_2S/Ag(111) surfaces.

Chapter 6

$p2gg(4 \times 2)$Mn/Cu(100) Films Grown on Cu(100)

6.1 Introduction

The study of surface alloy formation has gained increasing interest in recent years. Alloying at the surface of a substrate should strongly influence the physical properties of the surface. These changes could prove either beneficial or detrimental depending on the surface. The major benefit of alloying is in the potential for tailoring of catalytic properties of the surface alloy formed, whilst detrimental effects are brought about through changes to magnetic or electronic properties of magnetic thin films or semiconductor heterostructures due to alloy formation. In order to elucidate these effects, the most recent studies concentrate on surface structural determination of these alloys.

For a large number of these alloys, formed by depositing metal adsorbates onto a single metal substrate, it is found that the adsorbate occupies substitutional sites in the outermost atomic layers of the substrate. Commonly, these alloy systems involve adsorbate atoms with atomic radii that are larger than the substrate atoms. The presence of the larger atoms typically gives rise to buckling of the surface layer.

The deposition of Mn on Cu(100) forms one such alloy - a prototype surface alloy with several different structural phases existant depending on the growth conditions. These various long-range-ordered superstructures have been observed and investigated using LEED [91]. The formation of the surface alloy is believed to come about through direct Mn−Cu atomic exchange with a resultant atomic buckling of the surface layers because of the larger atomic radius of manganese compared to copper.

6.2 Previous work

The simplest phase formed from deposition of Mn on Cu(100) is the $c(2 \times 2)$ phase. Due to the relative simplicity in forming this phase, there have been several studies conducted using a wide variety of techniques: DFT [92], STM [93, 94], XPS [95], UPS [95, 96], MEIS [34], scanned energy mode PhD [97], LEED (quantitative and qualitative) [96, 98, 99] and AES [96, 100]. These have provided information on the growth, structural, electronic and magnetic properties of the $c(2 \times 2)$ phase.

The $p2gg(4\times2)$ phase has been investigated much less widely, with just a few studies existing. The first of these, by Flores *et al.* [91] used AES, LEED and medium energy electron diffraction (MEED) to examine this phase, which was identified as a $p2mg(4 \times 2)$ phase based upon the LEED pattern obtained. The Auger intensity ratio of the copper transition at 60 eV and the manganese transition at 40 eV was interpreted as showing that this metastable alloy phase consists of at least two ordered alloy layers.

A study by van der Kraan *et al.* [100] used LEED, AES and STM to examine this phase. This study relabelled the alloy as a $p2gg(4 \times 2)$Mn/Cu(100), based upon the lack of a mirror plane in the obtained STM images. This phase has a similar LEED pattern to the $p2mg(4 \times 2)$ phase proposed previously by Flores *et al.* [91]. A LEED investigation into the structure of the second layer of the alloy

was conducted, suggesting this structure could be either a $c(2 \times 2)$ or a mirrored pgg structure. The STM was unable to distinguish between these two possibilities, however, the study concluded that the $c(2 \times 2)$ phase was the most likely based on the fact that this phase is formed for lower coverages of the alloy. The STM images also identified a large corrugation in both the $p2gg(4 \times 2)$ and $c(2 \times 2)$ structural phases. It was not possible to determine whether these corrugations were as a result of atomic buckling or due to density of state (DOS) effects. It was therefore suggested that further investigations would be necessary looking at local DOS calculations and magnetic properties, as well as using a technique capable of performing a full structural determination, suggesting that full dynamical LEED, SEXAFS or ion scattering investigations could be appropriate.

Pan *et al.* [101] combined highly sensitive surface stress change measurements with SXRD structure determination. This was used to propose a refined structural model, see Figure 6.1. This model included considerable atomic buckling, which had been proposed by van der Kraan *et al.* [100] based upon STM images. Attempts were made to identify the concentrations of Mn and Cu in the first two layers, with $> 50\%$ Mn in the top layer and $< 50\%$ Mn in the second layer preferred. A schematic model for the MnCu surface alloy formation was proposed based upon the results of the investigation.

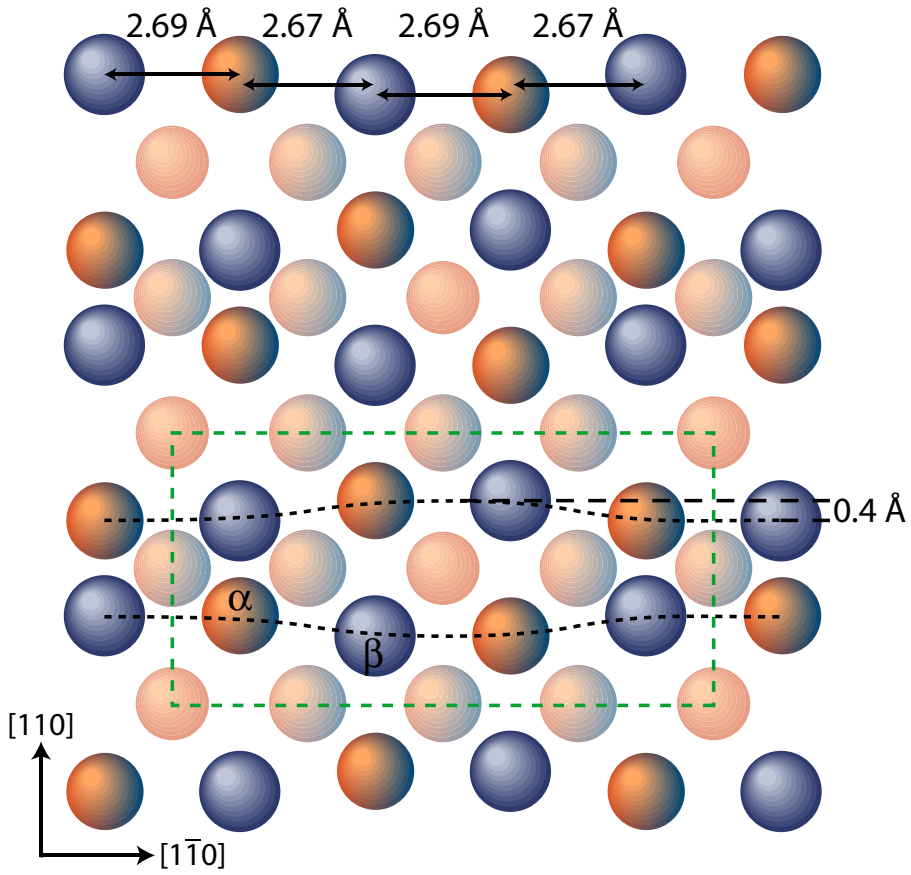

Figure 6.1: Plan view of the top two layers of the model of the $p2gg(4 \times 2)$Mn/Cu(100) surface, as proposed by Pan *et al.* [101]. The orange atoms represent the copper, the dark blue atoms represent the manganese, atoms that are partially blue and partially orange could be either copper or manganese. The dashed green box represents the (4×2) unit cell. The top layer consists of atoms close to bulk-terminated positions $(1/8, 1/4)$, labelled α, and $(3/8, 1/4)$, labelled β within the surface unit cell. These atoms undergo small lateral shifts in each direction.

6.3 Experimental Method

6.3.1 Preparation

The single crystal metal Cu(100) substrate was cleaned by cycles of cold sputtering and annealing, see section 3.2.6, with annealing to temperatures of 700 °C. After several such cycles, the crystal had no peaks attributable to contamination in the AES spectra, therefore it was judged to be clean, and had a sharp well-ordered (1×1) LEED pattern down to 56 eV.

The surface alloy was prepared by depositing manganese onto the clean Cu(100) surface, which was held at 100 °C for the duration of the deposition. Manganese deposition was conducted using an Oxford Instruments Knudsen cell (known as a 'K-cell'). The K-cell contains a crucible containing solid manganese, heating filaments, heat shields, a water cooling system and a shutter. The temperature of the K-cell is kept very stable by a controller, which adjusts precisely the power input required to achieve the selected temperature. The result of this is that the K-cell produces a stable, reproducible evaporation rate. The K-cell was operated at a temperature of 900 °C. The LEED pattern and Auger spectrum were examined at regular intervals throughout the deposition process to ensure no contaminants were appearing on the surface and that the expected phase was being produced. Several different deposition times were tested, and it was found that deposition times in the range $5 - 20$ mins yielded a $p2gg(4 \times 2)$Mn/Cu(100) LEED pattern, whilst shorter deposition times were found to yield the $c(2 \times 2)$ LEED pattern.

6.3.2 Characterisation

After deposition, the sample yielded a $p2gg(4 \times 2)$ LEED pattern relative to that of the clean (1×1) metal substrate at 56 eV, as required for the phase under investigation, see Figure 6.2. The Auger spectrum showed peaks only attributable to copper and manganese, see Figure 6.3 for an example spectrum.

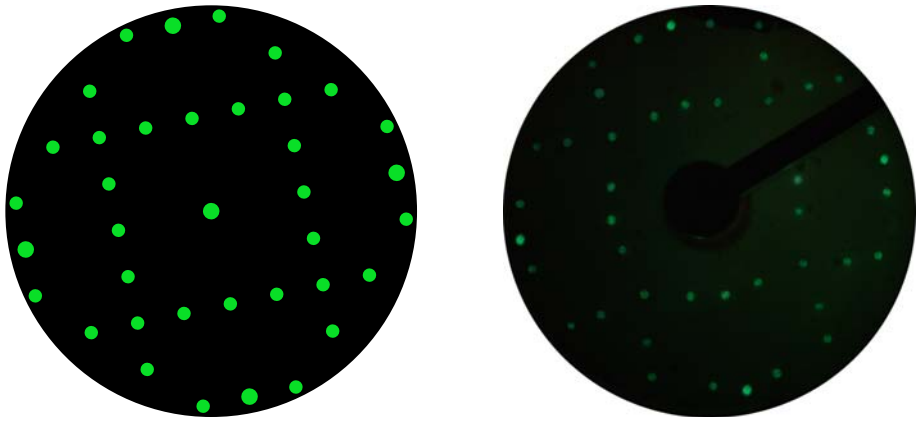

(a) Theoretical $p2gg(4 \times 2)$ LEED pattern relative to that of the metal substrate.

(b) LEED pattern obtained at 56 eV after copper manganese sample preparation, confirming $p2gg(4 \times 2)$ LEED pattern relative to that of the metal substrate.

Figure 6.2: Figure showing comparison between theoretical LEED pattern and experimentally obtained LEED pattern relative to that of the metal substrate, at 56 eV. Figure (a) shows the theoretical pattern, Figure (b) shows the experimentally obtained LEED pattern confirming the presence of a $p2gg(4 \times 2)$ LEED pattern.

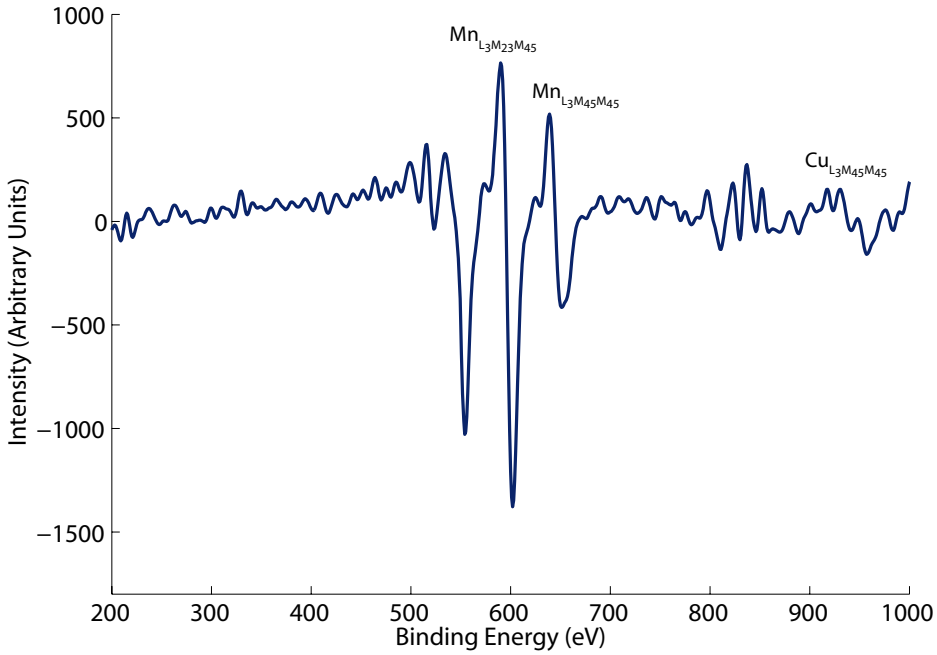

Figure 6.3: An example Auger spectrum of copper manganese obtained from a film that showed the LEED pattern of the $p2gg(4 \times 2)$Mn/Cu(100) phase.

6.3.3 Measurements

The data were taken using an 100 keV He^+ ion beam, with the intention to obtain energy separation between the two surface peaks, which would not be possible with the more standard 100 keV H^+ ion beam due to the similar masses of copper and manganese. See Section 2.2.1 and, in particular, Figure **??** for more details. It is interesting to note that, despite the lack of energy separation between the copper and manganese surface peaks, the MEIS study of the simpler $c(2 \times 2)$Mn/Cu(100) phase [34] was conducted using an H^+ ion beam. This study integrated the entire unresolved surface peaks of copper and manganese before analysing a blocking curve including both species. It is likely that in this case the H^+ ion beam was used because of the lower risk of beam-induced damage to the surface. It is not possible to apply a similar technique of integrating the unresolved copper and manganese surface peaks for the more complex, $p2gg(4 \times 2)$Mn/Cu(100) phase, because one of the critical questions is the concentration of manganese in the first two layers, which could only be answered if the blocking curves are analysed independently.

MEIS data were taken using an 100 keV He^+ ion beam with a dose of 0.25 μC per tile, and with no area of the surface exposed to more than 1 μC, this low dose was chosen because beam-induced damage is known to occur at a relatively rapid rate for the relatively heavy He^+ ions. Four data sets were taken for each preparation in order to obtain a cumulative dose per tile of 1 μC to improve statistics.

Data were taken in incidence geometries aligned along crystallographic directions within the Cu(100) substrate. These data were taken along a nominal one layer illumination of the substrate, namely the $[\overline{211}]$ incidence direction in the {011} azimuth, see Figure 6.4 for a side view of the crystal for this plane, along with the major blocking directions. Data were taken for scattering angles in the range of $83° - 134°$.

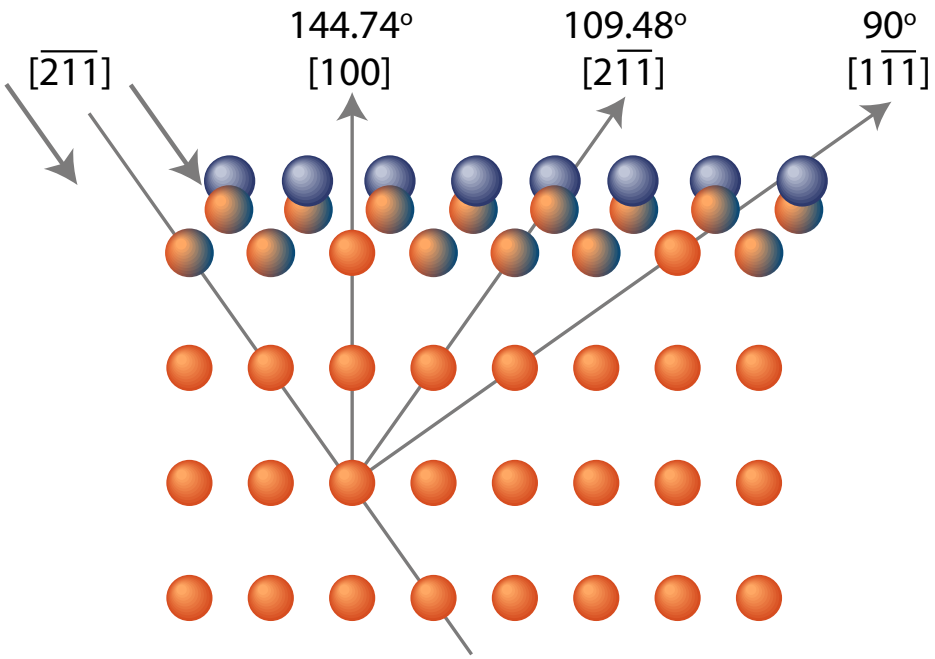

Figure 6.4: Side view of the $p2gg(4 \times 2)$Mn/Cu(100) phase. The figure shows a cross-section along the {011} azimuth. The orange atoms represent the copper, the dark blue atoms represent the manganese, atoms that are partially blue and partially orange could be either copper or manganese.

6.4 Results and Discussion

6.4.1 Depth Profile Information

During acquisition of the MEIS data, it became immediately apparent that the prepared surfaces contained significantly more manganese than the two layers expected from the previous work, and that the prepared surface contained a large amount of disordered material. As a result of this the manganese surface peak was exceptionally broad and was therefore unresolvable from the majority of the copper surface peak.

Despite several different preparation attempts, excessive amounts of disordered manganese were always observed in the MEIS data for preparations yielding the LEED pattern for the $p2gg(4 \times 2)$Mn/Cu(100) phase. Preparations with deposition

times for the manganese of < 5 mins were found to yield the LEED pattern for the $c(2 \times 2)$Mn/Cu(100) phase. As a result of this, it was not possible to yield any structural information on the $p2gg(4 \times 2)$Mn/Cu(100) surface, and instead only a brief depth profile analysis was conducted.

Figure 6.5 shows the experimental results from two of the prepared copper manganese films, along with simple simulations of the depth profiles using simulation software, written by P. D. Quinn [75] (described in more detail in section 4.4.1). Figure 6.5(a) gives the results obtained by deposition of manganese for a length of 5 minutes, whilst Figure 6.5(b) gives the results obtained by deposition of manganese for a length of 10 minutes. Both preparations yielded the $p2gg(4 \times 2)$Mn/Cu(100) LEED pattern.

Both plots show a small surface peak at ~ 89 keV, attributable to surface copper. This peak arises from a very small magnitude of copper in the surface layer. Behind this, at lower energy, lies a broad peak attributable in the most part to disordered manganese, although a contribution from the subsurface copper must also be present. However, the peak is unresolvable and therefore the precise concentrations of the two different elements is unclear. Due to the presence of a LEED pattern, the disordered material cannot cover the entire surface and therefore the most likely explanation of the energy cuts are that small regions of the $p2gg(4 \times 2)$Mn/Cu(100) phase are present, which give rise to the copper surface peak. Other areas of the surface appear to be covered with disordered manganese. After the longer dose of manganese, the magnitude of the regions of $p2gg(4 \times 2)$Mn/Cu(100) phase appear to have decreased because the magnitude of the copper surface peak has also decreased. These observations were used to create initial models for the depth profile, which were the sum of regions of copper manganese alloy and regions of disordered manganese each lying above a Cu(100) substrate. The models were then optimised using the depth profiling simulation software, to establish the average thickness of the disordered manganese layer and the quantity of copper visible within

the $p2gg(4 \times 2)$Mn/Cu(100) regions.

The simulations showed that for the 5 min manganese deposition, the distinct copper peak at $\sim$ 89 keV resulted from 0.16 ML of copper in the surface layer, whilst for the 10 min manganese deposition, the magnitude of copper in the distinct peak at $\sim$ 89 keV had decreased slightly to 0.12 ML. The thickness of the unresolved peak for the 5 min manganese deposition was found to be $\sim$ 25 Å, and for the 10 min manganese deposition the thickness was found to be $\sim$ 49 Å.

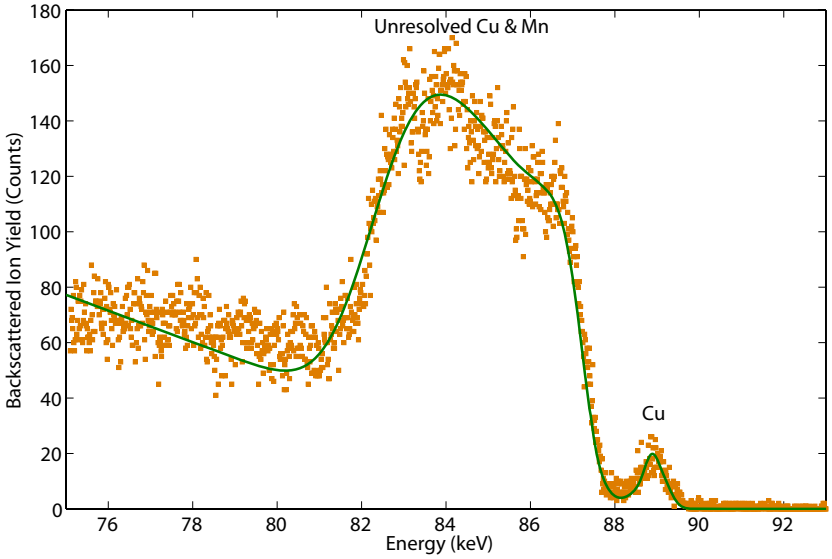

(a) 5 min deposition of manganese onto Cu(100).

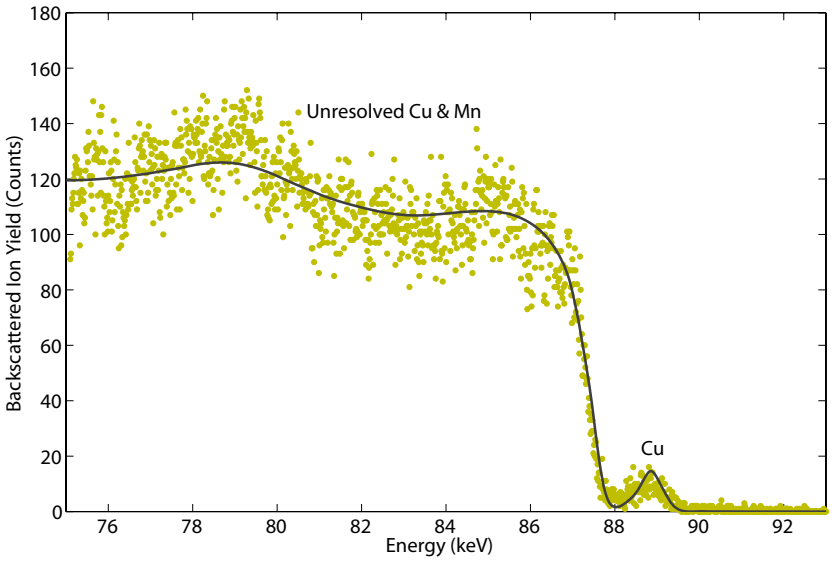

(b) 10 min deposition of manganese onto Cu(100).

Figure 6.5: Plots showing simulation (solid line) and experimental data (data points) for energy cuts obtained from two different preparations of copper manganese films. Figure 6.5(a) shows the results from a 5 min deposition of manganese, and Figure 6.5(b) shows the results from a 10 minute deposition of manganese onto Cu(100). Each energy cut is the projection of 3 channels from the $[\overline{2}11]$ incidence direction and $[\overline{111}]$ outgoing direction with respect to the Cu(100) substrate.

6.5 Conclusions

Ultrathin films of copper manganese were prepared on a Cu(100) surface, each of which yielded a $p2gg(4 \times 2)$Mn/Cu(100) LEED pattern. Data acquisition was undertaken using an He^+ ion beam, in an attempt to obtain sufficient energy resolution between the two elements, copper and manganese, which have similar masses. However, despite numerous attempts at sample preparation, all of the experimental data were found to contain amounts of manganese greatly in excess of the two layers predicted by previous studies. The thickness of the manganese layer precluded resolution of the copper and manganese surface peaks and therefore detailed structural analysis. The films were found to contain a small quantity of copper in the surface layer (< 0.16 ML), and a thick disordered layer (~ 25 Å thick for a 5 min manganese deposition, ~ 49 Å thick for a 10 min manganese deposition). Any peak arising from subsurface copper could not be distinguished from manganese in this layer.

Chapter 7

Conclusions

MEIS has been used for the purpose of this study of ultrathin epitaxial film systems. The versatility of the technique has been demonstrated with information being yielded on both surface structure and depth profiles of the films.

For the $V_2O_3(0001)$ films, depth profiling information was used to investigate the quality of the films when grown on two different substrates, Pd(111) and Au(111), under different growth conditions. Films grown on Pd(111) were found to have a much greater distribution of thicknesses than those grown on Au(111). It was also found that thin films grown on Au(111), using a method of multiple short doses, grew in islands with bare patches of gold remaining visible. The best quality films grown were thick films grown on Au(111), which were found to be relatively uniform, with a high degree of crystallinity. These films yielded good blocking curves, which were used for analysis of the surface structure.

Investigations of the surface structure of $V_2O_3(0001)$ found that the optimal fit of simulation to experimental blocking curves came from an oxygen termination, first proposed in a DFT study by Kresse *et al.* [57]. There is no known published quantitative experimental work on this structure, so it would be necessary to fully determine how this model fits in with data obtained using other techniques to establish the viability of this structure. PhD data on the $V_2O_3(0001)$ surface

has been re-examined by Unterberger [77] and it was found that PhD simulations obtained from this structure are compatible with the experimental PhD data. An STM study [70] has been interpreted as showing the coexistence of a vanadyl termination and an oxygen termination. With this possibility positively reinforced by this MEIS study, future investigations using MEIS could explore how different concentrations of the two potential terminations for the $V_2O_3(0001)$ surface affect the simulated MEIS blocking curves.

For the $Ag_2S/Ag(111)$ films, beam-induced damage was found to be a major limitation of the MEIS technique. Typically, despite the transfer of energy from ion to surface during data acquisition, the MEIS technique is considered non-destructive at the doses used. However, in the case of the silver sulphide films, extreme beam-induced damage occurred during data acquisition with an H^+ ion beam, which is believed to be as a result of an unusual chemical reaction between hydrogen originating from the beam and the sulphur in the surface. The heavier He^+ ion was used for data acquisition, however the greater transfer of energy due to the higher mass of the ion causes physical damage to the surface at an increased rate compared to the H^+ ions normally used to obtain structural information. To avoid any potential beam-induced damage, data were taken at a very low dose, limiting the information that could be obtained on the system.

Using MEIS as a depth profiling tool, the sulphur coverage was found not to saturate for the depositions studied. The evidence for this is that the silver sulphide films continue to increase in thickness with increasing sulphur deposition, and were all found to have a stoichiometry consistent with Ag_2S. This demonstrated an epitaxial growth of a silver sulphide overlayer. The films were also found to have a large distribution of thicknesses indicative of the formation of rough films. Analysis of the blocking curves obtained from each of these films found that a $(\sqrt{7} \times \sqrt{7})R19.1°$ structure, proposed by Yu *et al.* [1], produced consistent blocking curves. However, this does not preclude other possible structures. In order to conduct further

structural analysis of the $(\sqrt{7} \times \sqrt{7})R19.1^\circ$ silver sulphide phase using MEIS, data should be acquired along the incidence direction, $[\overline{1}12]$ in the Ag(111) substrate, in the $\{1\overline{3}2\}$ azimuth, which has been identified as being in the same azimuth as the atoms in the proposed overlayer structure. This will require a great deal of care in order to avoid the beam-induced damage effects.

In the case of the Ag_2S/Ag(111) films, the absolute yield of the blocking curves is critical. One of the major contributory factors in establishing simulated yields for MEIS blocking curves is the magnitude used for the thermal vibrations of the atoms. In order to reduce the potential impact of thermal vibrations in MEIS data, during 2009 the UK MEIS facility at Daresbury developed and installed a system compatible with sample transfer and capable of cooling samples in the experimental chamber. This cooling could be used in future MEIS experiments to improve the quality of blocking curves obtained. However, in the case of the ultrathin epitaxial films studied in this thesis, significant cooling may not be possible because of the existence of different phases for the films at low temperatures.

For the *p2gg*($\mathbf{4} \times \mathbf{2}$)Mn/Cu(100) films, the lack of intrinsic surface sensitivity in MEIS, used to yield information in the previous two systems of the thesis, proved to be detrimental. It was not possible to resolve the surface structure and as a result, only a small amount of information could be gleaned. For the films grown, a small amount of copper was found to be present within regions of a p2gg(4×2) phase, which gave rise to an appropriate LEED pattern, but with large regions of disordered manganese also observed. The precise quantities of manganese and copper could not be determined due to the existence of a broad unresolvable peak.

MEIS is a powerful technique capable of providing important contributions to the understanding of complex surface science systems. The lack of intrinsic surface sensitivity, often used to its advantage has also proved to be a weakness. Despite this, MEIS complements well the information gained by other surface science techniques.

Bibliography

[1] Miao Yu, D. P. Woodruff, Christopher J. Satterley, Robert G. Jones, and V. R. Dhanak. Structural Investigation of the Interaction of Molecular Sulphur with Ag(111). *Journal of Physical Chemistry C*, 111(7):3152–3162, 2007.

[2] D. P. Woodruff and T. A. Delchar. *Modern Techniques of Surface Science*. Cambridge University Press, second edition, 1994.

[3] M. Aono. Quantitative Surface Structure Analysis by Low-Energy Ion Scattering. *Nuclear Instruments and Methods in Physics Research B: Beam Interactions with Materials and Atoms*, 2:374–383, 1984.

[4] Horst Niehus, Werner Heiland, and Edmund Taglauer. Low-energy ion scattering at surfaces. *Surface Science Reports*, 17:213–303, 1993.

[5] S. Rubin. Surface analysis by charged particle spectroscopy. *Nuclear Instruments and Methods*, 5:177–183, 1959.

[6] D P Smith. Scattering of low-energy noble gas ions from metal surfaces. *Journal of Applied Physics*, 38(1):340–347, 1967.

[7] D P Smith. Analysis of surface composition with low-energy backscattered ions. *Surface Science*, 25:171–191, 1971.

[8] W. C. Turkenburg, W. Soszka, F. W. Saris, H. H. Kersten, and B. G. Colenbrander. Surface structure analysis by means of Rutherford scattering: Methods to study surface relaxation. *Nuclear Instruments and Methods*, 132:587–602, 1976.

[9] W. C. Turkenburg, H. H. Kersten, B. G. Colenbrander, A. P. de Jongh, and F. W. Saris. Experimental parameters for quantitative surface analysis by medium energy ion scattering. *Nuclear Instruments and Methods*, 138:271–286, 1976.

[10] H. Goldstein. *Classical Mechanics*. Addison-Wesley, 2002.

[11] E. Rutherford. The scattering of α and β particles by matter and the structure of the atom. *Philosophical Magazine*, 6(21), May 1911.

[12] J.F. Van der Veen. Ion Beam Crystallography of Surfaces and Interfaces. *Surface Science Reports*, 5:199–288, 1985.

[13] G. Z. Molière. Theorie der Streuung schneller geladener Teilchen. I. Einzelstreuung am abgeschirmten Coulomb-Field. *Z. Naturforsch*, 2a:133–145, 1947.

[14] O. B. Firsov. Calculation of the interaction potential of atoms. *Journal of Experimental and Theoretical Physics*, 6:534, 1958.

[15] J. F. Ziegler, J. P. Biersack, and U. Littmark. *The stopping and range of ions in solids*. Pergamon Press, 1985.

[16] J. L'Ecuyer and J. A. Davies and N. Matsunami. How accurate are absolute Rutherford backscattering yields. *Nuclear Instruments and Methods*, 160:337–346, 1979.

[17] H. H. Andersen and F. Besenbacher and P. Loftager and W. Möller. Large-angle scattering of light ions in the weakly screened Rutherford region. *Physical Review A*, 21(6):1891–1901, June 1980.

[18] S. R. Lee and R. R. Hart. Screened Rutherford backscattering cross sections for heavy ion and low energy backscattering analysis. *Nuclear Instruments and Methods in Physics Research B: Beam Interactions with Materials and Atoms*, 79:463–467, 1993.

[19] James F. Ziegler. www.srim.org.

[20] N. Bohr. The penetration of atomic particles through matter. *Kgl Danske Videnskab.Seskab Mat-Fys Medd*, 18(8):1 – 144, 1948.

[21] W. K. Chu. Calculation of energy straggling for protons and helium ions. *Physical Review A*, 13(6):2057–2060, 1976.

[22] Q. Yang and D. J. O'Connor and Zhonglie Wang. Empirical formulae for energy loss straggling of ions in matter. *Nuclear Instruments and Methods in Physics Research B: Beam Interactions with Materials and Atoms*, 61:149–155, 1991.

[23] Yoshiaki Kido and Takanori Koshikawa. Ion Scattering Analysis Programs for Studying Surface and Interface Structures. *Journal of Applied Physics*, 67(1):187–193, January 1990.

[24] J. B. Marion and F. C. North. *Nuclear reaction analysis graphs and tables*. North Holland Amsterdam, 1968.

[25] I. Stensgaard, L. C. Feldman, and P. J. Silverman. Calculation of the Backscattering-Channeling Surface Peak. *Surface Science*, 77:513 – 522, 1978.

[26] Ordean S. Oen. Universal Shadow Cone Expressions for an Atom in an Ion Beam. *Surface Science*, 131:L407–L411, 1983.

[27] Paul D. Quinn. XVegas MEIS Simulation Software. *Version 132*, 2005.

[28] John H. Barrett. Monte Carlo Channeling Calculations. *Physical Review B*, 3(5):1527–1547, 1971.

[29] J. Lindhard. Influence of crystal lattice on motion of energetic charged particles. *Kgl. Danske Videnskab Selskab Mat-fys Medd*, 34(14):64, 1965.

[30] R. M. Tromp and J. F. Van der Veen. Monte Carlo Simulations of Shadowing/Blocking Experiments for Surface Structure Analysis. *Surface Science*, 133:159–170, 1983.

[31] J. W. M. Frenken, R. M. Tromp, and J. F. Van der Veen. Theory and Simulations of High-Energy Ion Scattering Experiments for Structure Analysis of Surfaces and Interfaces. *Nuclear Instruments and Methods in Physics Research B: Beam Interactions with Materials and Atoms*, 17:334–343, 1986.

[32] D. P. Woodruff, D. Brown, P. D. Quinn, T. C. Q. Noakes, and P. Bailey. Structure determination of surface adsorption and surface alloy phases using medium energy ion scattering. *Nuclear Instruments and Methods in Physics Research B: Beam Interactions with Materials and Atoms*, 183:128–139, 2001.

[33] T. C. Q. Noakes, P. Bailey, and D. P. Woodruff. MEIS surface structure determination methodology: Application to Ni(100) $c(2 \times 2)$ - O. *Nuclear Instruments and Methods in Physics Research B: Beam Interactions with Materials and Atoms*, 136-138:1125–1130, 1998.

[34] D. Brown, T. C. Q. Noakes, D. P. Woodruff, P. Bailey, and Y. Le Goaziou. Structure determination of the Cu(100)$c(2 \times 2)$Mn and Cu(100)$c(2 \times 2)$Au surface alloy phases by medium-energy ion scattering. *Journal of Physics: Condensed Matter*, 11:1889–1901, 1999.

[35] Philip R. Bevington and D. Keith Robinson. *Data Reduction and Error Analysis for the Physical Sciences*. McGraw-Hill Higher Education, third edition, 2003.

[36] C. Davisson and L. H. Germer. Diffraction of electrons by a crystal of nickel. *The Physical Review*, 30(6):705–741, December 1927.

[37] J. B. Pendry. *Low Energy Electron Diffraction: The Theory and its Application to Determination of Surface Structure*. Techniques of Physics. Academic Press, 1974.

[38] Klaus Heinz. LEED and DLEED as modern tools for quantitative surface structure determination. *Reports on Progress in Physics*, 58:637–704, 1995.

[39] Hiroyuki Tawara. Some characteristics of a duoplasmatron ion source. *Japanese Journal of Applied Physics*, 3(6):342 – 346, June 1964.

[40] F. Naab and L.O. Lamm and W. Zech and A. Garcìa and P. Mumm. A zero-to-few-hundred eV proton beam for calibrations of neutron β decay experiments. *Nuclear Instruments and Methods in Physics Research B: Beam Interactions with Materials and Atoms*, (197):278281, 2002.

[41] S. K. Guhuray, J. Orloff, and M. Wada. Ion Beams and Their Applications in High-Resolution Probe Formation. *IEEE Transactions on Plasma Science*, 33(6):1911 – 1930, December 2005.

[42] R. G. Smeenk, R. M. Tromp, H. H. Kersten, A. J. H. Boerboom, and F. W. Saris. Angle Resolved Detection of Charged Particles with a Novel Type Toroidal Electrostatic Analyser. *Nuclear Instruments and Methods*, 195:581–586, 1982.

[43] H. A. Van Hoof and M. J. Van der Wiel. Position-sensitive detector system for angle-resolved electron spectroscopy with a cylindrical mirror analyser. *Journal of Physics E: Scientific Instruments*, 13(4):409–414, April 1980.

[44] J. McPherson W. B. Colson and F. T. King. High-gain imaging electron multiplier. *Review of Scientific Instruments*, 44(12):1694–1696, 1973.

[45] Joseph Ladislas Wiza. Microchannel plate detectors. *Nuclear Instruments and Methods*, 162:587–601, 1979.

[46] R. M. Tromp, M. Copel, M. C. Reuter, M. Horn von Hoegen, J. Speidell, and R. Koudijs. A New Two-Dimensional Particle Detector for a Toroidal Electrostatic Analyzer. *Review of Scientific Instruments*, 62(11):2679–2683, November 1991.

[47] J. Mendialdua, R. Casanova, and Y. Barbaux. XPS studies of V_2O_5, V_6O_{13}, VO_2 and V_2O_3. *Journal of Electron Spectroscopy and Related Phenomena*, 71:249–261, 1995.

[48] B. Tepper and B. Richter and A.-C. Dupuis and H. Kuhlenbeck and C. Hucho and P. Schilbe and M. A. bin Yarmo and H.-J. Freund. Adsorption of molecular and atomic hydrogen on vacuum-cleaved $V_2O_5(001)$. *Surface Science*, 496:64–72, 2002.

[49] A.-C. Dupuis, M. Abu Haija, B. Richter, H. Kuhlenbeck, and H.-J. Freund. $V_2O_3(0001)$ on Au(111) and W(110): growth, termination and electronic structure. *Surface Science*, (539):99112, 2003.

[50] A.-C. Dupuis. $V_2O_3(0001)$ on Au(111) and W(110): Metal to Insulator Transition Induced by Surface Termination. *arXiv:cond-mat/0610232v2 [cond-mat.other]*, October 2006.

[51] Horst Niehus, Ralf-Peter Blum, and Dirk Ahlbehrendt. Structure of vanadium oxide (V_2O_3) Grown On $Cu_3Au(100)$. *Surface Review and Letters*, 10(2 & 3):353–359, 2003.

[52] F. P. Leisenberger, S. Surnev, L. Vitali, M. G. Ramsey, and F. P. Netzer. Nature, growth and stability of vanadium oxides on Pd(111). *Journal of Vacuum Science and Technology A*, 4(17):1743–1749, 1999.

[53] S. Surnev, L. Vitali, M. G. Ramsey, F. P. Netzer, G. Kresse, and J. Hafner. Growth and structure of ultrathin vanadium oxide layers on Pd(111). *Physical Review Letters*, 61(20):13945–13954, May 2000.

[54] S. Surnev, G. Kresse, M. G. Ramsey, and F. P. Netzer. Novel interface-mediated metastable oxide phases: Vanadium oxides on Pd(111). *Physical Review Letters*, 87(8):086102, August 2001.

[55] J. Schoiswohl, M. Sock, S. Surnev, M.G. Ramsey, F.P. Netzer, G. Kresse, and J.N. Andersen. $V_2o_3(0001)$ surface terminations: from oxygen- to vanadium-rich. *Surface Science*, 555:101117, 2004.

[56] J. Schoiswohl, M. Sock, S. Eck, S. Surnev, M. G. Ramsey, and F. P. Netzer. Atomic-level growth study of vanadium oxide nanostructures on Rh(111). *Physical Review B*, 69:155403, 2004.

[57] G. Kresse, S. Surnev, J. Schoiswohl, and F.P. Netzer. $V_2O_3(0001)$ surface terminations: a density functional study. *Surface Science*, 555:118134, 2004.

[58] I. Czekaj, K. Hermann, and M. Witko. Ab initio density functional theory studies on oxygen stabilization at the V2O3(0001) surface. *Surface Science*, 545:8598, 2003.

[59] E.A. Kröger and D.I. Sayago and F. Allegretti and M.J. Knight and M. Polcik and W. Unterberger and T.J. Lerotholi and K.A. Hogan and C.L.A. Lamont and D.P. Woodruff. The structure of the $V_2O_3(0001)$ surface: A scanned-energy mode photoelectron diffraction study. *Surface Science*, 601:3350–3360, 2007.

[60] P. Guénard and G. Renaud and A. Barbier and M. Gautier-Soyer. Determination of the α-$Al_2O_3(0001)$ Surface Relaxation and Termination by Measurements of Crystal Truncation Rods. *Surface Review and Letters*, 5(1):321 – 324, February 1998.

[61] C.F. Walters, K.F. McCarty, E.A. Soares, and M.A. Van Hove. The surface structure of α-Al2O3 determined by low-energy electron diffraction: aluminum termination and evidence for anomolously large thermal vibrations. *Surface Science*, 464:L732L738, 2000.

[62] J. Ahn and J.W. Rabalais. Composition and structure of the $Al_20_3(0001) - (1 \times 1)$ surface. *Surface Science*, 388:121–131, 1997.

[63] Th. Gloege and H.L. Meyerheim and W. Moritz and D.Wolf. X-ray structure analysis of the $Cr_2O3(0001) - (1 \times 1)$ surface: evidence for Cr interstitial. *Surface Science Letters*, 441:L917–L923, 1999.

[64] F. Rohr and M. Bäumer and H.-J. Freund and J.A. Mejias and V. Staemmler and S. Müller and L. Hammer and K. Heinz. Strong relaxations at the $Cr_2O_3(0001)$ surface as determined via low-energy electron diffraction and molecular dynamics simulations. *Surface Science Letters*, 372:L291–L297, 1997. Erratum, *Surface Science*, 389:391, 1997.

[65] K. Wolter. Unpublished results. *cited in ref [49].*

[66] Bernd Dillmann, Friedmann Rohr, Oliver Seiferth, Gabor Klivenyi, Michael Bender, Klemens Homann, Ivan N. Yakovkin, Daniela Ehrlich, Marcus Bäumer, Helmut Kuhlenbeck, and Hans-Joachim Freund. Adsorption on a polar oxide surface: O_2, C_2H_4 and Na on $Cr_2O_3(0001)/Cr(110)$. *Faraday Discussions*, 105:295–315, 1996.

[67] I. Czekaj, K. Hermann, and M. Witko. Relaxation and electronic structure of the $V_2O_3(0001)$ surface: ab initio cluster model studies. *Surface Science*, 525:3345, 2003.

[68] I. Czekaj, M. Witko, and K. Hermann. Structure and electronic properties of the $V_2O_3(0001)$ surface: ab initio density functional theory cluster studies. *Surface Science*, 525:4656, 2003.

[69] F. Pfuner, J. Schoiswohl, M. Sock, S. Surnev, M. G. Ramsey, and F. P. Netzer. The metalinsulator transition in $V_2O_3(0001)$ thin films: surface termination effects. *Journal of Physics: Condensed Matter*, 17:40354047, 2005.

[70] S. Surnev, G. Kresse, M. Sock, M. G. Ramsey, and F. P. Netzer. Surface structures of ultrathin vanadium oxide films on Pd(111). *Surface Science*, 495:91–106, 2001.

[71] G. A. Sawatzky and D. Post. X-ray photoelectron and Auger spectroscopy study of some vanadium oxides. *Physical Review B*, 20(4):1546–1555, August 1979.

[72] Matej Mayer. http://www.rzg.mpg.de/ mam/index.html. *SIMNRA Program.*

[73] J B Zhou and H.C. Lu and T. Gustafsson and P. Häberle. Surface structure of MgO(001): a medium energy ion scattering study. *Surface Science*, (302):350–362, 1994.

[74] G. S. Parkinson and M. A. Muñoz-Márquez and P. D. Quinn and M. J. Gladys and R. E. Tanner and D. P. Woodruff. Medium-energy ion-scattering study of the structure of clean $TiO_2(110)-(1\times1)$. *Physical Review B*, 73(245409):1–11, 2006.

[75] Paul D. Quinn. MEIS energy cut simulator. 2004.

[76] G. Kresse, S. Surnev, M. G. Ramsey, and F. P. Netzer. First-principles calculations for V_xO_y grown on Pd(111). *Surface Science*, 492:329–344, 2001.

[77] W. Unterberger. *Private Discussions*, August 2009.

[78] Giovanni D. Aloisi, Massimiliano Cavallini, Massimo Innocenti, Maria Luisa Foresti, Giovanni Pezzatini, and Rolando Guidelli. In Situ STM and Electrochemical Investigation of Sulfur Oxidative Underpotential Deposition on Ag(111). *Journal of Physical Chemistry B*, 101:4774–4780, 1997.

[79] A. L. Harris, L. Rothberg, L. H. Dubois, N. J. Levinos, and L. Dhar. Molecular Vibrational Energy Relaxation at a Metal Surface: Methyl Thiolate on Ag(111). *Physical Review Letters*, 64(17):2086–2089, 1990.

[80] Miao Yu, S. M. Driver, and D. P. Woodruff. Scanning Tunneling Microscopy Investigation of the Structure of Methanethiolate on Ag(111). *Langmuir*, 21:7285–7291, 2005.

[81] Miao Yu, D. P. Woodruff, N. Bovet, C. J. Satterley, K. Lovelock, Robert G. Jones, and V. Dhanak. Structure Investigation of $Ag(111)(\sqrt{7}\times\sqrt{7})R19^\circ-SCH_3$ by X-ray Standing Waves: A Case of Thiol-Induced Substrate Reconstruction. *J. Phys. Chem. B*, 110:2164–2170, 2006.

[82] G.S. Parkinson, A. Hentz, P.D. Quinn, A.J. Window, D.P. Woodruff, P. Bailey, and T.C.Q. Noakes. Methylthiolate-induced reconstruction of Ag(111): A medium energy ion scattering study. *Surface Science*, 601:5057, 2007.

[83] K. Schwaha, N. D. Spencer, and R. M. Lambert. A Single Crystal Study of the Initial Stages of Silver Sulphidation: The Chemisorption and Reactivity of Molecular Sulphur (S_2) on Ag(111). *Surface Science*, 81:273–284, 1978.

[84] G. Rovida and F. Pratesi. Sulfur Overlayers on the Low-Index Faces of Silver. *Surface Science*, 104:609–624, 1981.

[85] R. Heinz and J. P. Rabe. Scanning Tunneling Microscopy Investigation of Sulfide and Alkanethiolate Adlayers on Ag(111). *Langmuir*, 11:506–511, 1995.

[86] David W. Hatchett and Henry S. White. Electrochemistry of Sulfur Adlayers on the Low-Index Faces of Silver. *Journal of Physical Chemistry*, 100:9854–9859, 1996.

[87] Jr Jodie L. Conyers and Henry S. White. Electrochemical Growth of Ag_2S on Ag(111) Electrodes. Coulometric and X-ray Photoelectron Spectroscopic Analysis of the Stepwise Formation of the First and Second Monolayers of Ag_2S. *Journal of Physical Chemistry B*, 103:1960–1965, 1999.

[88] Verónica Brunetti, Bárbara Blum, Roberto C. Salvarezza, and Alejandro J. Arvia. Comparative molecular resolution stm imaging of thiourea, ethylthiourea, and sulfur self-assembled adlayer structures on silver (111). *Langmuir*, 19:5336–5343, 2003.

[89] S. Hull, D. A. Keen, D. S. Sivia, P. A. Madden, and M. Wilson. The high-temperature superionic behaviour of Ag_2S. *Journal of Physics: Condensed Matter*, 14:L9L17, 2002.

[90] W. Heegemann, K.H. Meister, E. Bechtold, and K. Hayek. The Adsorption of Sulfur on the (100) and (111) Faces of Platinum; a LEED and AES Study. *Surface Science*, 49:161–180, 1975.

[91] T. Flores, M. Hansen, and M. Wuttig. Structure and Growth of Mn on Cu(100). *Surface Science*, 279:251–264, 1992.

[92] M. J. Harrison, D. P. Woodruff, and J. Robinson. Alloying-induced surface stress change in Cu(100)$c(2 \times 2)-$Mn. *Physical Review B*, 72(113408):1–3, 2005.

[93] T. Flores, S. Junghans, and M. Wuttig. Atomic mechanisms of the formation of an ordered surface alloy: an STM investigation of Mn/Cu(100). *Surface Science*, 371:14–29, 1997.

[94] D. Wortmann and S. Heinze and G. Bihlmayer and S. Blügel. Interpreting STM images of the MnCu/Cu(100) surface alloy. *Physical Review B*, 62(4):2862–2868, 2000.

[95] Y. Huttel, F. Schiller, J. Avila, and M. C. Asensio. Electronic and structural properties of Mn/Cu superstructures. *Physical Review B*, 61(7):4948–4957, 2000.

[96] C. Binns and C. Norris. Manganese Overlayers on Copper(100); A Study by LEED, AES and UPS. *Surface Science*, 116:338–350, 1982.

[97] R. Toomes and A. Theobald and R. Lindsay and T. Geißel and O. Schaffz and R. Didszhun and D. P. Woodruff and A. M. Bradshaw and V Fritzsche. Photoelectron diffraction determination of the structure of the Cu(100)$c(2 \times$ 2)Mn surface phase. *Journal of Physics: Condensed Matter*, 8:1023110240, 1996.

[98] M. Wuttig, C.C. Knight, T. Flores, and Y. Gauthier. LEED structure determination of two ordered surface alloys: Cu(100) $- c(2 \times 2)$Mn and Ni(100) $- c(2 \times 2)$Mn. *Surface Science*, 292:189–195, 1993.

[99] M. Wuttig and Y. Gauthier and S. Blügel. Magnetically driven buckling and stability of ordered surface alloys: Cu(100)$c(2\times2)$mn. *Physical Review Letters*, 70(23):3619–3622, 1993.

[100] R.G.P. van der Kraan and H. van Kempen. Growth of Mn on Cu(100) studied by STM: the $c(2 \times 2)$ and $pgg(4 \times 2)$ ordered surface alloys. *Surface Science*, 338:19–30, 1995.

[101] W. Pan, R. Popescu, H. L. Meyerheim, D. Sander, O. Robach, S. Ferrer, Minn-Tsong Lin, and J. Kirschner. Stress and structure of $c(2 \times 2)$ and $p2gg(4 \times 2)$ Mn/Cu(001) surface alloys. *Physical Review B*, 71(174439), 2005.